MODELING OF ACTIVE CRACK DAMAGE CONTROL AND THE ACTIVE FATIGUE DAMAGE CONTROL OF ADHESIVE JOINT

by

Shi Li

Thesis submitted to the Faculty of the

Virginia Polytechnic Institute and State University

in partial fulfillment of the requirements for the degree of

MASTER OF SCIENCE

in

Mechanical Engineering

APPROVED:

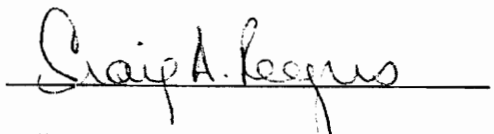

Dr. Craig A. Rogers, Chairman

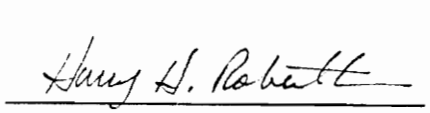

Dr. Harry H. Robertshaw

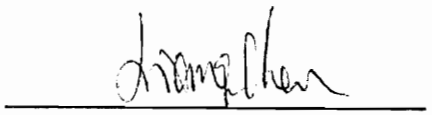

Dr. Chen Liang

September, 1992

Blacksburg, Virginia

Investigation of Active Crack Damage Control and Active Fatigue Damage Control of Adhesive Joints

by

Shi Li

Committee Chairman: Dr. Craig A. Rogers

Mechanical Engineering

Abstract

Active damage control is a new technique which mimics the self-repairing capability of biological beings and can be used to greatly increase the structural integrity and fatigue life. This thesis describes two approaches used in active damage control: direct stress cancellation and indirect stress cancellation.

Direct stress cancellation is illustrated using an example of active crack damage control with embedded shape memory alloy actuators. Both experimental and theoretical investigations have been conducted to analyze the damage control mechanism. The approach of indirect stress cancellation is demonstrated with active fatigue damage control of adhesive joints. The damage and active control mechanisms of the adhesive joints have been experimentally and theoretically investigated.

Acknowledgements

I would like to express my gratitude to my advisor, Dr. Craig A. Rogers, for his time and efforts in assisting me with the completion of my research project. Without his invaluable directions and suggestions, I would not be able to complete this work. I would also like to thank the members of my committee, Dr. Harry H. Robertshaw and Dr. Chen Liang for their help and assistance.

I also would like to thank all those in the center for Intelligent Material Systems and Structures, who have done me favors to listen to my thoughts, to discuss and answer my questions, and to give me advice and suggestions. Among them, Dr. Chen Liang deserves special thanks for his help in my research work and the completion of this thesis.

Thanks also go to the professors in Beijing University of Aeronautics and Astronautics for providing the high-quality education and training programs. My special thanks go to Prof. D. Chen and Prof. J. Nie for recommending me to study in Virginia Polytechnic Institute and State University.

Finally, I would like to give my heartfelt thanks to my parents, Maorong Li and Litian

Sun, and my family for their support and encouragement from overseas. I cannot express the depth of my gratitude and love for my wife, Zhijun Yin, for her willingness to put up with many hardships and to sacrifice her time and energy to support my study through the most stressful time in the past three years.

Table of Contents

Nomenclature

a_A, a_M	Material constants associated with temperature induced transformation
A_f, A_s	Austenite finish and start temperatures
b_A, b_M	Material constants associated with stress induced transformation
c	Crack length (in Chapter 2)
c	Moment intensity (in Chapter 3)
c_0	Characteristic length of crack
c'	Viscus damping coefficient
c^*	Structural damping coefficient
C_M, C_A	Stress influence coefficient
d	Diameter of SMA fiber
D	Elastic modulus
E_a, E_b	Elastic modulus of components, a and b
E_c	Elastic modulus of composites
E_e	Equivalent stiffness used for the actuator element in finite element analysis

E_A	Young's modulus of SMA actuators
E'_A	Equivalent modulus for the prestrained SMA
E_{Ae}	Equivalent modulus for restrained SMA element
E_M	Young's modulus of Matrix
I	Area moment of inertia
J	J-integral
K_I	Stress intensity factor
K_{AP}	Appearance stress intensity factor in photoelastic measurement
K^L	Stress intensity factor in SMA hybrid composites
K_c^M	Stress intensity factor of matrix in composites
l_d	Debonding length of the SMA fiber in matrix
L	Length of the beam
M	Moment of the beam
N	Photoelastic stress fringe order
P	Radial pressure across the interface
p(x)	Equivalent surface traction on the crack surface in tension stage
q(x)	Equivalent surface traction on the crack surface in activation stage
r	Distance measured from the crack tip
R_m	Electrostrictive coefficient
S_i	Deformation in PZT expression
t	Thickness of the components

t_a, t_b	Thickness of the components a and b
T	Temperature
v	Lateral displacement
v_f	Volume fraction of fibers
v_m	Volume fraction of matrix
v_n	Normal mode of the structure displacement
V	Shear force at any section
V_n	Normal mode of the structure shear force
w	Distributed load
α	Thermoexpansion coefficient
α_A	Equivalent thermal expansion coefficient for the activation strain of SMA in F.E.A.
γ	Specific weight of material
ΔT	Temperature increment
$\Delta\sigma_f$	Increment of fiber stress
ϵ	Engineering strain
ϵ_f	Engineering strain on bridging SMA fiber
ϵ_0	Initial engineering strain
θ	Thermoelastic tensor (in Chapter 2)
θ	Rotary angle of the deflection curve
κ	Curvature of the beam

Λ	Activation strain of PZT actuators
μ	Friction coefficient
ν_s	Relative Poisson's ratio
ν_f	Poisson's ratio of the fiber in composites
ν_m	Poisson's ratio of the matrix in composites
ξ	Martensite volume fraction
ξ_A, ξ_M	Initial martensite fraction of SMA
ρ	Density of material
σ	Engineering stress
σ_∞	Structure loading
σ_f	Fiber stress
σ_d	Critical fiber stress for debonding
σ_y	Yield strength
τ	Shear stress
Ω	Phase transformation tensor
ω	Frequency of excitation
ω_n	Natural frequencies of the vibration system

Chapter 1 Introduction

1.1 Introduction to Damage Control

Damage exists in nearly all engineering structures although most engineering structures are performing safely and reliably. The existence of damage in modern engineering structures may be attributed to the unfavorable mechanical and/or environmental conditions. Local damage, such as flaws, defects or discrepancies, can propagate under structure loading and finally result in structure failure. The presence of these flaws was not accounted for in the designs, which are based on a "safe-life" fatigue analysis. Some of the kinds of damage and their characteristics are described briefly below.

(a) Creep Damage. At high temperatures and under conditions of stress, an accumulation and growth of microvoids in metal grains take place (ductile transgranular creep fracture). At the same time, an accumulation and growth of microcracks on intergranular boundaries (brittle intergranular creep fracture) occurs.

(b) Ductile Plastic Damage. Nucleation and growth of microvoids and microcracks generate in metals as the result of a large plastic strain. This process leads to so-called plastic fracture.

(c) Fatigue Damage. Under conditions of cyclic loading, a gradual deterioration of the

structure of a material, caused by the accumulation and growth of micro and macro cracks, takes place.

(d) Embrittlement of Steels. Under conditions of atomic radiation, the structure of steel is changed, which decreases the plasticity and leads to embrittlement. As a result, free hydrogen atoms diffuse into the atomic grid of the steel, which leads to dangerous embrittlement of the structure (hydrogen brittleness).

(e) Chemomechanical Damage. Under conditions of tensile stress (especially cyclic stress), metals operating in aggressive media (e.g., sea water) are subjected to intensive corrosion (stress corrosion) or to other chemical reactions.

(f) Environmental Degradation. Some materials change their mechanical properties under environmental influences even in the absence of stress. For example, the mechanical properties of soil, wood and some other materials depend on the level of humidity in the environment.

(g) Damage of Composites. Since composites are non-homogeneous materials, they consist of zones of weak mechanical resistance, which, under loading, leads to the appearance of cracks and delaminations.

Although damage exists in every engineering structure, the comparatively few service failures in structures indicate that present-day practices governing material properties and design and fabrication procedures are generally satisfactory. However, the occurrence of infrequent failures indicates that further understanding and possible modifications of

present-day practices are necessary. Identification of the specific modifications needed requires a thorough study of material properties, design, fabrication, inspection, erection, and service conditions.

Techniques of damage control have been developing for decades. For example, in the mid 1970s, in order to ensure the safety of aircraft structures, the U.S. Air Force adopted the damage tolerance design approach to replace the conventional fatigue design approach. In recent years, a number of different industries have adopted the damage tolerance approach, calling it "fracture control". The ability of a structure to maintain adequate residual strength in a damaged condition is called damage tolerance. The damage tolerance (or fracture control) approach assumes that flaws are initially present in the structure. The structure must be designed such that these flaws do not grow to a critical size and cause catastrophic failure of the structure within a specific period of time. In order to accomplish this, an accurate damage tolerance analysis must exist. This analysis can be found in several fracture mechanics textbooks (Hertzberg, R.W., 1989; Parker, A.P., 1981; Kanninen and Popelar, 1985).

After the damage tolerance analysis, the residual lifetime can be determined. However, since the structure fails from a tiny flaw or a small crack, the servicing lifetime can be greatly increased if the crack growth can be restricted or delayed. Based on this consideration, the damage control technique becomes valuable. Some of the damage

control strategies are listed below.

(a) *Change of structure design to decrease the stress in the structure and to increase the damage tolerance of the structure.* The design can be changed geometrically to fit the standard of fracture mechanics (Meguid, 1989). By using a fail-safe design philosophy, the structures can have multiple load-path members, such as multiple stringer bridges. The damage and failure of one member does not necessarily lead to overall failure of the structure because the load is carried by adjacent members (Rolfe, 1972). Another method is the use of crack arresters (Rolfe et al., 1977). The crack arresters or crack stoppers are placed at various locations within a structure, and excessive crack growth is arrested before the structure fails. This technique is widely used in the aircraft industry where bonded doubler plates or crack arresters are attached to the skin of the aircraft.

(b) *Mechanical treatment of the structure.* A typical application of this strategy is in prestressed concrete (Nawy, 1989). In prestressed concrete, prestressed fibers apply compressive forces on the structure, and these compressive forces can balance tensile stresses generated by external forces or moments, resulting in an increase of the loading capacity of the structure, and eliminating or controlling cracking and deflection of the structure.

(c) *Surface treatment of components.* One of the methods is impact surface treatment, such as shot-peening (Meguid, 1986). Impinging the surfaces of components with spherical particles to yield state will induce residual compressive stresses in the surface

of the components. The fatigue life of the components will be greatly increased because of the compressive stresses.

(d) *Adaptive damage control.* A typical example of adaptive damage control is ZrO_2-containing ceramics (Evans and Heuer, 1980). In Zirconia ceramics, the precipitates of tetragonal ZrO_2 will martensitically transform to monoclinic symmetry when deformation exists in the structure, and the martensitic transformation in the stress field of propagating cracks leads to dramatic increases in the toughness of the ceramics. Another example is adhesive strips embedded in the interface in graphite/epoxy (Sun and Norman, 1990). Under impact loading the adhesive strips can absorb more impact energy, and are helpful in containing the delamination in laminated composites.

(e) *Active damage control.* This is a newly developing area in the damage control field (Rogers et al., 1991). Active damage control will actively change the stress and strain field at the crucial area, such as the crack area and the high stress concentration area, of structures by activating induced strain actuators which are embedded in or mounted on the structures, resulting in a reduction of the damage level and a decrease in the damage growth rate. This thesis will focus on this topic and introduce two models of active damage control.

1.2 Introduction to the Mechanism of Active Damage Control

For many years, scientists and engineers have taken a passive approach to studying

fractures and the crack propagation of structures. A great deal of effort has been put into predicating the location and the nature of fractures and examining how they propagate. The typical design approaches used to rectify high stress intensity factors involve changing the physical design to reduce the stress level or replacing the original materials with tougher ones. The best design approach thus far is obviously the one that prevents the occurrence of dangerous fractures in the first place. However, one cannot assure that the design will be absolutely free of fractures. In most cases, structures must be replaced if any indication of fracture is found. However, if a structure is in service, such as an airplane, the occurrence of a dangerous crack may result in a disaster. Nevertheless, the application of fracture mechanics and other techniques, such as damage tolerance, have greatly improved the capability of engineers to design safe structures. However, new concepts, material systems and design philosophies are still needed in order to thoroughly conquer the strongest enemy of engineering structures, the hidden fractures.

Combined with today's sensors, actuators, and computer technology, an exciting material system concept known as, "intelligent material systems" is currently being investigated (Rogers, 1990). An intelligent material system is a hybrid material system with integrated sensors, control processors, and induced strain actuators designed to provide multi-functional capabilities. One important operational aspect of an intelligent material system could be self-damage sensing and self-damage control or repair.

The active damage control concept can be described as a two-part procedure. First, the occurrence and the position of damage (e.g., cracks) are detected with a sensor system. Second, induced strain actuators embedded in or mounted on the structure are activated. The activation of the induced strain actuators can change the stress and strain field at the crack tip, or the high stress and strain zone, leading to a reduction of stress intensity factor, so that the initiation and propagation of the crack will be slowed or stopped. The analysis in this thesis will concentrate on the mechanical control effect of the second part of the procedure involved in active damage control.

Active damage control methods can be classified into two categories - direct damage control and indirect damage control. Mechanically analyzing the activated induced strain actuators can generate induced strains, and with the constraint of the structure, induced stresses will be generated. These induced strains and stresses can directly change the original local strain and stress distribution (which results in a decrease in the local damage level), creating the scenario of direct damage control. Also, these induced strains and stresses can excite a dynamic response of the structure, and the dynamic response can change the original stress and strain distribution (which results in a decrease in the dynamic damage level), creating the scenario of the indirect damage control.

Active direct damage control was studied by conducting photoelastic experiments and performing finite element analysis (Rogers et al., 1991). The induced strain actuators

were placed around the damage area. It was found that proper actuation will directly reduce the stress concentration in the damage area, resulting in a retardation of damage level. In this scenario, the control force comes directly from the activation force of induced strain actuators. The mechanical model of active crack damage control analyzed in Chapter 2 is an example of active direct damage control.

Active indirect damage control aims to control the dynamic response and to decrease the dynamic stress and strain level in the structure. The control force is not directly from the activation force of induced strain actuators, but from the inertial force excited by the actuation force of induced strain actuators. Studies of active control of delaminations in composite structures (Hanagud et al., 1992) belongs to this indirect damage control category. The control scheme is arranged to control the dynamic response of a delaminated cantilever beam using induced strain actuators, resulting in a reduction in the inplane delamination force. Active indirect damage control can be simply illustrated by the following experiment involving active fatigue damage control (Rogers et al., 1991). The experimental set-up is shown in Fig. 1.1. A composite beam was bonded on an aluminum bracket and subjected to a fatigue loading from a motor. Two PZT actuators were mounted on the upper and lower surfaces of the beam. The actuators operated at the same frequency as the fatigue loading, but the induced stress from the actuators in the bonding area was out-of-phase with the fatigue loading. When the vibration frequencies are close to the resonant frequencies of structures, the inertial force

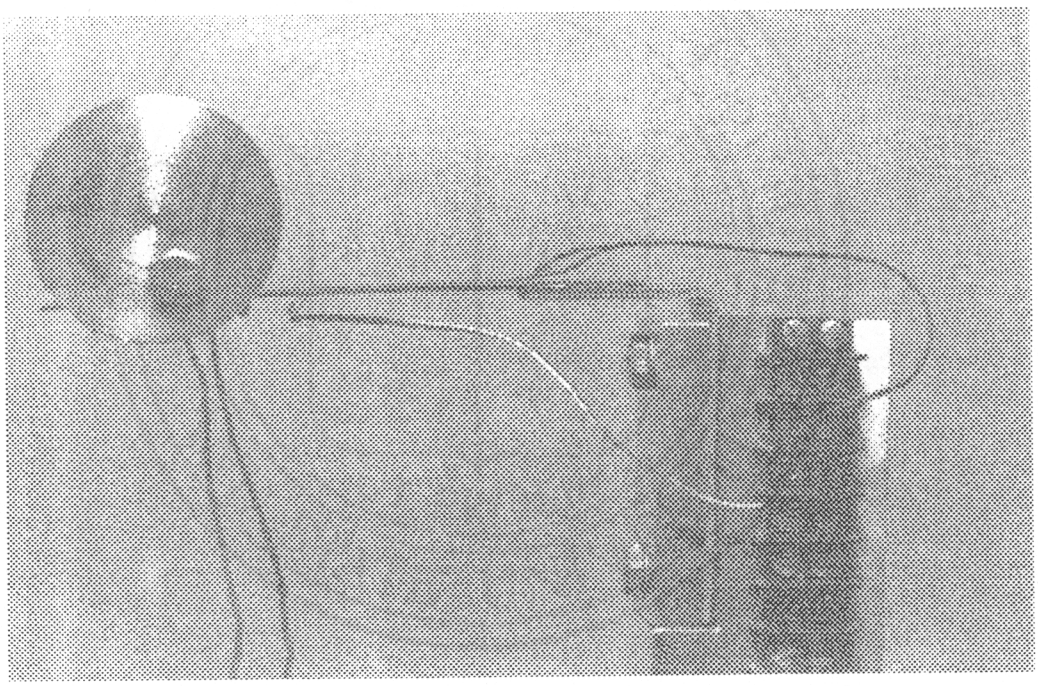

Figure 1.1: Active fatigue damage control of an adhesive joint with an active global damage control scheme.

of the beam generated tremendous shear and peeling force in the glue bonding layer. On the other hand, the induced strain actuators generated an out-of-phase dynamic response. This response, when superposed with the original response, can cancel part of the original dynamic response, resulting in a sharp fall in the stress level in the adhesive layer. By reducing the fatigue stress amplitude, the fatigue cycles of the bonding joint were increased significantly. The fatigue life of the bond without the active control was 52,000 cycles, while this number increased to more than 500,000 cycles when the actuators were activated. A detailed mechanical analysis will be conducted later.

The mechanism of active damage control can be analyzed not only from a stress-strain point of view, but also from an energy point of view. Both analyses are meaningful, but have different emphatic points. The stress-strain analysis is advantageous in explaining the detail of the control mechanism, while the energy analysis is helpful in explaining the physical meaning of control scheme. Active direct damage control can be analyzed as the input of new energy by induced strain actuators that changes the original local energy distribution in the structure, causing a decrease in the high stress concentration. Active indirect damage control (e.g., fatigue damage control of a adhesive joint) can be analyzed as the input of new energy by induced strain actuators that obstructs the input of the original source energy. In this case, the original dynamic energy in the system is dissipated by structure damping, resulting in a decrease in the total energy in the system

and a decrease in the strain energy in the adhesive joint.

1.3 Introduction to Induced Strain Actuators

Induced strain actuators are energy transducers, which can transfer different kinds of energy, such as electric, magnetic, and thermal energy, into mechanical energy. Currently, there are three types of induced strain actuators which are often used. They are shape memory alloy (SMA) actuators, piezoelectric actuators, and electrostrictive actuators. A brief introduction of each type of actuators is given below.

1.3.1 SMA Actuators

Ti-Ni-based shape memory alloy (Nitinol) has been investigated for decades. The earliest research can be traced back to the early 1960's when Buehler and Wiley (1965) of the U. S. Naval Ordnance Laboratory received a U.S. patent on a series of engineering alloys possessing a unique mechanical (shape) 'memory'. The generic name of this series of alloys is 55-Nitinol. These alloys have chemical compositions in the range of 53-54 weight percent Nickel.

Shape memory alloys depend on the shape memory effect (SME) for their actuator characteristics. The SME can be briefly described as follows: an object in the low-

temperature martensitic phase, after being inelastically deformed and having the external stress removed, will regain its original (memorized) shape upon being heated. The process is the result of a martensitic phase transformation during the heating process, while the process of regaining the original shape is associated with a reverse transformation of the stress-induced martensitic phase to the higher-temperature austenitic phase. Inelastic strains of typically 6%-8% (which are used as induced strain) may be completely recovered by heating the material so as to transform it to its austenite phase. If an initially elongated SMA wire is constrained and heated, it will generate an enormous stress referred to as, "recovery stress". The recovery stress is another aspect of the shape memory effect. Figure 1.2 (Cross et al., 1970) shows the recovery stress as a function of temperature for various initial strains of a Nitinol alloy. The recovery stress behavior of SMAs plays a key role in the active damage control of SMA hybrid composites. The recovery stress is generated when heating a constrained initially elongated SMA wire. However, when an SMA actuator is embedded into a composite matrix, the surrounding material has a finite stiffness allowing the embedded SMA fiber to have some recovery strain. A completely different stress-strain relation, which is referred to as, "recovery stress-strain relation" (Dye, 1990), must be used as the constitutive relation of SMA actuators. Shown in Fig. 1.3 is the complete process of loading, unloading, and the constrained recovery process of actuated Nitinol with various spring-rate constraints. The Nitinol wire is first elongated and then unloaded, yielding a residual strain, ϵ_{ro} (Note: the residual strain will fully recover when the SMA wire is

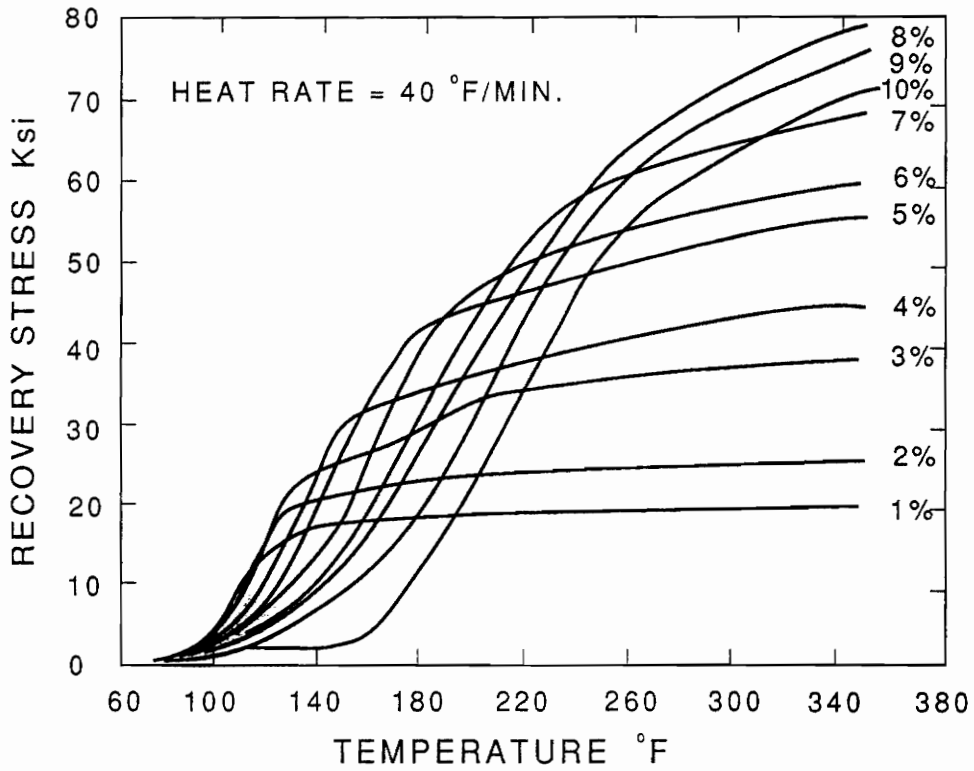

Figure 1.2: Recovery stress vs. temperature of a Nitinol alloy for various initial strains (Cross et al., 1970).

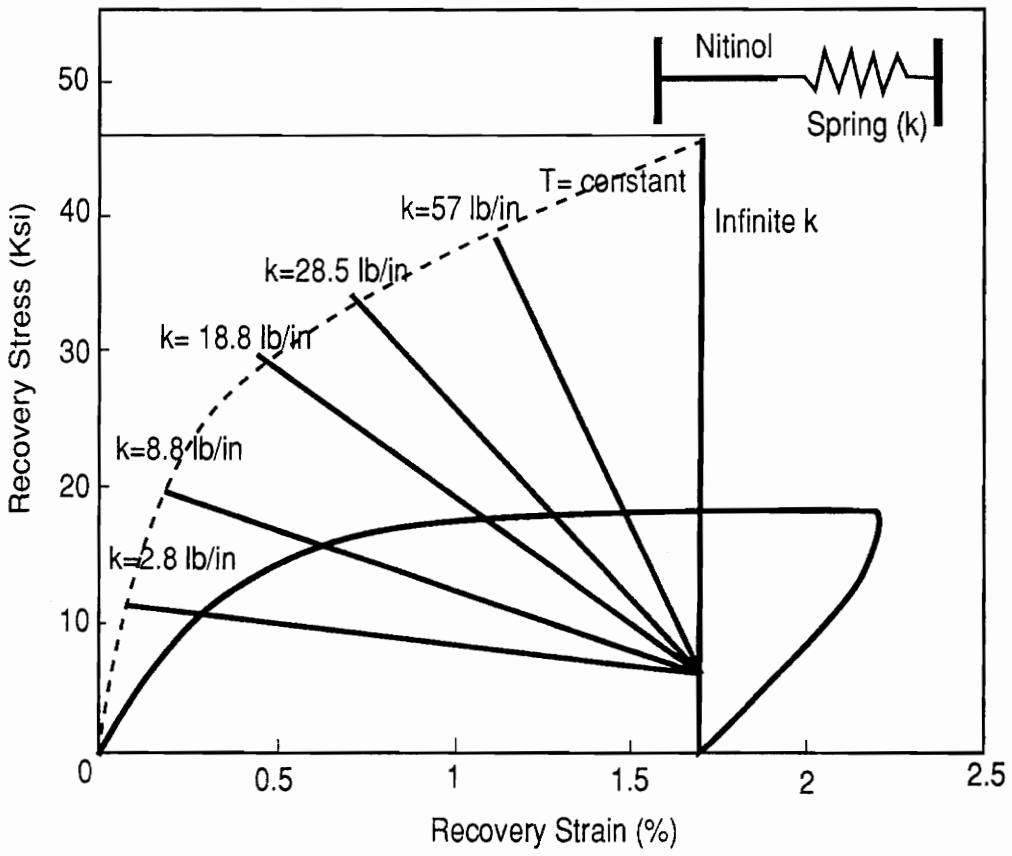

Figure 1.3: Complete loading, unloading, and constrained recovery of a Nitinol alloy (Dye, 1990).

heated if no constraint is applied). The elongated Nitinol is then connected to a spring (the spring constant is also given in Fig. 1.3). The spring will allow a certain amount of recovery strain when the Nitinol wire is heated. This recovery stress-strain relation will be utilized in the theoretical analysis of active damage control of SMA hybrid composite systems.

1.3.2 Piezoelectric Actuators

Piezoelectrics are materials which generate a certain amount of strain when an electric field is applied across the material. The direction of induced strain depends on the direction of the applied electric field, i.e., piezoelectric materials can either expand or contract depending on the direction of the applied electrical voltage.

Piezoelectric materials have been investigated and studied for several decades. Besides being used as induced strain actuators, piezoelectric materials are used in the areas of sonar transducers, phonograph pick-ups, tweeters for audio speakers, and accelerometers. In many of these early applications, piezoceramics and Barium Titanate, $BaTiO_3$, were used (mainly as sensors). Lead Zirconate Titanate (PZT) is now often used as induced strain actuators.

The fundamental governing relationship of piezoelectric materials is the relation of

electric field strength and induced mechanical strain. In the linear theory, the induced mechanical strain in the x_1 - x_2 plain is related to the electric field applied in the x_3 direction (shown in Fig. 1.4) by the piezoelectric coefficient d_{31}:

$$\varepsilon_1^{\text{induced}} = d_{31}E_3 \quad . \tag{1.1}$$

A typical electrical field and strain curve is plotted in Fig. 1.4. There is some nonlinearity between the electrical field and the mechanical strain; nevertheless, the linear model given in Eq. (1.1) is used for most applications.

The stress and strain relation of piezoelectric materials is generally assumed to obey Hook's law for relatively small strains, i.e.,

$$\sigma_{ij} = D_{ijmn}(\varepsilon_{mn} - \varepsilon_{mn}^{\text{induced}}) \quad , \tag{1.2}$$

where D_{ijmn} is the elastic tensor. Piezoelectric materials are considered to be orthotopic in the x_1 - x_2 plane. The elastic modulus of piezoelectric materials in the x_1 -x_2 plane is around 60 GPa. The maximum induced strain can be as high as 1000 microstrains. It is necessary to mention that piezoelectric materials with large induced strain capabilities are now being investigated; the new piezoelectric materials may have an induced strain up to several thousands microstrains.

PZT actuators are the most widely used actuators, in active vibration control

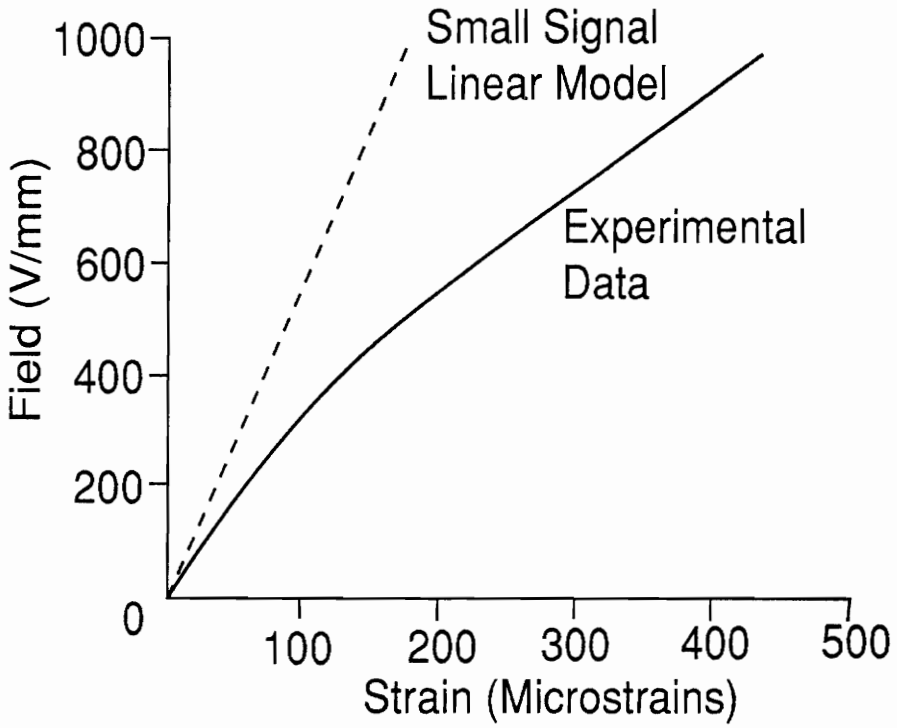

Figure 1.4: Relationship of induced strain and electric field of a piezoelectric material (Anderson and Crawley, 1989).

(Dimitriadis, Fuller and Rogers, 1989), active structural acoustic control (Wang, Dimtriadis and Fuller, 1991), and active shape control (Lazarus and Crawley, 1989; Chaudhry and Rogers, 1991). This thesis will describe how they can also be used in active fatigue damage control.

1.3.3 Electrostrictive Actuators

Electrostrictive materials, like piezoelectric materials, can generate an induced strain when activated by the application of an electric field. The induced strain is approximately proportional to the square of the applied electric field, and the corresponding equation is given by:

$$S_i = R_{m_i}(E_m)\, E_m^2 \quad , \tag{1.3}$$

where S_i, R_{mi} and E_m are the deformation, electrostrictive coefficient and electric field, respectively. In piezoelectrics, the direction of the strain (displacement) is sensitive to the polarity of the field, while in electrostrictive materials, the second order effect insures that the displacement is always positive. The maximum induced strain of currently available electrostrictive materials is about 1000 microstrains. The maximum force generated if an electrostrictive actuator is restrained while being activated can reach up to 100 MPa. Electrostrictive materials have a time response speed of 10 microseconds; the power consumption is low compared to piezoelectric materials. Electrostrictive

actuators exhibit less hysteresis compared to piezoelectrics. They also show no aging or creep effects since no poling is necessary for electrostriction strains (Uchino, 1986).

1.3.4 Comparison of Various Actuators for Active Damage Control

All three kinds of actuators are suitable for active damage control, while each of them has its own advantages and disadvantages which determine the appropriate application area. The advantages of SMA actuators are as follows: (a) the deformation of the activation is larger than that of the other two actuators; (b) the activation force in the actuators can be as high as 540 Mpa; and (c) the fabrication of SMA hybrid composites is easy, and SMA fibers are very effective for crack sensing and bridging crack damage control. These advantages are, however, balanced with the disadvantages of long response time, and difficulty in maintaining the control temperature. Since the activation is triggered by heat, and the temperature cannot be changed in high frequencies, it is difficult for SMA actuators to apply a control force with a frequency higher than 5 Hz. The activation of SMA actuators in SMA hybrid composites can change the stiffness of the structure, and therefore, change the resonance frequencies of the structures. This can change the dynamic response of the structures, and is helpful in active fatigue damage control similar to the SMA in active vibration control. However, in cases involving multi-frequency damage signals, this method is not useful.

The advantages of piezoelectric actuators are in their complimentary characteristics compared with SMA actuators. The frequency response of PZT actuators can be as high as 20 Khz, since the activation is triggered by electric voltage. However, the maximum induced strain is only about 1200 $\mu\epsilon$, and the maximum induced stress is only about 60 Mpa, much smaller values than those obtained using SMA actuators. Based on their characteristics, PZT actuators are suitable for active indirect fatigue damage control. PZT actuators can generate high-frequency dynamic responses which are out-of-phase with the damage responses, and the responses can cancel each other by superposition. However, PZT actuators will have difficulties in active static crack damage control and active direct fatigue damage control, since PZT actuators are not powerful in generating activation force, and are not strong enough to support high-tension stresses.

Electrostrictive actuators have similar characteristics as PZT actuators for active damage control. However, they have following disadvantages compared with PZT actuators: (a) the maximum deformations of the known electrostrictive materials are smaller than those of the best PZT actuators; (b) since electrostriction is a nearly quadratic function of the electric field, the deformation is especially small at low electric fields, which is obstructive to a lowering of the excitation voltage; (c) the practical, usable temperature range is restricted due to the stronger temperature dependence of the electrostrictive mechanism. Applications of electrostrictive actuators in active damage control will not be discussed in this thesis.

1.4 Summary

1. This chapter briefly reviews the seven types of damage models, i.e., creep damage, ductile plastic damage, fatigue damage, embrittlement of steels, chemomechanical damage, environmental damage, and damage of composites. Damage control strategies are also reviewed, i.e., change of structure design, mechanical treatment of structures, surface treatment of components, adaptive damage control, and active damage control.

2. The mechanism of active damage control is presented. Active damage control includes damage signal sensing and damage load control which involves activating induced strain actuators, resulting in a decrease in the stress and strain fields in the structure. In this thesis, the analysis will be focused on the mechanical effect of the activation strains and stresses.

3. The methods of active damage control can be classified into two categories - active direct damage control and active indirect damage control. Active direct damage control employs the induced strains and stresses generated by actuators to directly change the original strain and stress distribution in the structure, resulting in a decrease in the stress concentration. Active indirect damage control uses the induced stresses generated by actuators to excite a dynamic response in the structure, and this dynamic response is

utilized to cancel the original dynamic response, causing a decrease in the damage level in the structure.

4. Active damage control is also analyzed from an energy point of view. Active direct damage control increases the total energy in the structure, but changes the original energy distribution, resulting in a decrease in high-energy concentration. Active indirect damage control uses new energy to obstruct the original damage energy input, resulting in a decrease in the total energy in the structure.

5. The characteristics of SMA, PZT and electrostrictive actuators are discussed. In this thesis, it will be shown how SMA actuators can be used in active bridging crack damage control, and how PZT actuators can be used in active fatigue damage control.

Chapter 2 Modeling of Crack Damage Control

2.1 Scenarios of Active Damage Control with SMA Actuators

A great deal of interest in the control characteristics of intelligent material systems and structures, i.e., materials integrated with distributed sensors and actuators, has been shown in recent years. SMA hybrid composites that contain SMA fibers (or films) have been chosen as the intelligent components to actively control structures. The behavior of SMA hybrid composite systems has been extensively investigated (Barker, 1989; Dye, 1990). Detailed discussion was also given by Rogers et al. (1989). SMA hybrid composites have a tremendous potential for creating new paradigms for material-structure interactions (Rogers, 1989). The list of scientific areas that can be influenced by novel approaches possible with SMA reinforced composites is quite long, e.g., active vibration control, active buckling control, active motion and shape control, etc. The stiffness or compliance of the structures and the force or stress distribution in the structures can be changed with the actuation of the embedded SMA fibers. Therefore, the composites or structures can have various control functions and satisfy different control requirements in engineering with elaborately designed arrangements of SMA fibers.

There are several configurations of SMA hybrid composites that have the capability of

active or adaptive damage control. In all cases, SMA fibers are embedded in a composite material and become an integral part of the material system. In the first configuration, the SMA fibers are inelastically elongated before being embedded. The embedded SMA fibers are constrained from contracting to their 'normal' length during the composite curing or consolidation process. Because of this constraint, the SMA fibers can keep their memory even though the curing temperature is above their annealing temperature during processing. After fabrication, when the fibers are heated generally by passing an electric current through the SMA fibers, the fibers try to return to their 'normal' length, resulting in a change in the internal stress and strain distribution. This type of active damage control is usually limited because of the free edge effect of shape memory alloy hybrid composite systems.

Liang and Rogers (1989) and Lin and Rogers (1990) have shown that the recovery force of embedded SMA fibers acts like a concentrated force at the free edge of SMA hybrid composites when activated. High stress and strain concentrations occur at the free boundaries, while the internal shear stress and deformation due to the recovery force of the SMA fibers is relatively small. The recovery boundary effect is shown in Fig. 2.1. If cracks appear at the center part of the SMA hybrid composites, the activation of the embedded SMA actuators cannot greatly change the stress and strain distributions at the crack tips because of the small activation stress. If only a portion of the embedded

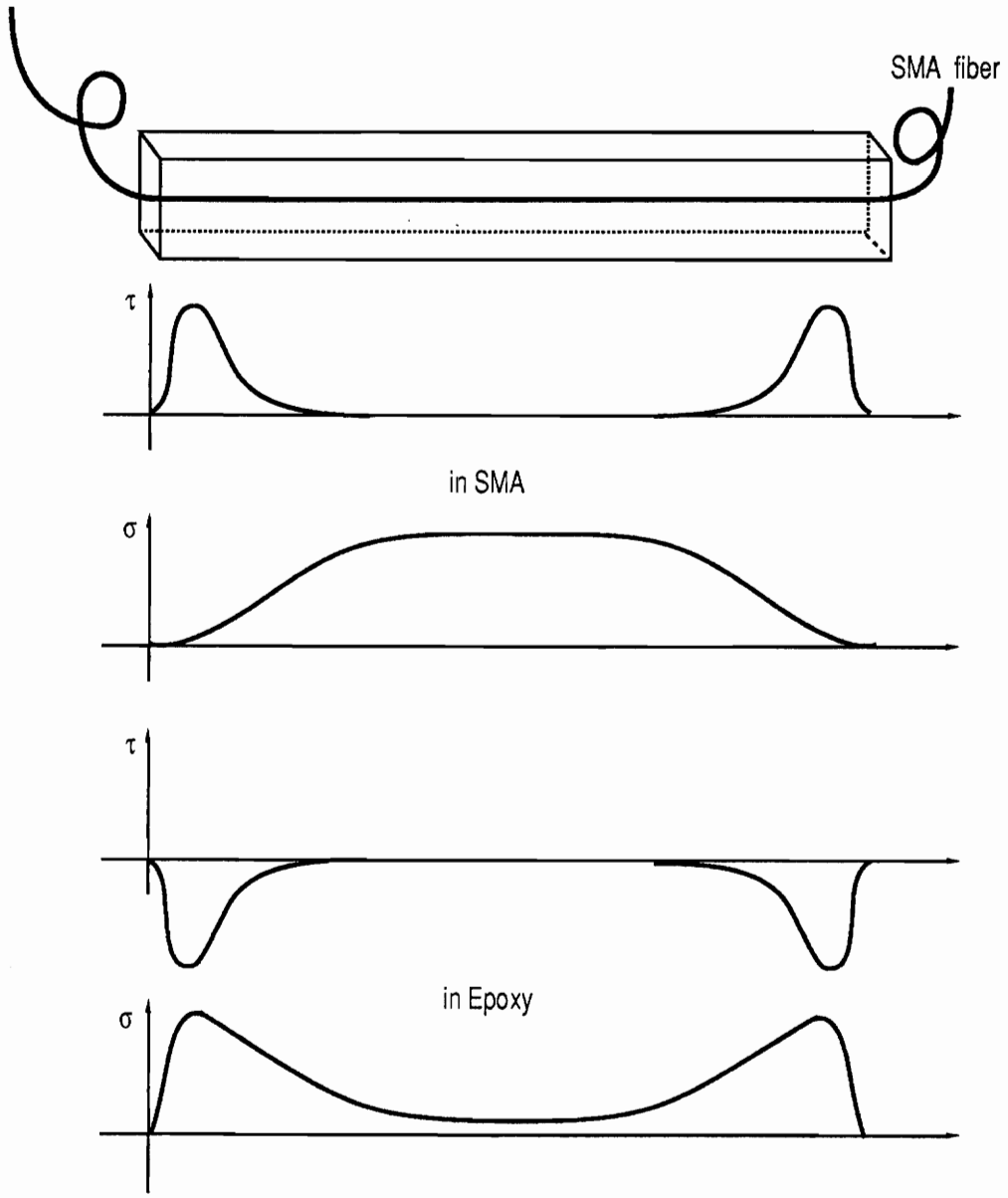

Figure 2.1: Schematic diagram of the recovery boundary effects of SMA actuators.

SMA fibers are inelastically elongated, the free edge effect actually means that the high stress and strain concentrations exist only around the two ends of the inelastically deformed section. Based on this explanation, a better way to control the crack damage is to embed SMA fibers which have very short inelastically deformed sections in composites, and to position these areas where cracks are expected to form. However, in reality it is often difficult to determine where cracks are likely to occur before the fabrication of composites. The free edge effect and the indeterminate position have limited the application of this configuration.

In the second configuration, SMA fibers with no initial elongation are directly embedded into a composite material, as shown in Fig. 2.2. When a crack propagates, is close to, and passes through the embedded SMA fibers, the large strain due to the stress concentration at the crack tip and the crack opening will result in a large strain in the SMA actuators, as shown in Fig. 2.2. When the SMA fibers are activated by passing an electric current through them for resistive heating, the recovery stress generated by the strained SMA actuators will alter the stress and strain distribution at the crack tips, as shown in Fig. 2.3. The recovery stress in SMA fibers is tensile, and the reaction force in the matrix is compressive, resulting in a decrease in the stress concentration at the crack tip, i.e., a reduction in the stress intensity factor. The compressive forces resulting from heating the embedded SMA fibers can alter the stress and strain distribution at the crack tip area or even close the crack, so that further propagation of

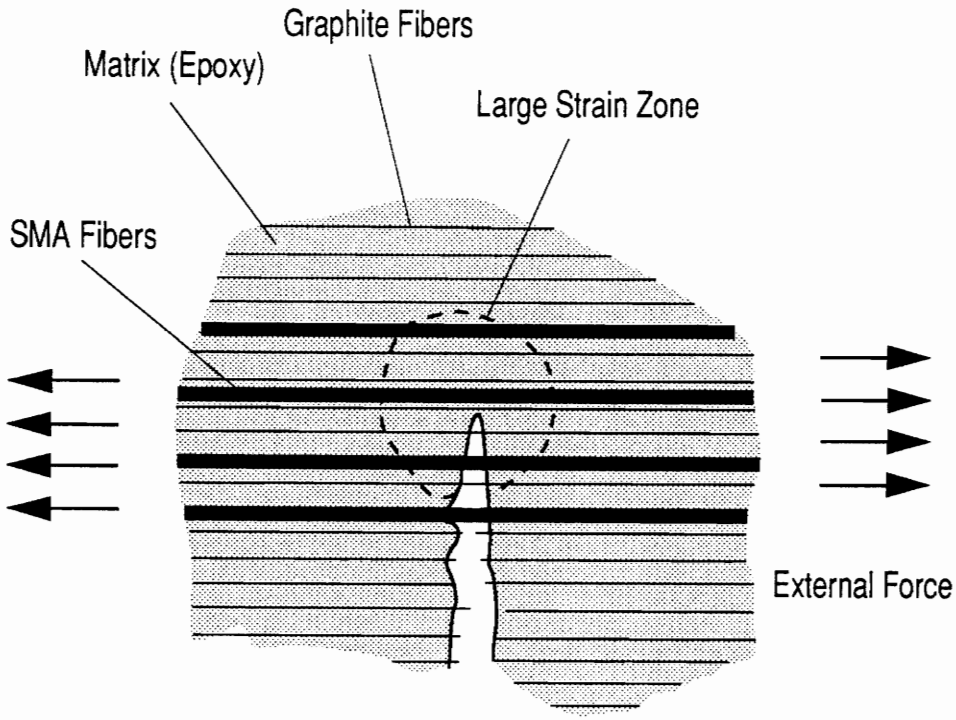

Figure 2.2: Schematic diagram of a crack in an SMA hybrid composite.

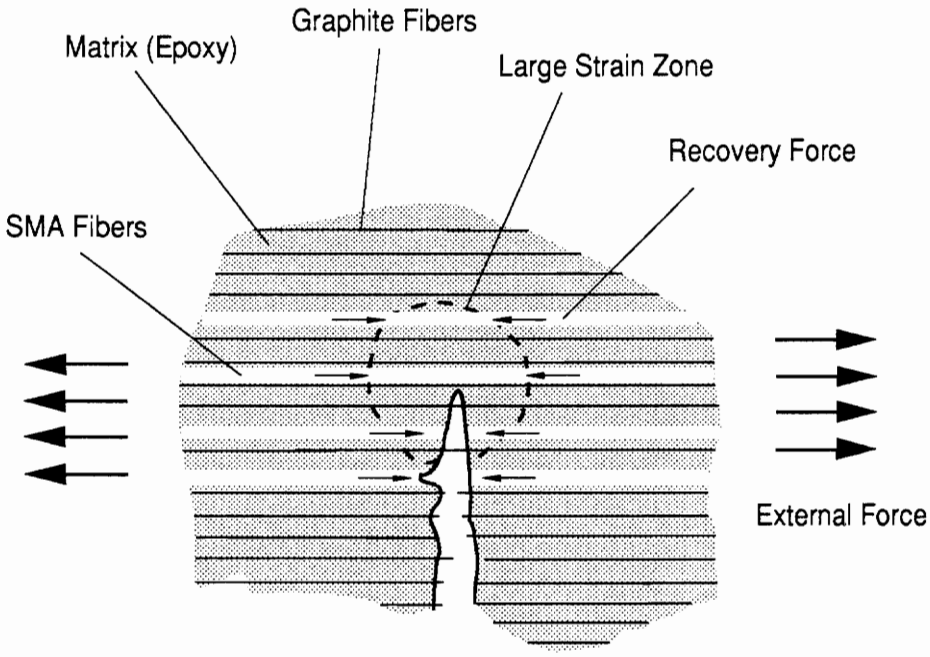

Figure 2.3: Schematic diagram of the operating mechanism of active damage control using SMA.

the crack can be slowed or hindered. This approach relies on the deformation of the composite matrix and the crack opening to inelastically elongate the embedded SMA actuators above some critical strain to generate stress-induced martensitic transformation within the actuator fibers. The critical strain is the elastic strain limit, which, depending on the ambient temperature, ranges from 0.1% to 0.4% for nickel-titanium alloys (Dye, 1990). Brittle composites, such as some of the thermoset composites like graphite/epoxy, cannot generate this amount of deformation. The stress induced martensitic transformation will result primarily from the crack opening. However, the ultimate elongation of most thermoplastic composites, for example, Fluorocarbon ETFE thermoplastic carbon fiber composite, can reach up to 5% (DATA INC., 1987). Both matrix deformation and crack opening will contribute to the phase transformation in SMA actuators.

To quantitatively calculate the activation effect of SMA actuators, the analysis of fracture mechanics must be combined with the nonlinear constitutive model of SMA presented by Liang and Rogers (1990). A brief review of the constitutive model of SMA is given below. More detailed discussions of shape memory alloys can be found in earlier published literature (Liang, 1990).

The constitutive relation of shape memory alloys can be expressed as:

$$\sigma-\sigma_0=D(\epsilon-\epsilon_0)+\Omega(\xi-\xi_0)+\theta(T-T_0) \ , \tag{2.1}$$

where D, Ω, and θ are the Young's modulus, phase transformation tensor, and thermoelastic tensor, respectively. σ is the stress, ϵ the strain, and ξ the martensitic fraction, which can be obtained phenomenologically as:

$$\xi=\frac{1-\xi_A}{2}\cos[a_M(T-M_f)+b_M\sigma]+\frac{1+\xi_A}{2} \ , \tag{2.2}$$

for martensitic phase transformation, and

$$\xi=\frac{\xi_M}{2}\{\cos[a_A(T-A_s)+b_A\sigma]+1\} \tag{2.3}$$

for the reverse transformation. a_A, a_M, b_A, and b_M are material constants derived from the four transition temperatures: M_f (martensitic finish), M_s (martensitic start), A_s (austenitic start), and A_f (austenitic finish); and the stress influence coefficients which describe how the transition temperatures vary with stress. The quantities, ξ_A and ξ_M, are the initial martensitic fractions for each transformation process.

The constitutive equations can provide quantitative description and prediction of the stress-strain relations and shape memory effects of SMAs, including recovery stress vs. temperature and recovery strain vs. temperatures, by utilizing different initial conditions and Eq. (2.2) or Eq. (2.3). These equations will be employed in the theoretical modeling of bridging SMA fibers.

2.2 Experiments on Active Crack Damage Control

Photoelastic techniques were used to study the mechanism of active damage control of embedded SMA actuators. The experiments were conducted by using specimens of PLM-9 photoelastic epoxy with embedded Nitinol fibers (0.381 mm dia.), as shown in Fig. 2.4. The material properties of the photoelastic epoxy are listed in Table 2.1.

Nitinol (55% Ni, 45% Ti) SMA wires were used as the induced strain actuators and embedded in the photoelastic specimens. The characteristic transformation temperature (A_s) of the Nitinol is about 34.5°C. Recovery stress was generated by heating the inelastically elongated Nitinol wire above its transition temperature. The recovery stress of the restrained SMA wire reached the maximum value when the Nitinol wire was heated above 60°C. Two symmetric cracks were opened and the SMA actuators were about 0.5 mm in front of the cracks. A constant tensile load of 222.41 N (50 lbf) was applied to the specimen. The embedded SMA actuator was activated by resistive heating. A thermocouple was attached on the SMA wire outside the epoxy specimen to monitor the temperature of the SMA actuators. The maximum temperature of the external portion of the SMA actuator was about 60°C when it was considered to be fully activated.

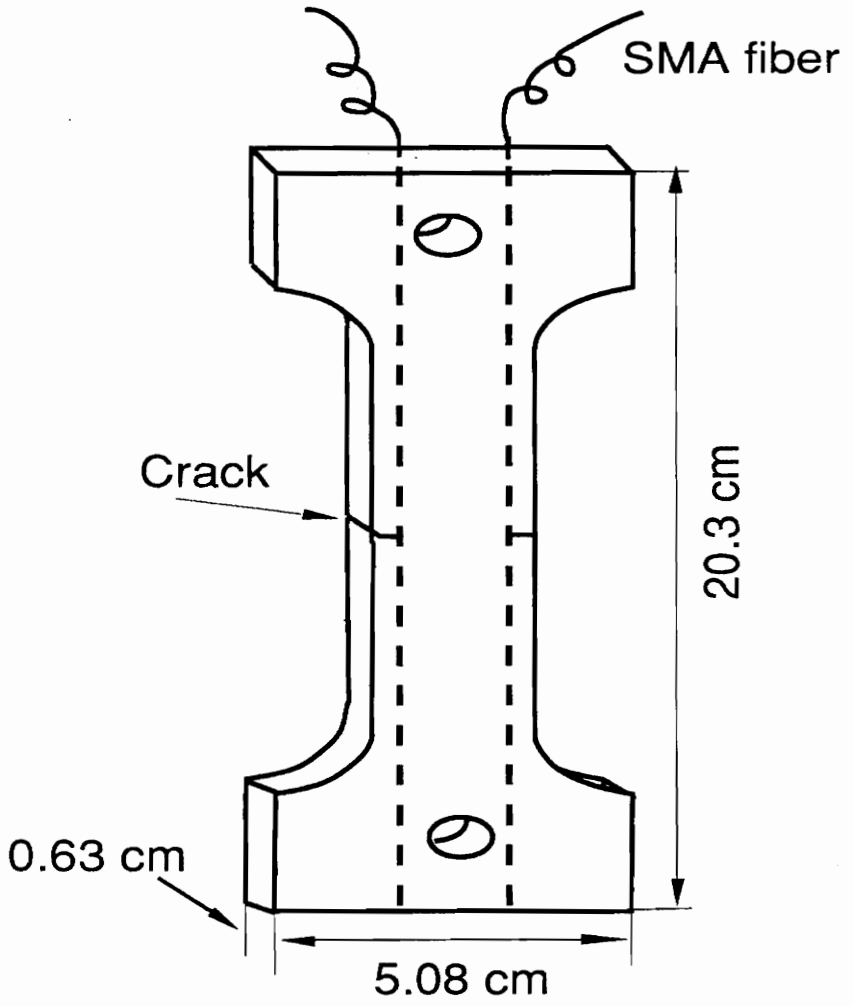

Figure 2.4: Photoelastic epoxy test specimen with SMA actuators embedded to control the stress intensity factor of the crack.

Table 2.1. Material Properties of PLM-9 Epoxy

T °C	E MPa	f' KPa/fringe/in	σ_b Mpa	α PPM/°C	γ
22(Room)	3309.5	10.5	51.71	396	.36

The pictures of the photoelastic fringe patterns at the crack tip were taken when the SMA wires were at both room temperature (22°C) and in the fully actuated state, i.e., at approximately 60°C. Since the material properties of the photoelastic epoxy are sensitive to temperature (60°C is sufficient to induce significant change in the elastic modulus of photoelastic epoxy material), the heating was accomplished in a very short period of time (0.1 sec.) so that the bulk specimen temperature and the material properties of the bulk epoxy material did not change significantly.

Since photoelastic epoxy material is elastic, brittle and of relatively low modulus, it could not induce the required strain for stress-induced martensitic phase transformation (0.2% at least for the Nitinol material that was used (Dye, 1990)). Therefore, the section of the embedded SMA actuator close to the crack tip was prestrained to 5% before it was embedded in the epoxy specimen. However, as discussed in the Introduction, some composite materials, such as thermoplastic composites, are capable of inducing a large strain in the embedded SMA actuators through material interaction. The photoelastic pattern of the specimen was photographed at two actuator fiber temperatures (22°C and 60°C). Figure 2.5 shows the fringe pattern of the entire specimen (inactivated (a) and activated (b)). The enlarged picture of the fringe pattern at the crack tip is shown in Fig. 2.6. Figure 2.6 (a) shows the fringe pattern before activation of the embedded SMA actuator and Fig. 2.6 (b) shows the fringe pattern after the embedded fiber actuator has been activated. The change in the fringe pattern, illustrated in Figs. 2.6 (a) and (b),

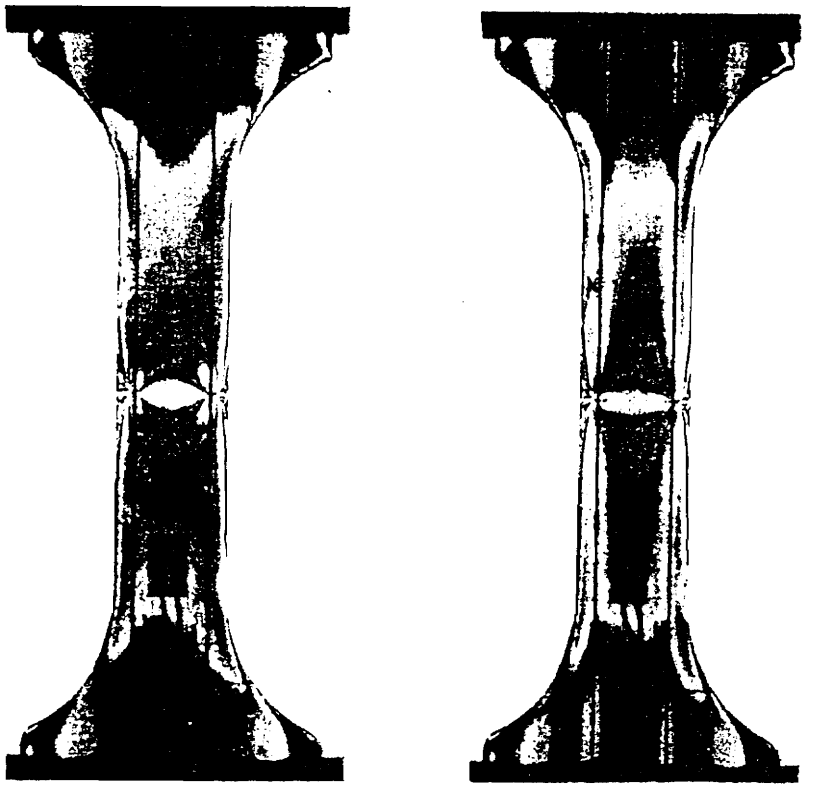

Figure 2.5: Fringe patterns of the photoelastic epoxy test specimen for both inactivated (a) and activated (b) cases.

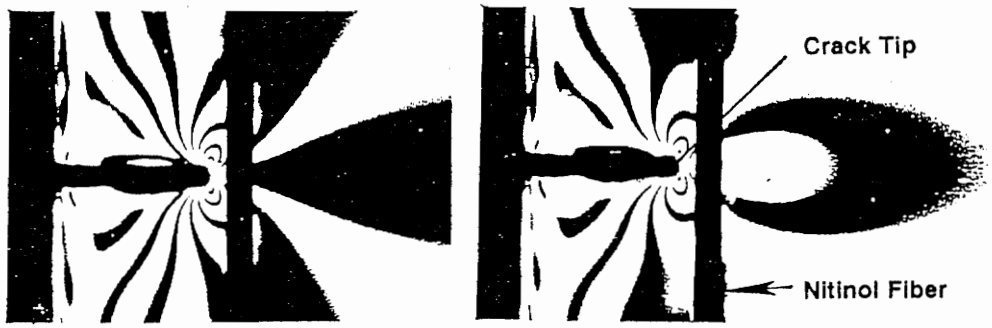

Figure 2.6: Fringe pattern at the crack tip of the photoelastic epoxy test specimen.

clearly indicates the reduction in the stress concentration at the crack tip. According to the theory of photoelasticity, the fringe order is directly related to the maximum shear stress and, therefore, to the stress intensity factor at the crack tip area. From the fringe order, the stress intensity factor can be determined (Dally and Riley, 1985) by:

$$\frac{K_{AP}}{\sigma(\pi c)^{1/2}} = \frac{K_I}{\sigma(\pi c)^{1/2}} + \frac{f(\sigma_{ij}^0)}{\sigma}\left(\frac{r}{c}\right)^{1/2}, \tag{2.4}$$

where $f(\sigma_{ij}^0)$ are a set of constants, $K_{AP}=\tau_{max}(8\pi r)^{1/2}$ is related to the maximum shear stress, r is the distance measured from the crack tip, σ is the normal stress far away from the crack, and "c" is the length of the crack. The photoelastic stress-optic law states:

$$\tau_{max} = \frac{Nf'}{t}, \tag{2.5}$$

where N = photoelastic stress fringe order

t = model thickness

f′ = material fringe coefficient.

The stress intensity factor K_I can be solved by substituting Eq. (2.5) into Eq. (2.4). The stress intensity factor of the inactivated specimen is calculated as 11.20 $[N/(mm)^{3/2}]$. The stress intensity factor of the crack is decreased to 8.47 $[N/(mm)^{3/2}]$ when the embedded SMA actuator is activated. The total reduction in the stress intensity factor is about 2.73 $[N/(mm)^{3/2}]$ (about 24%).

2.3 Finite Element Analysis of Active Crack Damage Control

Experimental studies have shown that activation of SMA fiber actuators embedded in test specimens changes the stress and strain distribution, resulting in a reduction in the stress intensity factor. Preliminary numerical analyses have been conducted and some of the results are presented here.

The finite element analysis was carried out using the finite element program ABAQUS. Only a quarter of the test specimen was modeled according to symmetric geometric and loading conditions. The 2-D finite element mesh is shown in Fig. 2.7. The shaded elements shown in Fig. 2.7 represent the embedded SMA actuator. Since the diameter of the SMA actuator is only one tenth of the thickness of the test specimen, an equivalent stiffness was used for the elements that represent the SMA actuator. The Young's modulus of the Nitinol alloy is 26.3 GPa (Liang, 1990), while the equivalent stiffness used for the actuator elements is given by:

$$E_e = \left(\frac{d}{t}\right)E_A + \left(\frac{t-d}{t}\right)E_m \,, \tag{2.6}$$

where t is the thickness of the specimen, d the diameter of the SMA actuator, E_A the Young's modulus of the SMA actuator, and E_m the elastic modulus of the matrix.

The portion of the SMA fiber actuator close to the crack tip was assumed to be

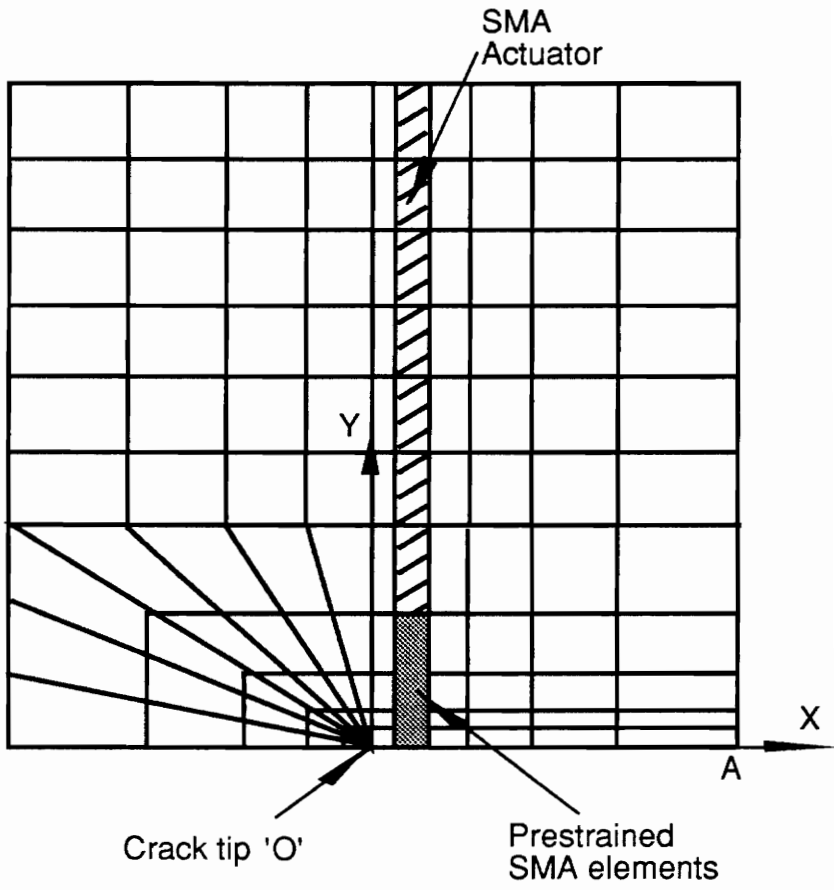

Figure 2.7: Finite element mesh.

prestrained to 5%, as described in the experimental section. The prestrained actuator elements are marked and shown in Fig. 2.7.

Once the prestrained SMA fiber actuator is activated by resistive heating above A_s, the recovery stress-strain-temperature is completely different from the original stress-strain relation. It is necessary to specify different constitutive relations for the prestrained actuator elements. Liang and Rogers (1989) and Lin and Rogers (1991) have presented detailed discussions concerning the constitutive modeling of shape memory alloys and SMA hybrid composites. Here, a simple and effective way of modeling the recovery stress-strain relations is proposed. From the experimental results of the recovery effects of SMA fibers, shown in Fig. 1.2, the interactive recovery stress-strain relations may be considered linear for a certain matrix stiffness, but the slopes of the curves are negative. When only the activation effect in the matrix is considered, the recovery results for SMA actuators are similar to those for the thermal contraction of materials. Therefore, the recovery force is incorporated into the finite element model by utilizing the thermal contraction model. In the model, the thermal expansion coefficients of the matrix (epoxy) and the unstrained portion of the SMA fiber actuator are neglected, and the thermal expansion coefficient of the prestrained SMA actuator elements has a negative magnitude. When the SMA actuator is activated upon being heated (this was done in the program by assuming a temperature increment of ΔT), the tensile force generated in the prestrained SMA actuator elements due to thermal contraction has the same effect on

the crack tip stress distribution as the actual recovery force.

In the experimental study, the SMA actuator was heated from 22°C to 60°C. The restrained recovery stress, σ_{r_0}, was about 85 Ksi, and the prestrain for the SMA actuator was approximately 5%. In the finite element calculations, the following assumptions were used: ΔT=38°C (from 22°C to 60°C) and the equivalent thermal expansion coefficient of prestrained SMA elements was determined to be α_A = -5%/ΔT = -0.001316 m/m/°C. The equivalent modulus of the prestrained SMA elements, E'_A, can be calculated from:

$$-E'_A \times \alpha_A \Delta T = \sigma_{r_0} . \tag{2.7}$$

E'_A was calculated to be 11721 Mpa, (1700 Ksi). It should be noted that the nonlinear recovery stress and strain relation is replaced with a linear thermal expansion model which will inevitably introduce some error. Considering the 2-D simplification of the finite element model, the actual equivalent modulus used for the prestrained SMA actuator elements, E_{Ae}, was calculated from:

$$E_{Ae} = \left(\frac{d}{t}\right)E'_A + \left(\frac{t-d}{t}\right)E_m . \tag{2.8}$$

A parametric study using the finite element results has been completed. Shown in Fig. 2.8 is the stress distribution (σ_y) along OA (shown in Fig. 2.7). In Fig. 2.8, the crack tip is at x=5 (mm), and the embedded SMA fiber actuator is 0.5 mm away from the

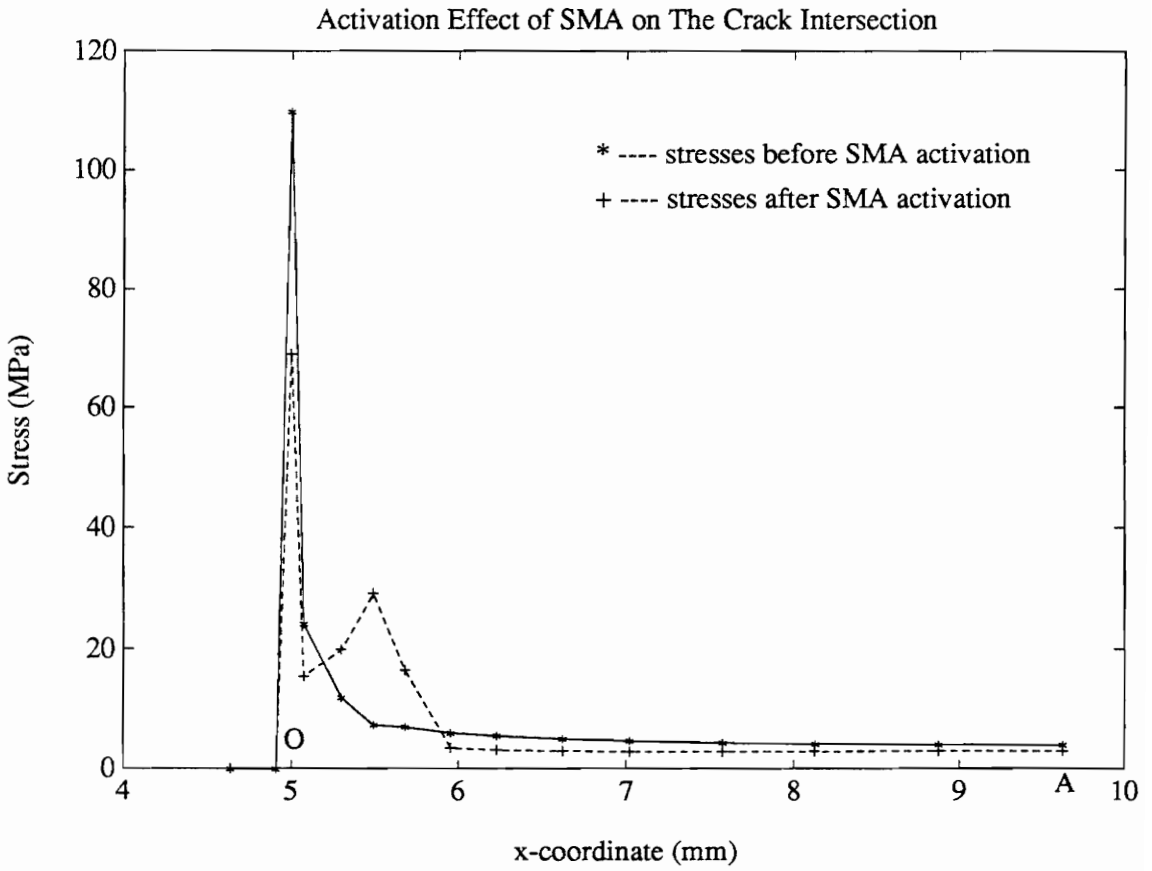

Figure 2.8: Stress distribution (MPa) along OA (distance in mm).

crack tip. The solid line shows the stress distribution before activating the embedded SMA actuator. A large stress concentration is shown occurring at the crack tip. The dotted line shows the stress distribution after activating the SMA fiber actuator. The second peak on the dotted line indicates the activation of the SMA actuator. The stress at the crack tip has been reduced significantly. Before activation, the peak stress at the crack tip is 110 (Mpa). This peak stress is reduced to 69 (Mpa) after activating the embedded SMA actuators. Although statistical analysis was not performed, the results do show that activation of the embedded SMA actuator can significantly reduce the stress concentration at a crack tip, thereby yielding a reduction in the stress intensity factor.

The stress intensity factors were also calculated. The stress intensity factor has the following relation with the J-integral, J:

$$K_I = \sqrt{J E_m}\ , \tag{2.9}$$

where E_m is the modulus of the photoelastic epoxy. The J-integral was calculated using the ABAQUS finite element program. The finite element results and experimental results are calculated and listed in Table 2.2. The finite element results are very close to the experimental results considering the approximations made in using a 2-D finite element model and the simplification of the recovery stress-strain relationship.

Some parametric studies have been completed. Shown in Fig. 2.9 is the influence of the

Table 2.2. Comparison of Experimental and Finite Element Results

Specimen	Experimental K	F.E.M. K
T=22 C	11.20	11.60
T=60 C	8.467	8.355
Δ K (%)	2.733 (24.4%)	3.078 (27.97%)

embedded SMA actuator fraction on the reduction in the stress concentration at the crack tip. As indicated by Eqs. (2.6) and (2.7), increasing the number of SMA fiber actuators at a crack tip will increase the equivalent stiffness of the actuator element, resulting in a decrease in the stress concentration at the crack tip. The change in the peak stress (inactivated peak stress - activated peak stress) increases as a function of the volume fraction of the embedded SMA actuators (d/w).

Shown in Fig. 2.10 is the change in the stress intensity factor as a function of the relative stiffness of the SMA actuator and the matrix material. The stiffness of the SMA actuator, E_A, is calculated from Eq. (2.7). The results show that with increasing matrix stiffness, the reduction in the stress intensity factor will increase. This is a result of the higher compressive forces generated by the embedded SMA actuators (less recovery for the SMA actuator will generate a higher recovery force in the actuator, a higher recovery force in the actuator will produce the same amount of reactionary compressive force in the matrix).

The experimental results and finite element analysis demonstrate that the activation of an SMA fiber greatly changes the stress concentration at the crack tip even when the fiber is located in front of the crack tip. In this configuration, the activation forces are applied to the area in front of the crack tip. If the fiber bridges the crack, the activation force will apply to the upper and lower surfaces of the crack, which can also decrease the

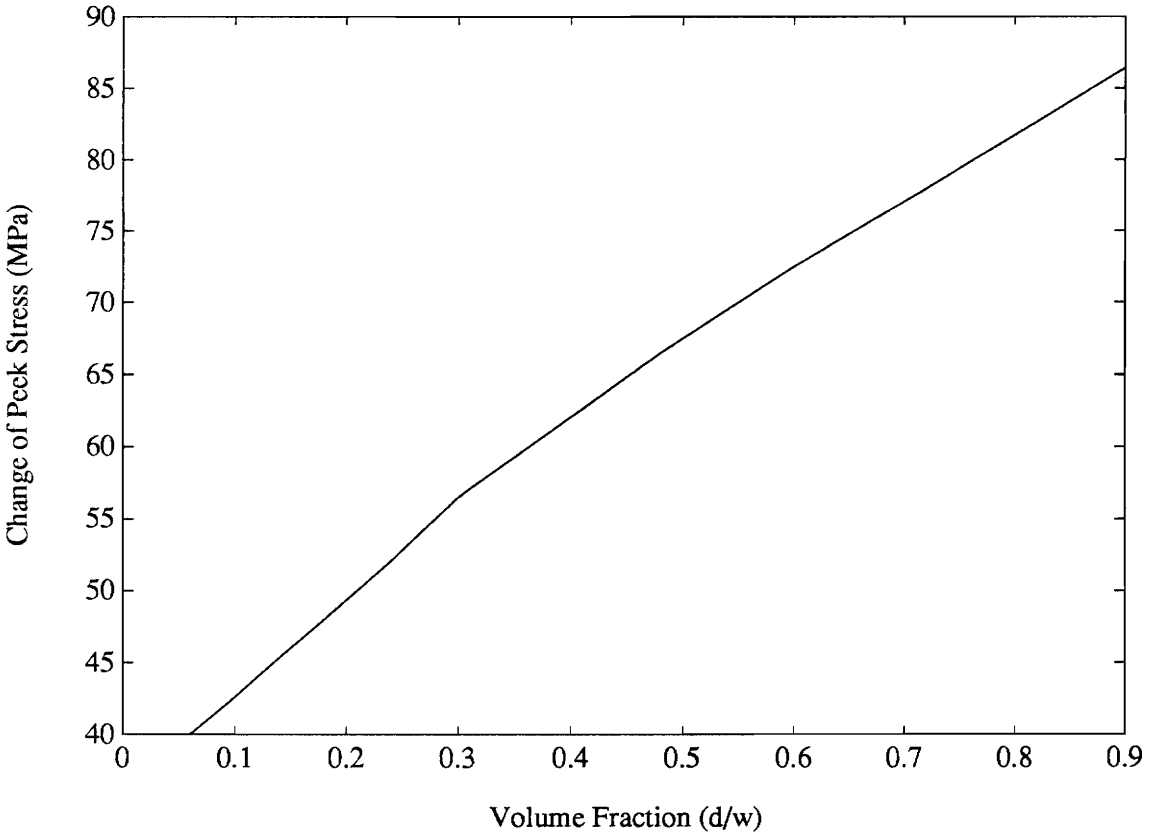

Figure 2.9: Change in the peak stress at the crack tips vs. the volume fraction of the embedded SMA actuators, (d/w).

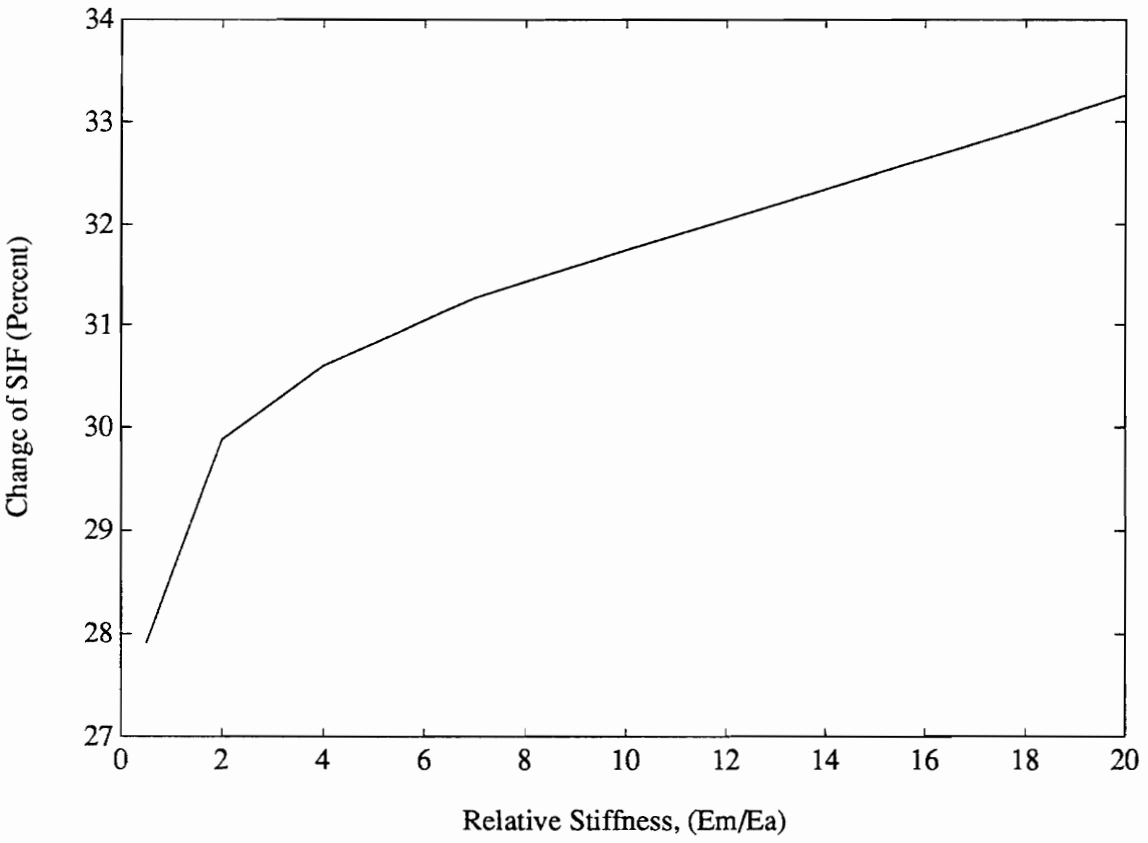

Figure 2.10: Change in the stress intensity factor at the crack tips as a function of relative stiffness, (E_A/E_m).

stress concentration at the crack tip. In the next section, a mechanical model of an SMA bridged crack will be formulated which considers the pulling-out and the activation effects of bridging SMA fibers.

2.4 Theoretical Model of Virgin Nitinol Fiber in Bridging Case

The fracture modes of composites are far more complicated than those of homogeneous and isotropic materials. The embedded SMA actuators can only be effective in controlling the damage of a certain damage mode, such as matrix cracking perpendicular to the SMA fibers with the fibers bridging the crack. This section will model the active damage control of this special damage mode.

2.4.1 Mechanism of Active Crack Damage Control in Bridging

Before the introducing of the mechanism of active crack damage control, it is necessary to introduce the bridging case. The bridging case can be formed by two processes. In a unidirectional composite of long, continuous SMA fibers aligned parallel to an applied load, the cracks form perpendicular to the fiber direction. Under tensile loads or cyclic tensile loads, a small crack forms in the matrix between fibers. Load, once carried by the matrix, is transferred by shear to the fibers which are still intact. This shear force eventually becomes so large that the bond between the fiber and the matrix fails. A

cylindrical crack at the interface propagates along the length of the fiber as the applied load increases. This process is called debonding. Because of the good plasticity of SMA fibers (elongation at failure can be as high as 30%, and the maximum recoverable strain can be up to 8.5%), the matrix crack passes through the fibers leaving the fibers intact as the debonding occurs. On the other hand, in the debonded areas, some load transfer between the fiber and the matrix is still possible due to interfacial friction. The forces originally in the cracked matrix now are transferred to the fibers, and the debonded portions of the fibers are further stretched. The composite contains a matrix crack-plane with fibers protruding from it. This process is called pull-out. The above two processes result in bridging, as shown in Fig. 2.11.

The mechanism of active damage control in the case of bridging case can be illustrated as follows: in the pull-out period, the SMA fibers will toughen the matrix, and the high stress in the fiber (the stress level is related to the load level and the volume fraction) will pull the fiber into activation ready state (martensitic phase transformation). Then, by activating the SMA actuators through heating, the debonded portions of the SMA actuators will try to recover to their original lengths (the closure state of the crack). Because of the constraint between the crack body and the SMA fibers, the activation forces will be generated in SMA fibers and in the crack body. The contraction forces generated by SMA fibers will be applied to the upper and lower crack surfaces, resulting in closing of the crack and reduction in the stress intensity at the crack tip.

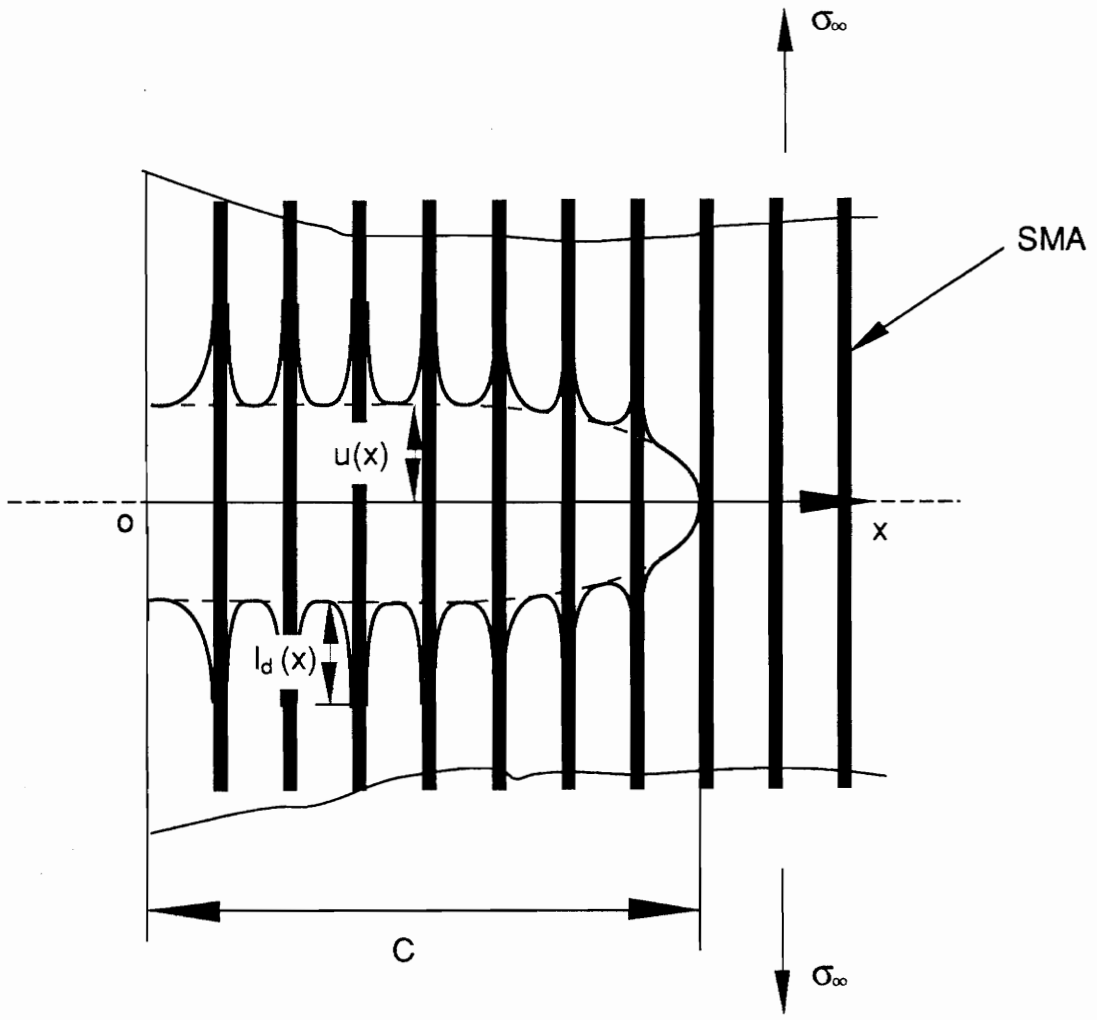

Figure 2.11: Simplified model of a crack in SMA composites which is perpendicular to the embedded SMA fibers.

An important parameter that affects the activation effect is the interfacial strength between the fibers and the matrix, which determines the debonding length of the SMA fibers. If the interfacial strength is very high, or the debonding length is very short, the fiber strain in the debonded part will be very high, resulting in fiber breakage. Conversely, if the interfacial strength is very low or the debonding length is very long, the strain in the debonded part will be very small. The strain may not be big enough to induce martensitic phase transformation, or may just induce a small amount of martensitic phase transformation, and the activation will not be powerful. Fortunately, the interfacial strength between the SMA fibers and the matrix, which is a function of fiber diameter, surface treatment, and material properties, etc., is adjustable. Therefore, the pull-out strain in the debonded part is also adjustable. Further experiments are needed to determine the parameters to achieve the suitable amount of tensile strain in the bridging section.

In addition to a phenomenological analysis, a mechanical expression for the debonding length is helpful in understanding the mechanism of debonding. A mechanical analysis of the debonded length of SMA pull-out will be performed in the next section.

2.4.2 Analysis of the Debonding Length of Nitinol Fibers

The opening of a matrix crack which is bridged by SMA fibers requires some sliding and

debonding between the fibers and the matrix. In the present analysis, there is no chemical bond between the fibers and the matrix, and the sliding of the matrix over the fibers is resisted only by friction. Figure 2.11 shows a simplified model of a crack perpendicular to the embedded SMA fibers. Since the SMA is extremely ductile, a crack will propagate through the SMA fibers without breaking them. Each bridging fiber will have a debonding length $l_d(x)$ which is a function of x, as shown in Fig. 2.11. Wells and Beaumont (1985) gave an expression of debonding length based on the nonlinear model, and Piggot (1991) showed a detailed derivation of fiber stress vs. debonding length. However, according to the author's analysis (which is similar to Piggot's derivation, but in which the assumption and free body analysis are significantly different), different results are obtained. The derivation is given as follows. For a fiber which is partly debonded from a matrix, the force arrangement and the free body diagram are shown in Fig. 2.12. Considering the stress distribution at the debonding point, the fiber force is σ_d, the fiber shrinking force perpendicular to the fiber is $\nu_s\sigma_d$ where ν_s is an effective Poisson's ratio defined later, and the compressive force between the fiber and matrix is P_0. There is no shear force, τ, on the interfacial surface now. After debonding, a shear force, τ, is generated, as shown in Fig. 2.12, and the magnitude is related to the normal compression on the sliding surface and the friction coefficient. The normal compression consists of the pressure, P, and the further shrinking force, $(\sigma_f-\sigma_d)\nu_s$. Note the further shrinking force is not $\sigma_f\nu_s$. Since the fiber has already decreased in diameter due to the Poisson effect of σ_d before debonding, σ_d will have no contribution to the further

shrinkage after debonding. Therefore, the shear stress can be expressed by $\tau=[P-\nu_s(\sigma_f-\sigma_d)]\mu$, where μ is the frictional coefficient. Based on the above analysis and the free body diagram, shown in Fig. 2.12, the force balance along the fiber direction, x, is given by:

$$\sigma_f(\pi r^2) - [\sigma_f + \frac{d\sigma_f}{dx}dx](\pi r^2) - [P-\nu_s(\sigma_f-\sigma_d)]\mu(2\pi r dx) = 0 . \qquad (2.10)$$

This equation can yield the governing equation:

$$\frac{d\sigma_f}{dx} = -\frac{2\mu}{r}[P-\nu_s\sigma_f+\nu_s\sigma_d] . \qquad (2.11)$$

Solving the differential equation and integrating over the whole debonded fiber length gives:

$$\sigma_f = \frac{P}{\nu_s}\left(1-e^{-\frac{2\mu\nu_s}{r}l_d}\right) + \sigma_d . \qquad (2.12)$$

By rewriting the equation, the debonding length is obtained:

$$l_d(x) = -\frac{1}{\beta}\ln\left[1-\frac{\nu_s}{P}(\sigma_f-\sigma_d)\right] , \qquad (2.13)$$

where $\beta=2\mu v_f E_m/r(1+v_m)E_f$ is a function of SMA fiber volume fraction, v_f, matrix volume fraction, v_m, and Young's modulus of matrix and fiber, E_m and E_f, respectively.

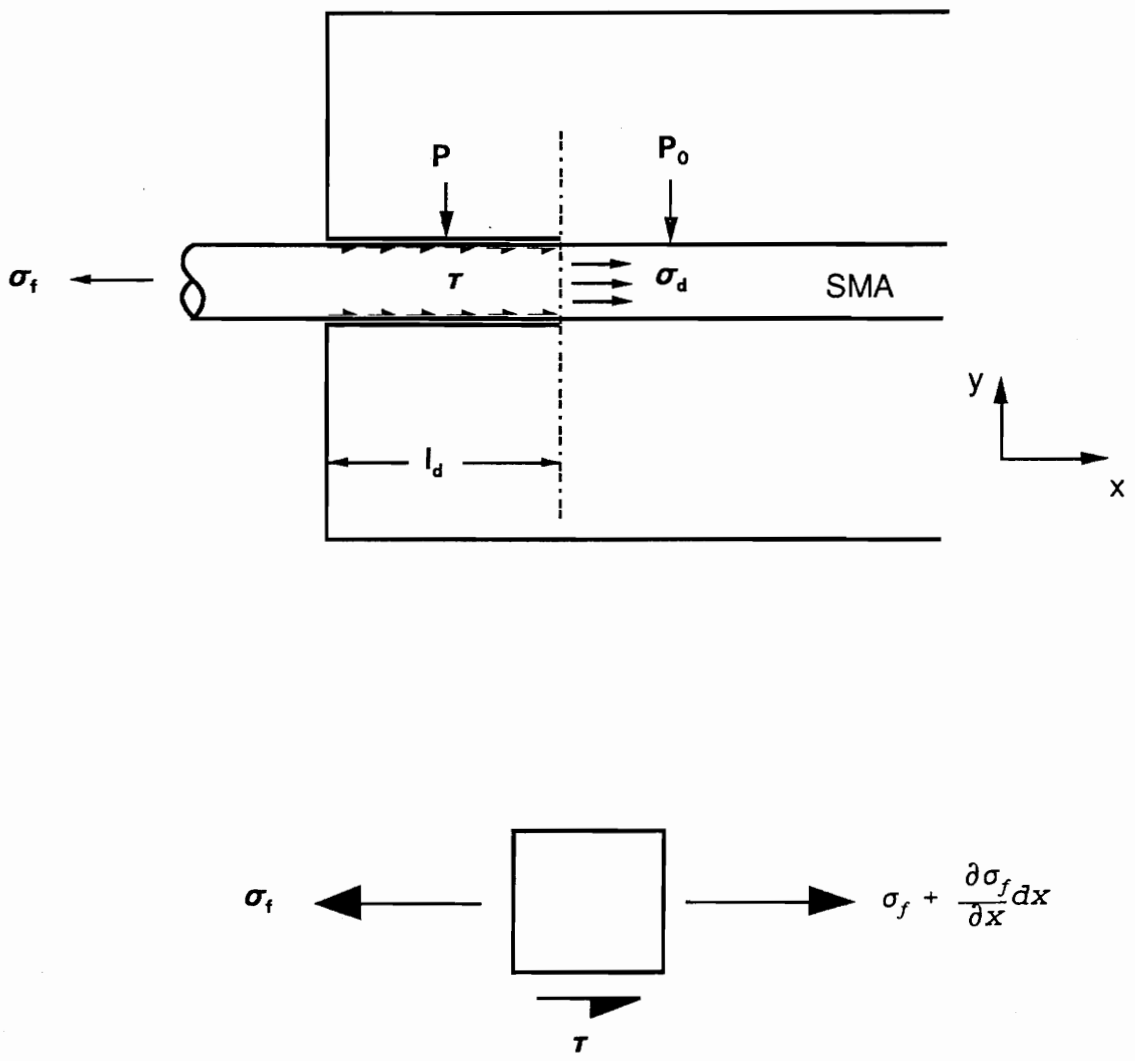

Free Body Diagram of SMA

Figure 2.12: Stress distribution on partly debonded fiber and the free body diagram of the debonded part.

σ_f is the normal fiber stress for each bridging fiber, σ_d is the normal pull-out strength of SMA fibers, P is the radial pressure across the interface, and $\nu_s=\nu_f E_m/(1+\nu_m)E_f$. To verify the debonding length expression, experiments were performed with SMA fibers of 15 mil diameter embedded in photoelastic epoxy PLM-9. The experimental points and the theoretical curve of the debonding length with respect to fiber forces are drawn in Fig. 2.13. The curve is drawn according to the theoretical model, and assuming that σ_f=300 Mpa, $\nu_m=\nu_f$=0.3, P=20 Mpa, and μ=0.2. The "*'s" represent the experiment points. The experiments show good agreement with the theoretical model of debonding length.

2.4.3 Theoretical Modeling of the Pull-Out of SMA Fibers in Bridging Case

The strain of each bridging SMA fiber can be described as

$$\epsilon_f=\frac{u(x)}{l_d(x)} \quad , \tag{2.14}$$

where u(x) is the crack opening displacement. The fiber stress, σ_f, and strain, ϵ_f, are governed by the constitutive relationship of SMA, as given by Eq. (2.1).

The stresses applied by an SMA fiber to a crack can be analyzed as two steps, shown in Fig. 2.14. First, all of the bonds across the crack plane (in the fibers and matrix as well) are cut, and the stress σ_∞ is applied, (Fig. 2.14(a)), causing the crack to open. In the

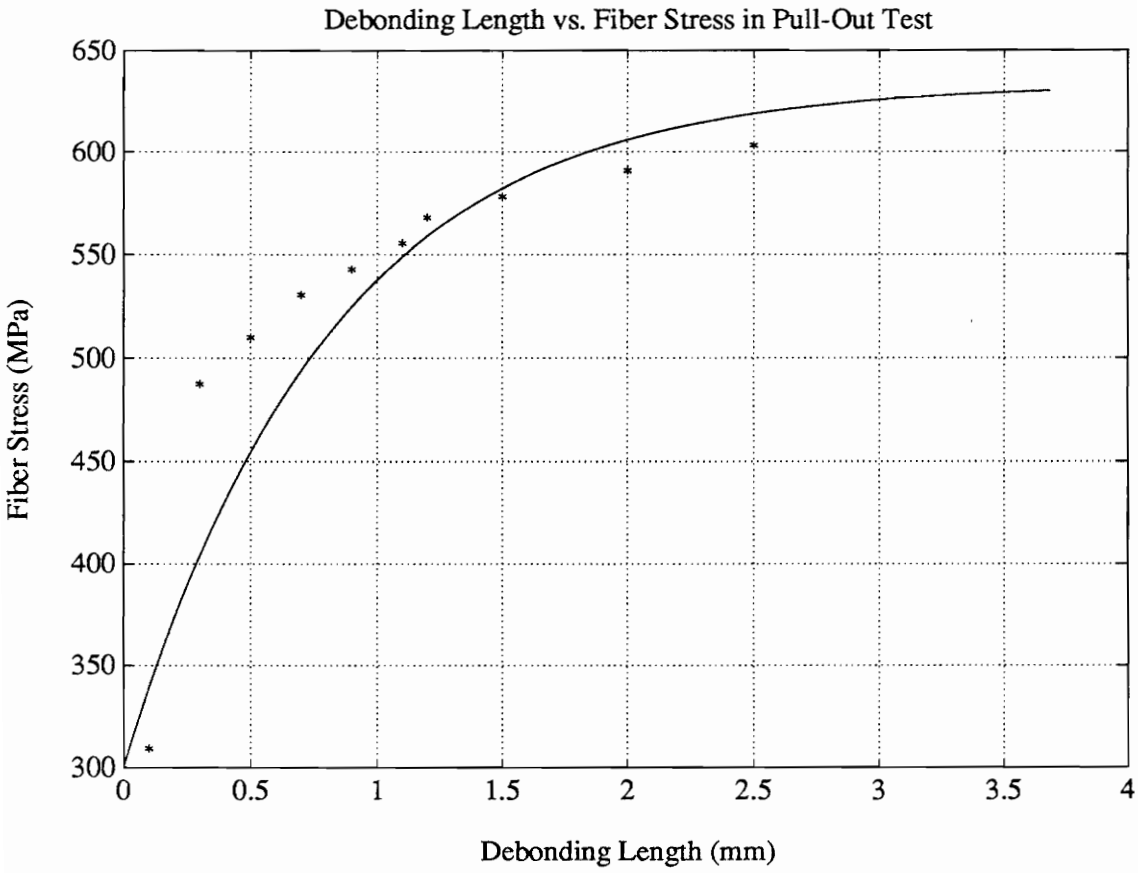

Figure 2.13: Debonding lengths vs. fiber forces from pull-out tests on SMA fibers.

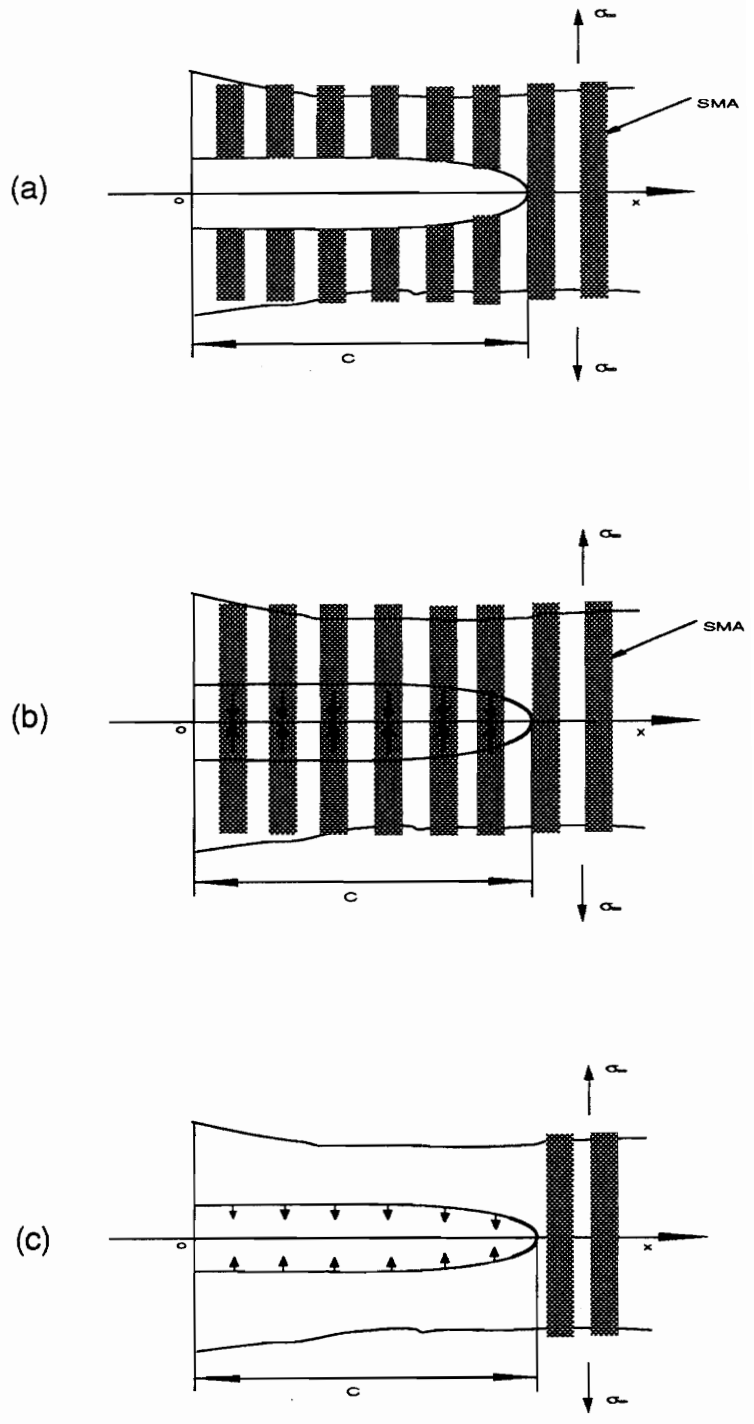

Figure 2.14: Equivalent mechanical model of SMA bridged crack.

second step, traction stresses, σ_f, are applied to the end of each fiber. The magnitude of σ_f is chosen such that the fiber ends displace relative to the matrix and cause the fibers to be rejoined, shown in Fig. 2.14(b). In this analysis, the fiber stresses, σ_f, are distributed as traction stresses on the crack surfaces. In a continuum approximation (c>> fiber space), the effect of the bridging SMA fibers can be represented by a uniformly distributed surface traction, p(x), as shown in Fig. 2.14(c). The surface traction can be expressed as:

$$p(x)=\sigma_f \nu_f \ , \tag{2.15}$$

where ν_f is the volume fraction of the fibers.

Substituting Eqs. (2.13), (2.14), and (2.15) into the constitutive relations of SMA given by Eq. (2.1) to solve for the crack opening displacement yields:

$$u(x)=-\frac{1}{\beta E_f} ln(1-\frac{\nu_s}{P}(\frac{p(x)}{\nu_f}-\sigma_d))\left[\frac{1}{\nu_f}(p(x)-p_0(x))-\Omega(\xi-\xi_0)-\Theta(T-T_0)\right] \\ -\frac{1}{\beta} ln(1-\frac{\nu_s}{P}(\frac{p(x)}{\nu_f}-\sigma_d))\epsilon_0 \tag{2.16}$$

The expression for the martensite fraction can be obtained by substituting Eq. (2.15) into Eqs. (2.2) and (2.3). The equilibrium condition and geometric compatibility will yield another expression for the crack opening displacement, u(x), as follows (Sneddon et al., 1969):

$$u(x) = \frac{4(1-\nu^2)c}{\pi E_c} \int_x^1 \frac{s}{\sqrt{s^2-X^2}} \int_0^s \frac{[\sigma_\infty - p(t)]dt}{\sqrt{s^2-t^2}} ds \ , \qquad (2.17)$$

where c is the crack length, and X equals x/c. σ_∞ is the external loading and E_c is the equivalent modulus of the SMA composites given by:

$$E_c = E_f v_f + E_m v_m \ . \qquad (2.18)$$

Substituting Eq. (2.16) into Eq. (2.17) to eliminate u(x) will yield an integration equation in terms of an unknown function p(x). Once the surface traction p(x) is solved, the stress intensity can be calculated from the following equation (according to Lawn (1975) and Sih (1973)):

$$K^L = 2(c/\pi)^{1/2} \int_0^1 \frac{[\sigma_\infty - p(X)]dX}{\sqrt{1-X^2}} \ , \qquad (2.19)$$

where X equals x/c.

The inactivated tension and activated tension have different characteristics and modeling. In the inactivated tension stage, SMA fibers absorb the crack energy, and generate martensitic phase transformation in the bridging section. The tension force in SMA fibers is directly related to the structural loading. While in the activated tension period, the SMA actuators transform heat energy into mechanical energy, and apply this energy

to the crack surfaces. The summation of the increment of tension force in SMA fibers is balanced with the summation of the increment of compression force in the structure. Therefore, the two periods have to be analyzed separately.

Inactivated Tension Period

It is convenient to analyze large cracks and small cracks separately (Marshall et al., 1985). The characteristic crack length is c_0 from the crack tip. For large cracks (i.e., $c > c_0$), crack growth is referred to as steady-state, and the crack tip stress concentration is determined exclusively by the stress distribution within c_0. For small cracks (i.e., $c < c_0$), the stress concentration and crack growth are dependent upon the crack length.

Steady-state cracks

The schematic stress system for a steady-state crack is depicted in Fig. 2.15. The surface traction, p(x), is balanced by the external loading, i.e., $p(x) = \sigma_\infty$, beyond c_0, and the crack opening traction only exists in the c_0 section. In this region, p(x) can be expressed by the following relationship:

$$p(\rho) = \sigma_\infty f(\rho) \qquad \rho \leq 1 \ , \tag{2.20}$$

where $\rho = r/c_0 = (c-x)/c_0$, and $f(\rho)$ is a function that varies smoothly from zero at $\rho = 0$,

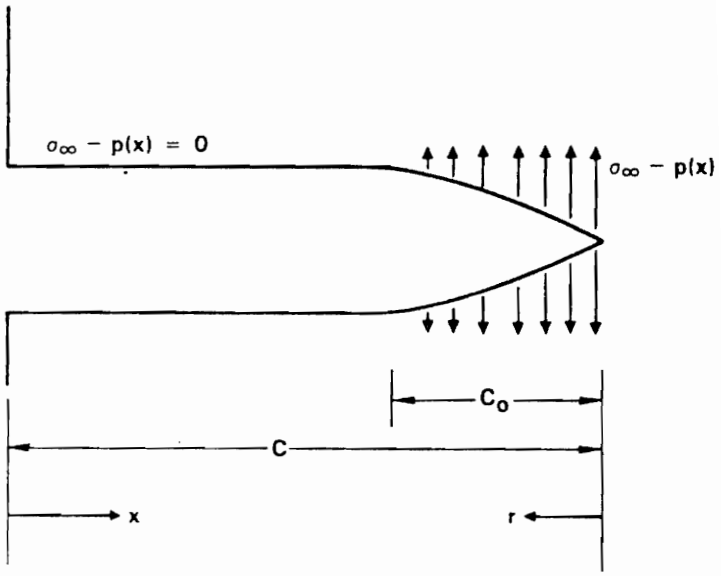

Figure 2.15: Net surface traction acting on a steady-state crack.

to one at $\rho=1$. For steady-state cracks, rewriting Eq. (2.16) for the case of inactivated tension by assuming zero for all initial conditions and that the process is isothermal yields:

$$u(x)=-\frac{1}{\beta E_f}\ln(1-\frac{\nu_s}{P}(\frac{p(x)}{\nu_f}-\sigma_d))\left[\frac{p(x)}{\nu_f}-\Omega\xi\right] , \tag{2.21}$$

where the martensitic volume fraction, ξ, can be expressed as:

$$\xi=\frac{1}{2}\{\cos[a_M(T_0-M_f)+b_M\frac{p(x)}{\nu_f}]+1\} , \tag{2.22}$$

if the ambient temperature, T_0, is above M_s.

The characteristic length c_0 is evaluated by considering the crack opening displacement within the range $r \leq c_0$. For steady-state cracks, Eq. (2.17) becomes:

$$u(x) = \frac{4(1-\nu^2)c_0\sigma_\infty}{\pi E_c}\int_X^1 \frac{s}{\sqrt{s^2-X^2}}\int_0^s \frac{[1-f(t)]dt}{\sqrt{s^2-t^2}}ds . \tag{2.23}$$

Equating Eqs. (2.21) and (2.23) with X=0, f(x)=1, yields:

$$c_0=\nu\frac{-E_c}{\beta E_f\sigma_\infty}\ln(1-\frac{\nu_s}{P}(\frac{\sigma_\infty}{\nu_f}-\sigma_d))\left[\frac{\sigma_\infty}{\nu_f}-\Omega\xi\right] , \tag{2.24}$$

where v is a dimensionless constant:

$$v = \pi/4(1-\nu^2) \int_0^1 \int_0^s \frac{[1-f(t)]dt}{\sqrt{s^2-t^2}} ds \ . \qquad (2.25)$$

Solving Eqs. (2.21), (2.23), and (2.24) yields f(x), and then p(x). The displacement u(x) is determined by substituting Eq. (2.24) and p(x) into Eq. (2.23). The debonding length, $l_d(x)$, and the fiber strain, $\epsilon_f(x)$, are obtained from Eqs. (2.13) and (2.14) separately. The martensitic volume fraction, $\xi(x)$, is given by substituting p(x) into Eq. (2.22). The stress intensity factor expression, Eq. (2.19), then becomes:

$$K^L = 2(c_0/\pi)^{1/2} \sigma_\infty \int_0^1 \frac{[1 - f(X)]dX}{\sqrt{1-X^2}} = w\sigma_\infty C_0^{1/2} \ , \qquad (2.26)$$

where w is another dimensionless constant:

$$w = (4/\pi)^{1/2} \int_0^1 \frac{[1-f(X)]dX}{\sqrt{1-X^2}} \ . \qquad (2.27)$$

Evaluating Eqs. (26) and (24), and setting $\sigma_\infty = \sigma_0$, at $K^L = K_c^M E_c / E^M$ yields:

$$\left[w^2 \nu \frac{E_c \sigma_0}{\beta E_f} \ln\left(1 - \frac{\nu_s}{P}\left(\frac{\sigma_0}{\nu_f} - \sigma_d\right)\right) \left[\frac{\sigma_0}{\nu_f} - \Omega\xi \right] \right]^{1/2} = \frac{K_c^M E_c}{E_M} \ . \qquad (2.28)$$

The critical crack propagation stress, σ_0, can be obtained from this equation.

Short Crack

For short cracks (i.e., $c < c_0$), a rigorous analytical solution cannot be obtained. Instead, an approximate analytical solution is adopted to illustrate the mechanics of crack growth. The approximate solution assumes that for small cracks, the crack profile does not differ greatly from that of a large crack subjected to uniform pressure.

Rewriting u(x) in Eq. (2.17) in terms of K^L yields:

$$u(x) = 2(1-\nu^2)K^L c^{1/2}\left[1-\frac{x^2}{C^2}\right]/E_c\pi^{1/2} \quad . \tag{2.29}$$

This equation is suitable for cracks smaller than c_0 (i.e., $u < u_0$). Combining Eqs. (21), (29), and (19) gives:

$$\frac{4(1-\nu^2)c}{\pi E_c}(1-\frac{x^2}{c^2})^{1/2}\int_0^1 \frac{[\sigma_\infty - p(X)]dX}{\sqrt{1-X^2}} = \frac{1}{\beta E_f}\ln(1-\frac{\nu_s}{P}(\frac{p(x)}{\nu_f}-\sigma_d))\left[\frac{p(x)}{\nu_f}-\Omega\xi\right] \quad . \tag{2.30}$$

From this equation, p(x), which is always smaller than σ_∞, is obtained. On the other hand, p(x) can be approximately considered as the front part of the distribution of a steady-state crack, which satisfies the relationship $p(x) = \sigma_\infty f(x)$ ($1 \geq f(x) \geq 0$). However, the stress intensity factor, K^L, has to be evaluated by Eq. (2.19), which is a function of crack length, c, instead of Eq. (26), which is a function of the crack transforming length, c_0. Then, substituting K^L into Eq. (2.29) will yield the

displacement, u(x), which is always smaller than u_0, and is approximately equal to the front part of the distribution of a steady-state crack. The debonding length, $l_d(x)$, the fiber strain, $\epsilon_f(x)$, and the martensitic volume fraction, $\xi(x)$, can be determined by p(x) and u(x) from Eqs. (13), (14) and (22) separately.

2.4.4 Theoretical Modeling of the Activation of Bridging SMA Fibers

In the activation period, the activation force in the SMA fibers and the force generated in the cracked body yield a self-balanced system. The balanced system of a single activated fiber is shown in Fig. 2.16. The activation force in the SMA fiber is related to structural stiffness, fiber stiffness, martensitic volume fraction, and temperature. The incremental stress distribution in the activation period is independent from that in the inactivated tension period. The final stress distribution is the superposed result of these two periods.

In a continuum approximation ($c >>$ fiber space), the activation force can be represented by a distributed surface traction, q(x), as shown in Fig. 2.17, which satisfies the following relationship:

$$q(x) = \Delta\sigma_f(x)\ v_f\ . \tag{2.31}$$

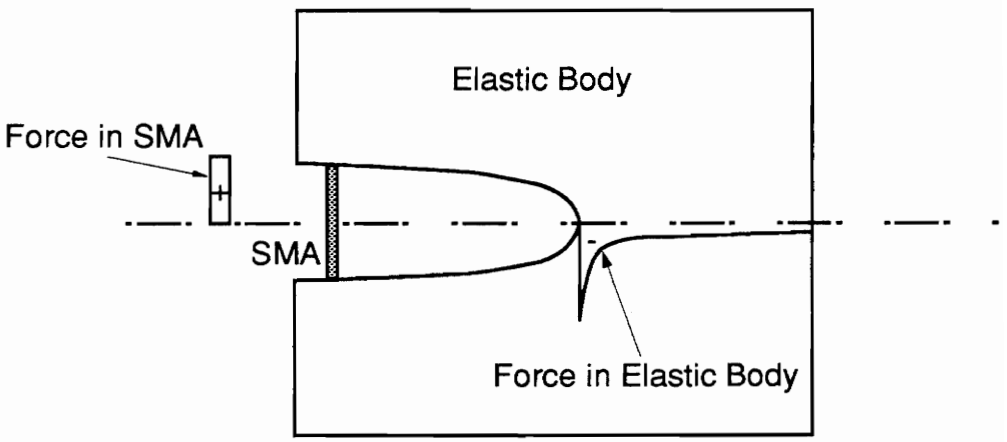

Figure 2.16: Schematic diagram of self-balanced activated system.

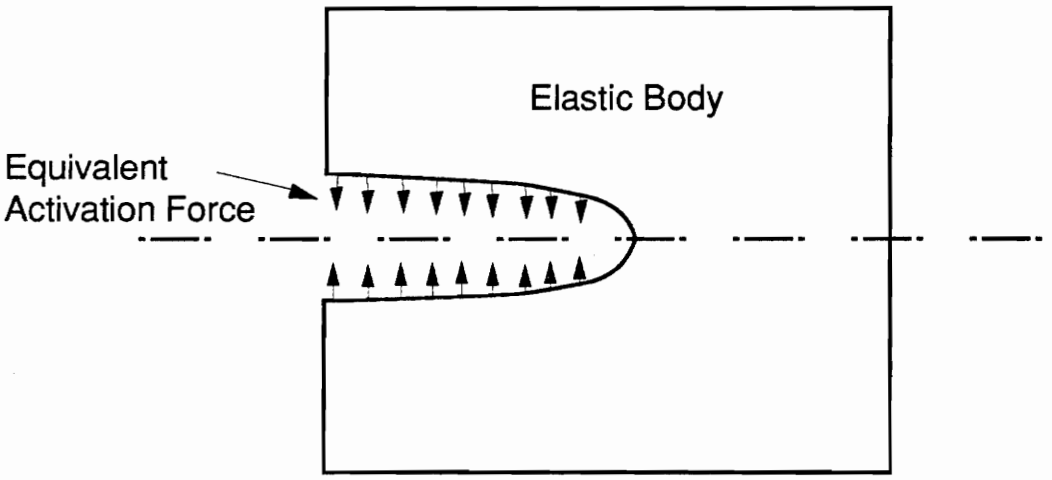

Figure 2.17: Schematic diagram of activated force on a crack.

Since the activation period is the second step, it is convenient to use incremental expressions in the equations. From Eq. (2.17), the change in the crack opening displacement caused by q(x) can be expressed by:

$$\Delta u_c(x) = \frac{4(1-\nu^2)c}{\pi E_c} \int_x^1 \frac{s}{\sqrt{s^2-X^2}} \int_0^s \frac{q(t)dt}{\sqrt{s^2-t^2}} ds \ . \tag{2.32}$$

From the constitutive equation of SMA actuators, Eq. (2.1), the activation force can be represented by:

$$q(x) = (\sigma-\sigma_0)\ v_f = [D(\epsilon-\epsilon_0)+\theta(T-T_0)+\Omega(\xi-\xi_0)]\ v_f \ , \tag{2.33}$$

where the ϵ_0, T_0, and ξ_0 are for the inactivated tension period. ξ is given by Eq. (2.3) for reverse transformation. On the other hand, from the constitutive relationship of an SMA actuator, Eq. (2.1), the change in the length of the SMA actuators is given by:

$$\Delta u(x) = (u-u_0) = \frac{l_d}{D}[(\sigma-\sigma_0)-\theta(T-T_0)-\Omega(\xi-\xi_0)] \ , \tag{2.34}$$

where l_d is determined by Eq. (2.13), in which σ_f is the total fiber force. According to the compatibility of the crack opening and the stretching of SMA fibers, the following relationship can be obtained:

$$\Delta u_c(x) = \Delta u_s(x) \ . \tag{2.35}$$

This relationship is based on the absolute values of the incremental displacements. Substituting Eqs. (2.34), (2.33), and (2.32) into Eq. (2.35) yields:

$$\frac{4(1-\nu^2)c}{\pi E_c}\int_x^1 \frac{s}{\sqrt{s^2-X^2}}\int_0^s \frac{(\sigma-\sigma_0)\nu\beta dt}{\sqrt{s^2-t^2}}ds = \frac{l_d}{D}[(\sigma-\sigma_0)-\theta(T-T_0)-\Omega(\xi-\xi_0)] \quad . \quad (2.36)$$

Using an iteration method, the only unknown variable in the equation, $\sigma(x)$, can be obtained. Then, q(x) can be determined from Eq. (2.33), and $\Delta u_s(x)$, $\Delta u_c(x)$ can be calculated from Eqs. (32) and (34), respectively. The change in the stress intensity factor can be expressed by:

$$\Delta K^L = 2(\frac{c}{\pi})^{1/2}\int_0^1 \frac{-q(X)dX}{\sqrt{1-X^2}} = 2(\frac{c}{\pi})^{1/2}\int_0^1 \frac{-(\sigma-\sigma_0)\nu\beta dX}{\sqrt{1-X^2}} \quad . \quad (2.37)$$

The negative sign represents the decrease in stress intensity after the activation of SMA actuators.

In the activated tension period, the steady-state crack and short crack are analyzed wing the same expression. Because the activation system is a self-balanced one, all distributed forces, q(x), on the crack surface will attend the balance of the system, and contribute to the change in the stress intensity factor. Therefore, in the equations for the activated period, the crack length is expressed by c, either longer or shorter than c_0.

2.4.5 Numerical Results for the Pull-Out and the Activation of Bridging Nitinol Fibers

Numerical solutions for inactivated and activated SMA hybrid composites were obtained. The input data are listed in Table 2.3. To simplify the calculation, the martensitic

volume fraction, ξ, was calculated by the following linear expression (Lin and Rogers, 1991):

$$\xi = \frac{\xi_A}{M_s - M_f}(M_s - T + \frac{\sigma}{C_M}) \ , \tag{2.38}$$

for martensitic phase transformation, and

$$\xi = \frac{\xi_M}{A_f - A_s}(A_f - T + \frac{\sigma}{C_A}) \ , \tag{2.39}$$

for reverse phase transformation. Since the practical debonding length is small, a linear expression is substituted for the original debonding length calculation, Eq. (2.4). For the inactivated tension period, with numerical integration, the crack opening displacement is depicted in Fig. 2.18, with u_0=0.0817 mm. The volume fraction of the martensite phase in the SMA fibers is shown in Fig. 2.19, and Fig. 2.20 shows the debonding length of the SMA fibers in the bridging section. The fiber strain distribution is depicted in Fig. 2.21, and Fig. 2.22 gives the fiber stress distribution. The stress intensity factor is calculated by Eq. (2.19) and is equal to 57.45 N/mm$^{3/2}$.

Table 2.3. Input data for SMA hybrid composites.

σ_∞	σ_d	v_f	C	E_M
50 Mpa	150 Mpa	0.25	10 mm	3.3 Gpa
E_f	M_s	M_f	A_f	A_s
26.3 Gpa	18.4 °C	9.0 °C	34.5 °C	49.0 °C

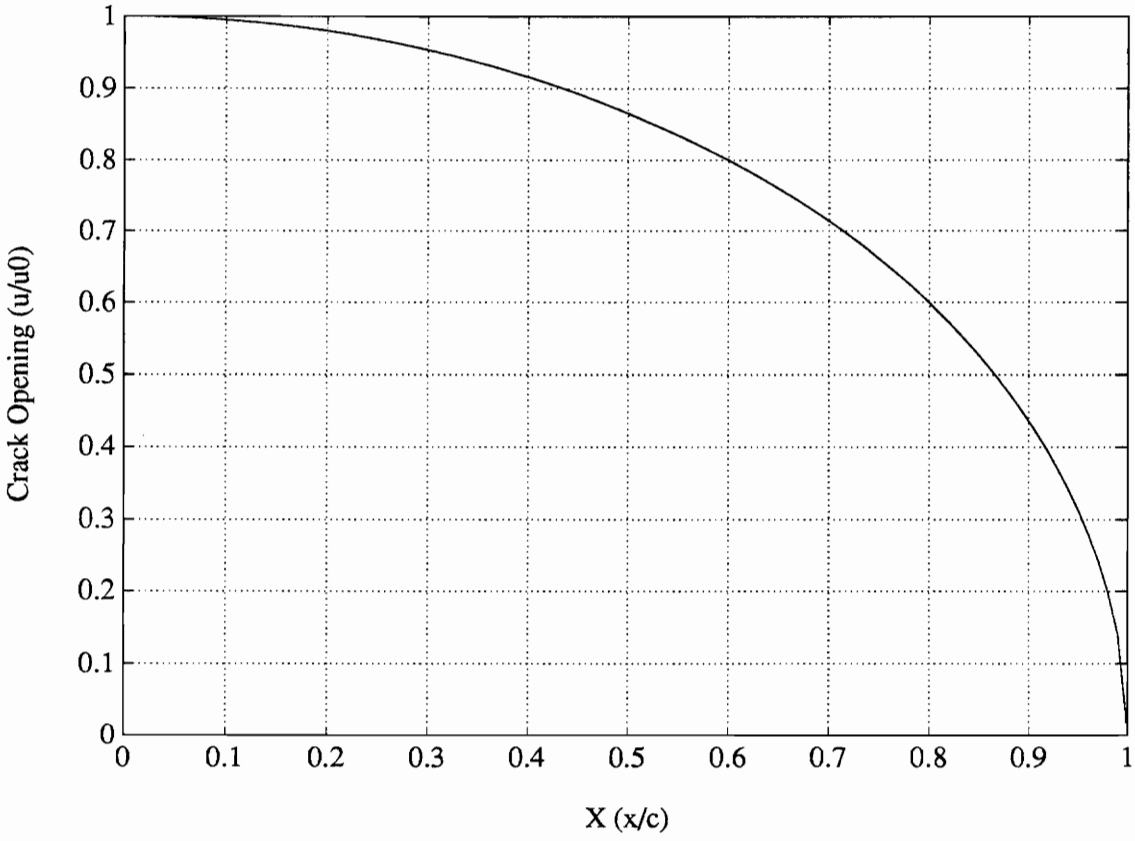

Figure 2.18: Crack opening displacement in inactivated tension.

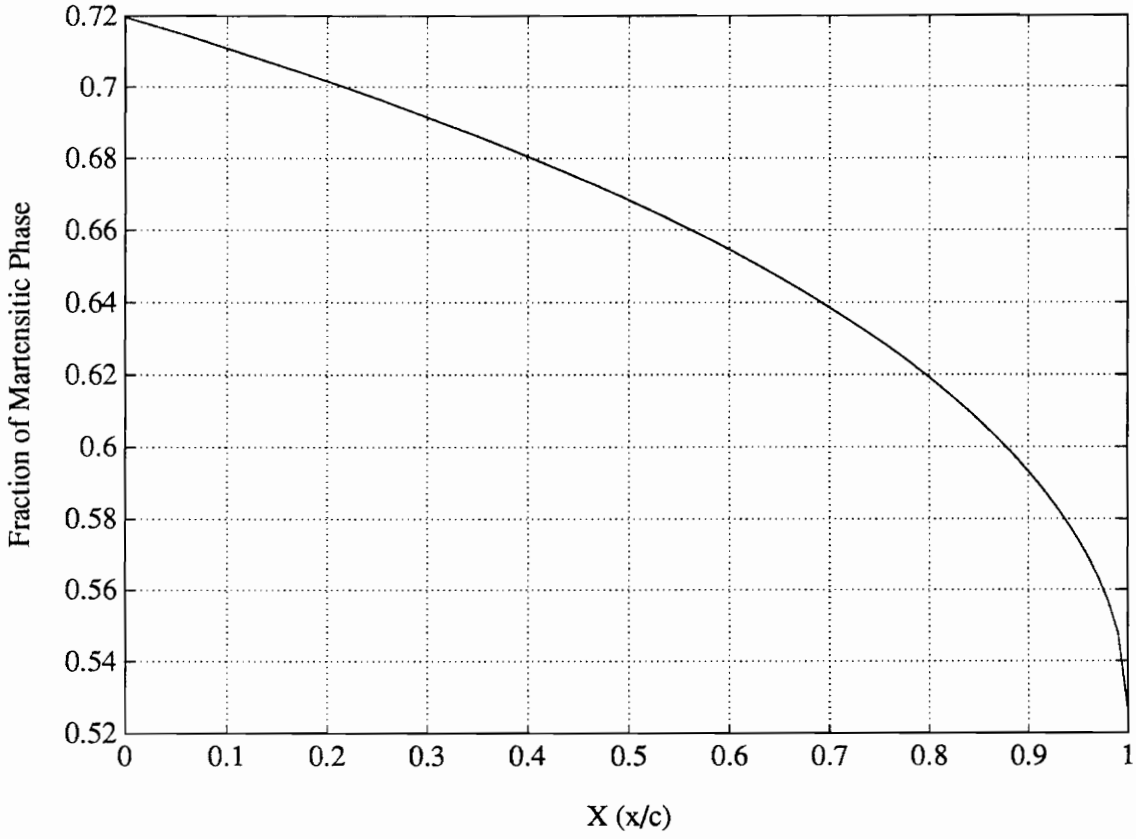

Figure 2.19: Volume fraction of martensitic phase in inactivated tension.

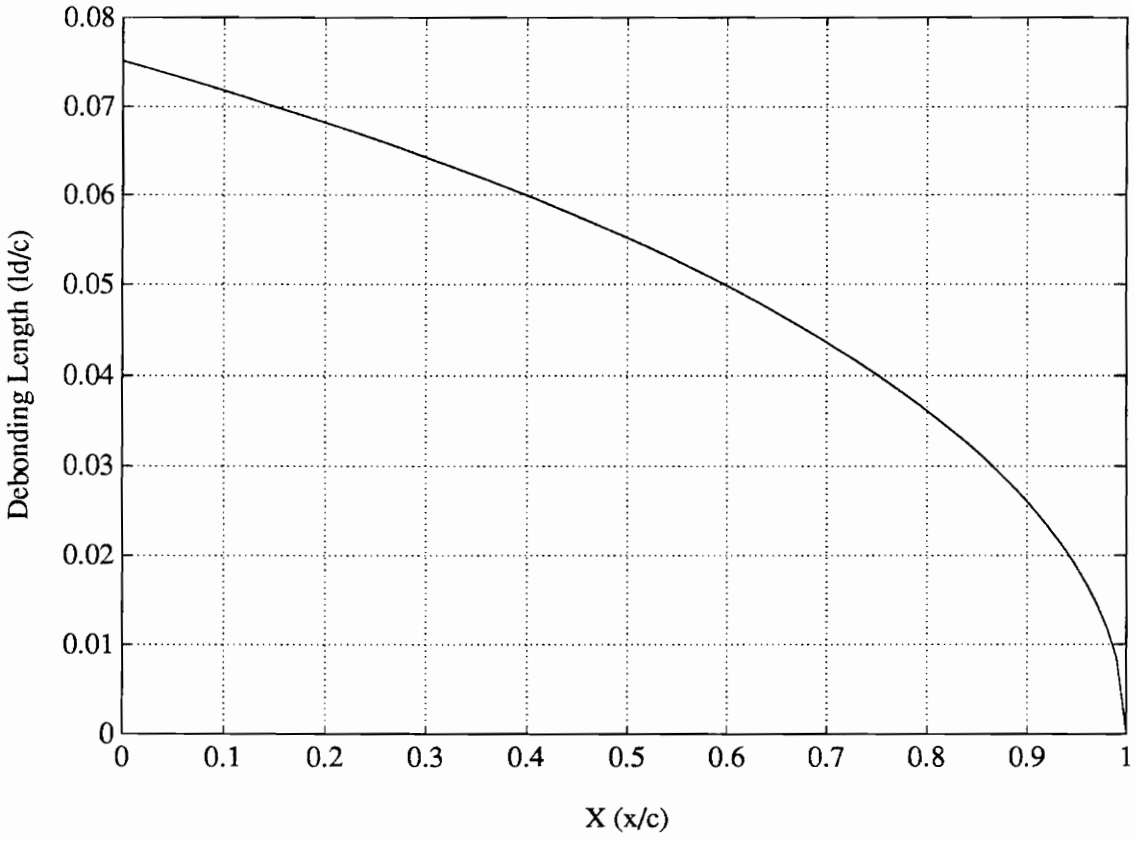

Figure 2.20: Distribution of debonding length of SMA bridging section.

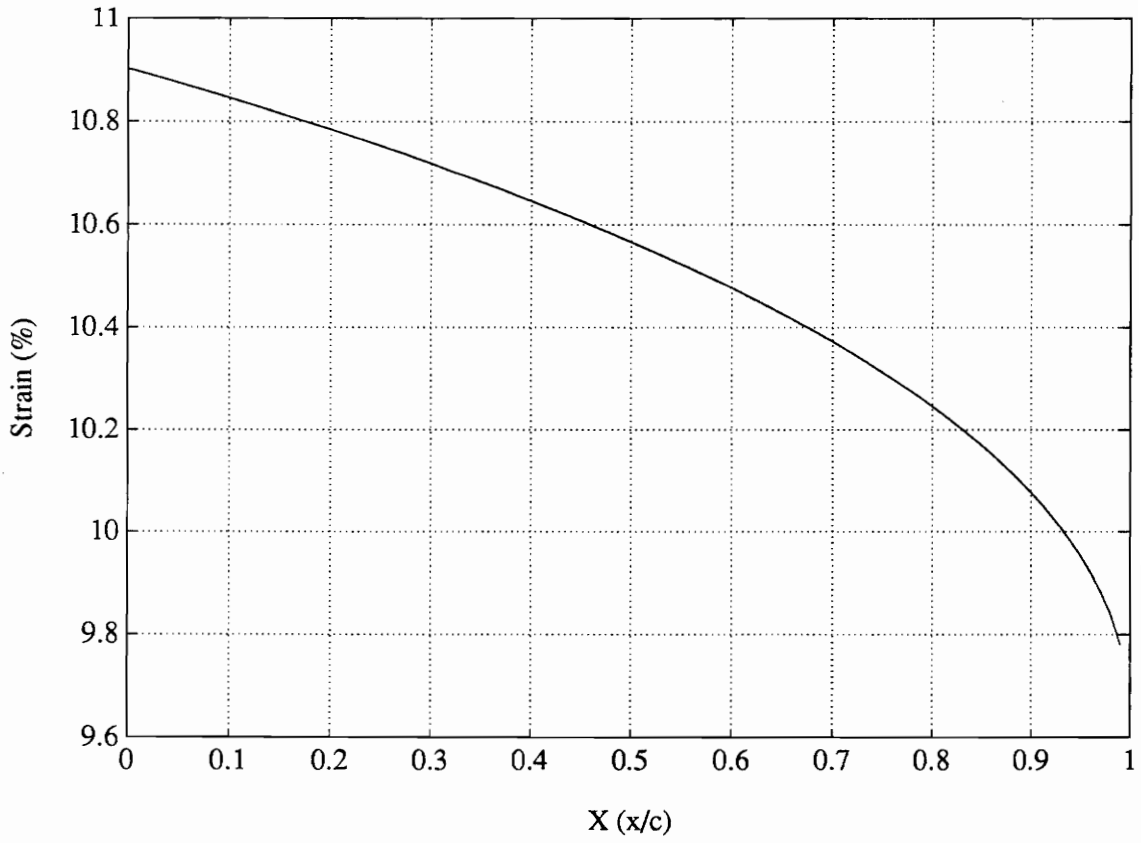

Figure 2.21: Fiber strain distribution in inactivated tension.

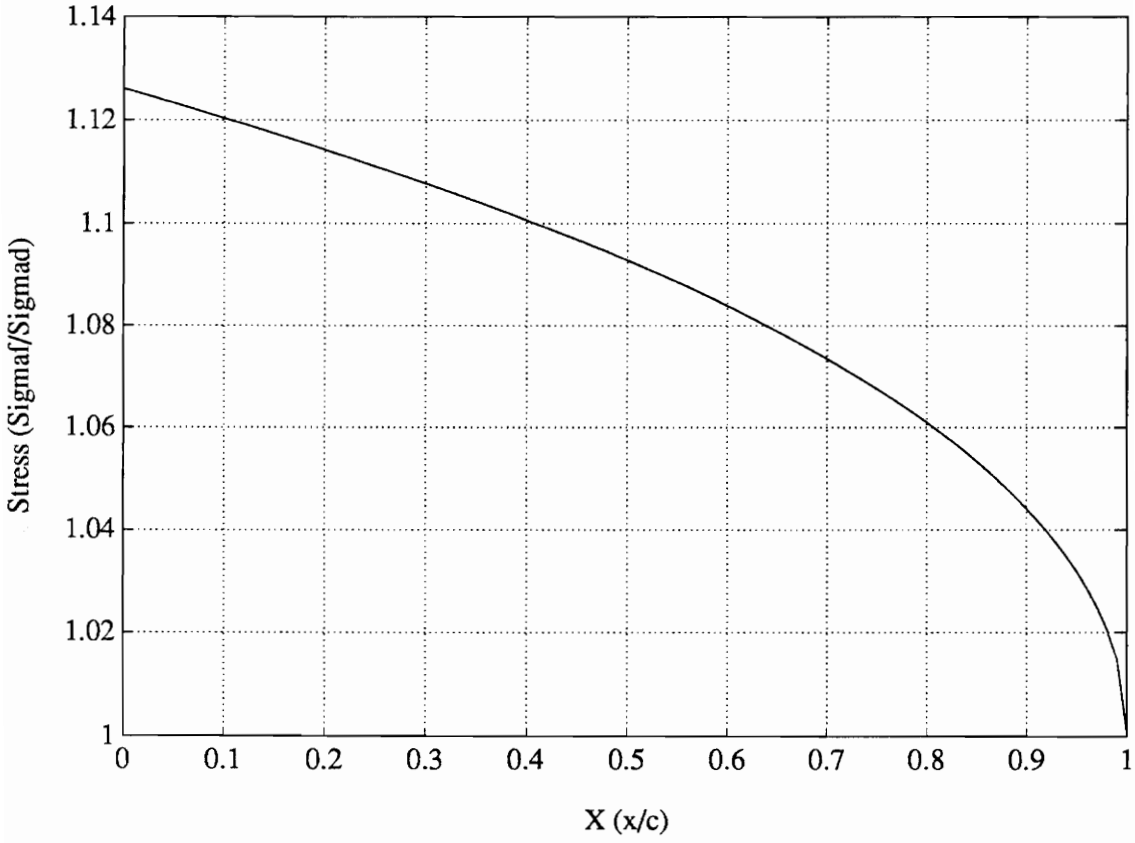

Figure 2.22: Fiber stress distribution in inactivated tension.

For the activated tension period, the fiber stress distribution is depicted in Fig. 2.23, while Fig. 2.24 shows the distribution of the volume fraction of the martensitic phase in SMA fibers. The crack opening displacement is plotted in Fig. 2.25, and Fig. 2.26 gives the strain distribution. The change in the stress intensity factor is calculated in Eq. (2.37), and equal to -29.1 $N/mm^{3/2}$.

In Figs. 2.23 - 2.26, dotted lines represent inactivated cases, and solid lines represent activated cases. In the plot of the volume fraction of the martensitic phase, Fig. 2.24, the solid line coincides with the x-axis, as all of the martensite in the bridging part has been transformed back to austenite after activation. After the activation of SMA actuators, the crack opening displacement at the back edge decreases by 23%, the fiber strain decreases by 23%, the fiber stress increases by 13%, and the stress intensity factor decreases by 50%.

In the present model, the minimum fiber stress in the bridging section of the SMA fibers is σ_d. Before the fiber stress, σ_f, arrives at σ_d, debonding between the fiber and matrix does not occur, and the crack surface cannot be opened. The bridging section experiences only elastic strain, which is the same as that in the surrounding matrix. After the fiber stress, σ_f, arrives at σ_d, the debonded length appears, and the crack opening displacement is generated between the two surfaces. However, the fiber strain in this bridging section may not be very small. Hence, the fiber strain around the crack

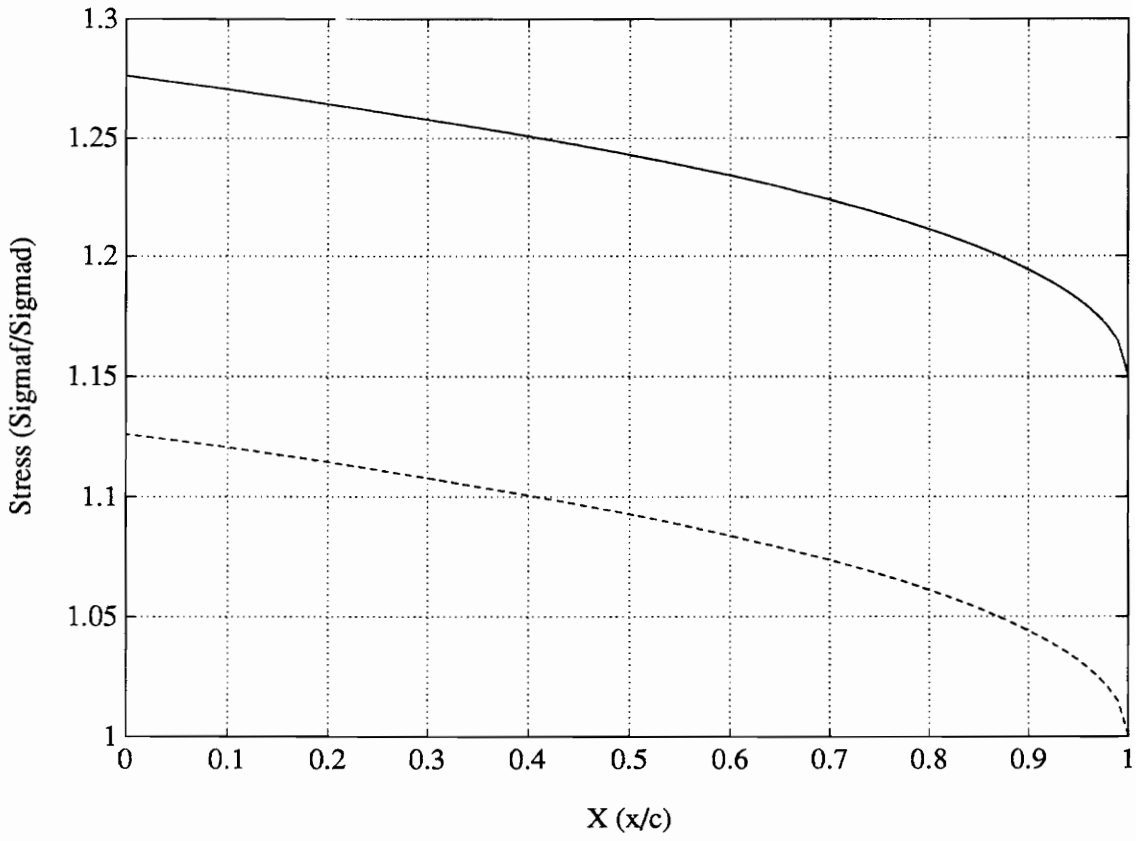

Figure 2.23: Fiber stress distribution in activated tension.

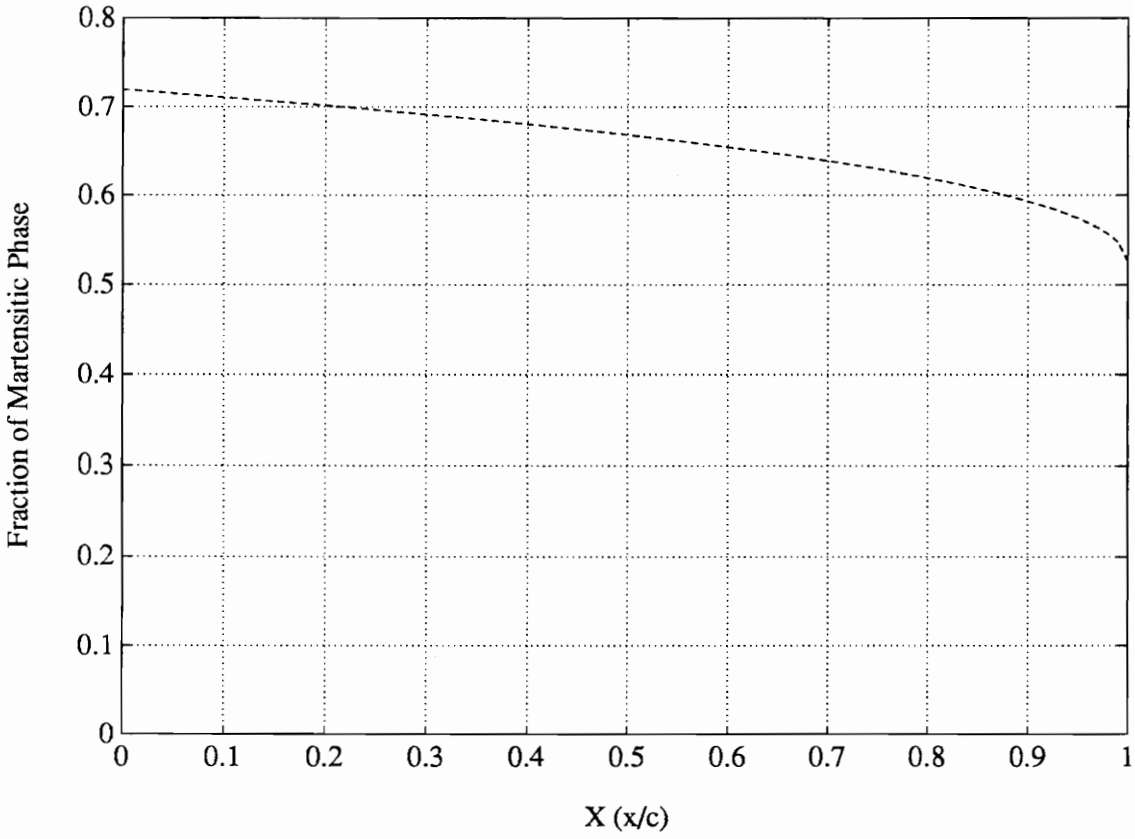

Figure 2.24: Volume fraction of martensitic phase in activated tension.

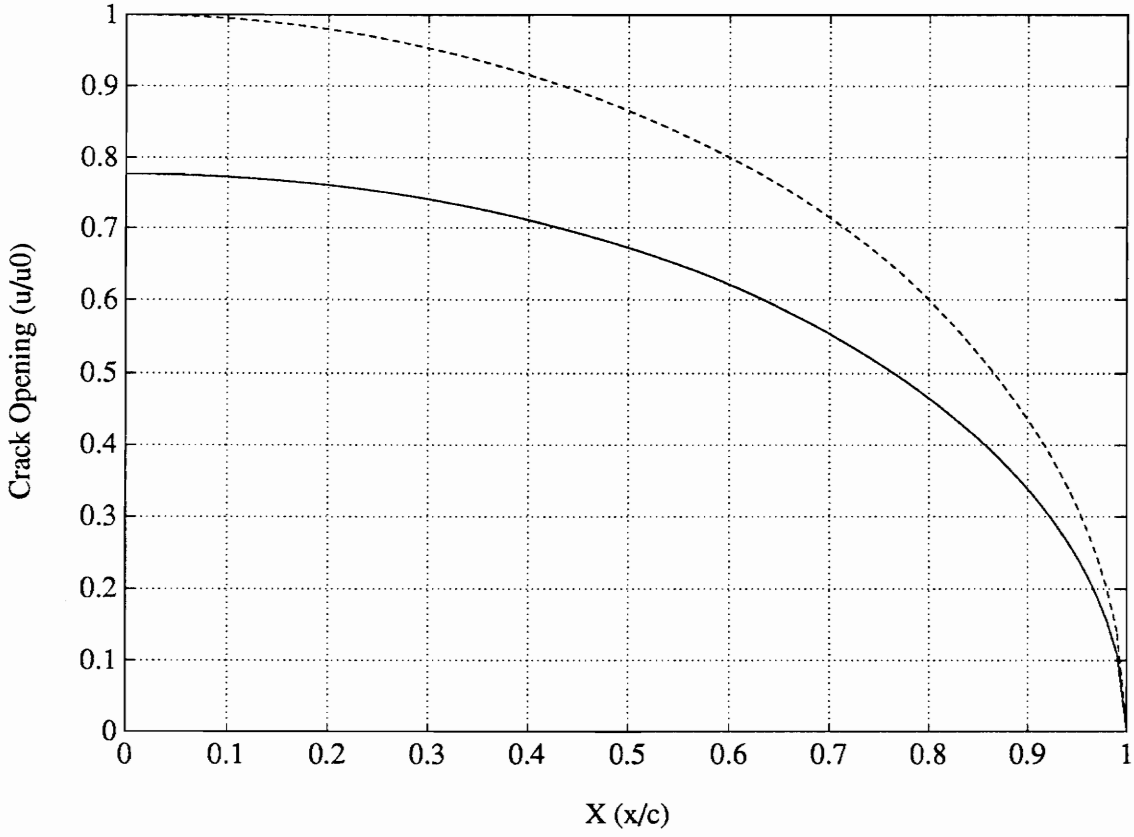

Figure 2.25: Crack opening displacement in activated tension.

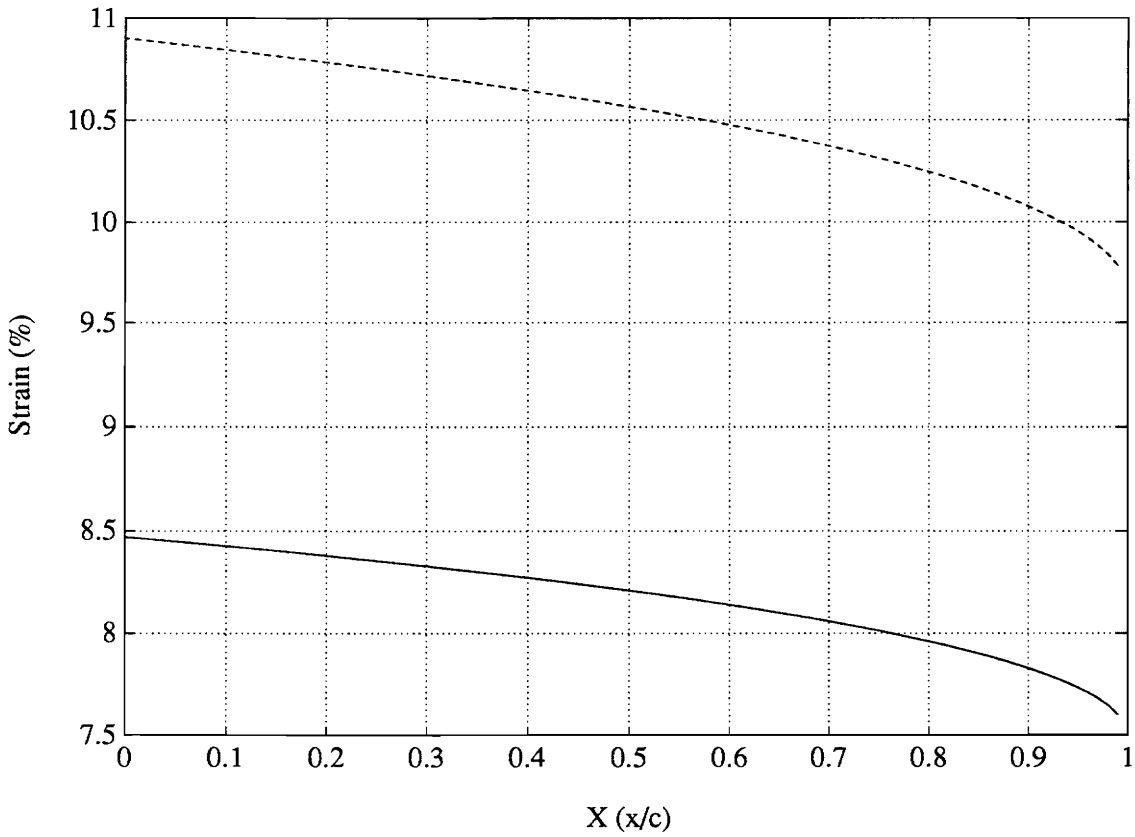

Figure 2.26: Fiber strain distribution in activated tension.

may not develop smoothly.

The thermal expansion difference between the fibers and the matrix in the activated period is not considered in the model. The importance of this parameter is related to the activation method used on the SMA actuators. If the heat is applied to the whole composite structure, this parameter will be of less importance; while, if it is applied only to the SMA actuators, e.g., by electric current, this parameter will be of more importance.

This theoretical analysis is only a preliminary model, or a simplified model, for active crack damage control in SMA hybrid composite systems. Experimental measurements are needed to verify the accuracy of this analytical prediction. On the other hand, this analytical model exhibits a new direction in active damage control. Active crack damage control in multiphase composite systems (e.g. SMA hybrid glass/epoxy composites) will be closer to real hybrid composite systems and more complicated, and should be the topic of future investigations.

2.5 Summary

1. Two scenarios of active crack damage control has been analyzed. In the first scenario, inelastically elongated SMA fibers are embedded into composites. Because of

the free edge effect, the activation is not effective away from the edges of the composites. For SMA fibers with short inelastically deformed sections in front of crack can be effective. However, in reality, the position of the section of the SMA fiber which is to be elongated is difficult to determine. In the second scenario, which is more practically applicable, virgin SMA fibers are embedded into composites. When the crack propagates and touches the fibers, the crack will pass through the fibers leaving the fibers intact, and the crack opening will transform the bridging parts of the fibers into the martensite phase. The activation of the bridging sections of SMA fibers will generate a recovery stress to be applied to the crack surfaces, resulting in a decrease in the stress intensity at the crack tip.

2. Photoelastic experiments have been conducted and showed the activation effects of SMA actuators on the crack tip. By using a partly prestrained SMA fiber in front of the crack tip, the stress intensity at the crack can be decreased by as much as 24% if the SMA fiber is activated. The results experimentally demonstrated the activation effects of SMA fibers on active crack damage control.

3. Finite element calculations have been conducted and compared with the photoelastic experiments. Good agreement has been obtained. In addition, the finite element analysis also showed that the stress level at the crack tip has decreased by 36% after the activation.

4. A theoretical model for the debonding length of SMA fibers has been developed. SMA pull-out tests have been conducted to verify the theoretical model. Good agreement with the experiment results has been obtained.

5. A theoretical model for SMA fibers bridging a crack has been developed. Expressions for crack opening displacement, martensitic phase fraction of SMA, fiber strain, fiber stress, and stress intensity factor have been obtained for pull-out tension and activation tension. The numerical example shows that after the activation of the bridging fibers, the stress intensity can be decreased by as much as 50%.

Chapter 3 Active Fatigue Damage Control of Adhesive Joints

Active fatigue damage control is a newly developing technique and is drawing more attention. Experiments and analysis related to this issue have been conducted, but the theoretical representation of the mechanics and mechanism of this subject has not yet been developed, and the physical meaning of active fatigue damage control is still not clear.

This chapter provides a fundamental analysis of the mechanism of active fatigue damage control, and a theoretical model for the active fatigue damage control of a cantilever beam. As an example, the adhesive joint of a cantilever beam is considered as the objective of active fatigue damage control.

3.1 Introduction to the Experiments of Active Fatigue Damage Control

The fatigue damage in an adhesive joint is directly related to the dynamic response. The dynamic loads for this beam are related to the beam's characteristics and the excitation frequencies. The active fatigue damage control is also realized through the dynamic

response.

The schematic diagram of the experimental set-up of active fatigue damage control is shown in Fig. 3.1. A graphite/epoxy beam is glued on a steel frame. The dimension of the beam is $185 \times 25.4 \times 1.5$ mm^3, and the site of the adhesive area is 38.1 mm in length and 25.4 mm in width. The material properties are listed in Table 3.1. Two G-1195 PZT actuators are bonded on the top and bottom surface at the beam root, respectively. A LDS V-203 shaker, which can generate maximum 3 lbf shaking force, is used to excite the beam at 1/4 of the beam length from the free end. A picture of the beam and the shaker is shown in Fig. 3.2.

The damage and control effects were examined by the following two experiments. In the first experiment, a sinusoidal signal was applied only to the shaker at the first resonance frequency. The displacement at the free end of the beam had the maximum value, and the amplitude was as high as 10 mm. After 52,000 cycles, the adhesive joint failed, and the graphite/epoxy beam was separated from the steel frame. In the second experiment, a sinusoidal signal was supplied to the shaker at the first resonance frequency of the beam. At the same time, the same signal is amplified and supplied to the PZT actuator to reduce the vibration of the beam. The electric field applied to the PZT actuators was 600 V/mm. With the PZT actuators being activated, the vibration amplitude at the free end of the beam was only 3 mm, which was less that 1/3 of the amplitude in the first

Table 3.1. Material properties of the beam, frame and PZT actuator.

$E_{G/E}$ (GPa)	$\rho_{G/E}$(kg/m^3)	$\sigma_{bG/E}$ (GPa)	E_{st} (GPa)	ρ_{st} (kg/m^3)
130	1500	1.5	210	7800
σ_{bst} (MPa)	E_{PZT} (GPa)	ρ_{PZT} (kg/m^3)	σ_{bPZT} (MPa)	d_{31}
482	63	7650	21 (Dynamic) 70 (Static)	180×10^{-12}

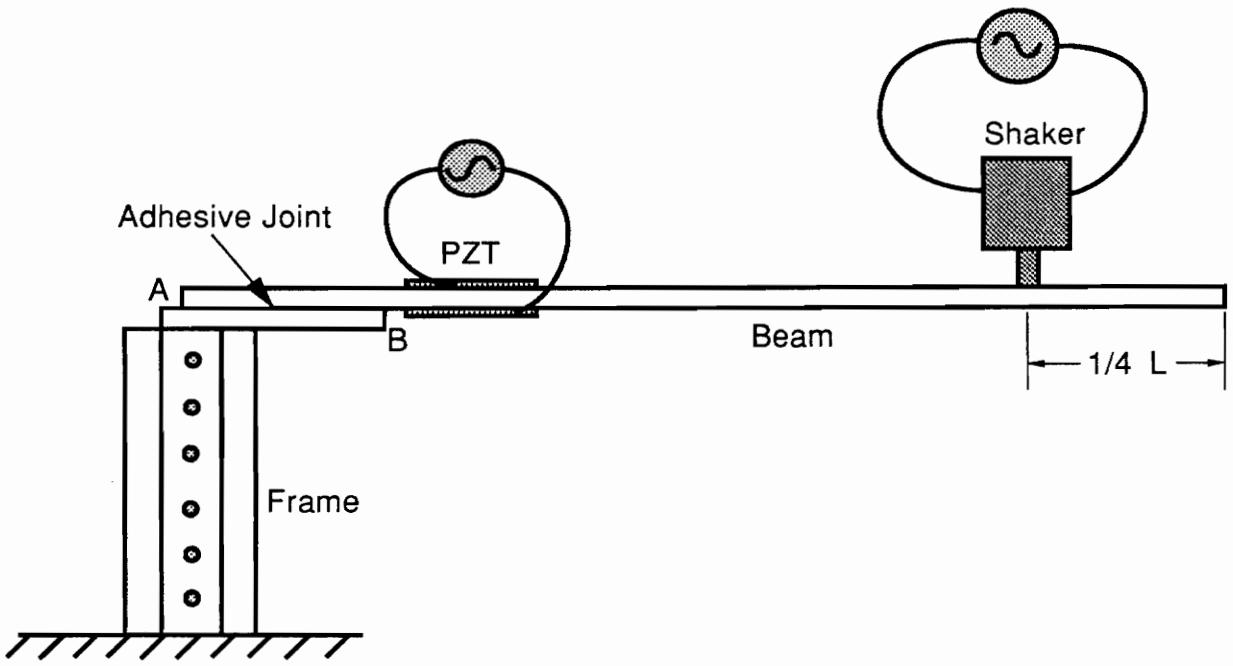

Figure 3.1: Schematic set-up of the experiments of active fatigue damage control.

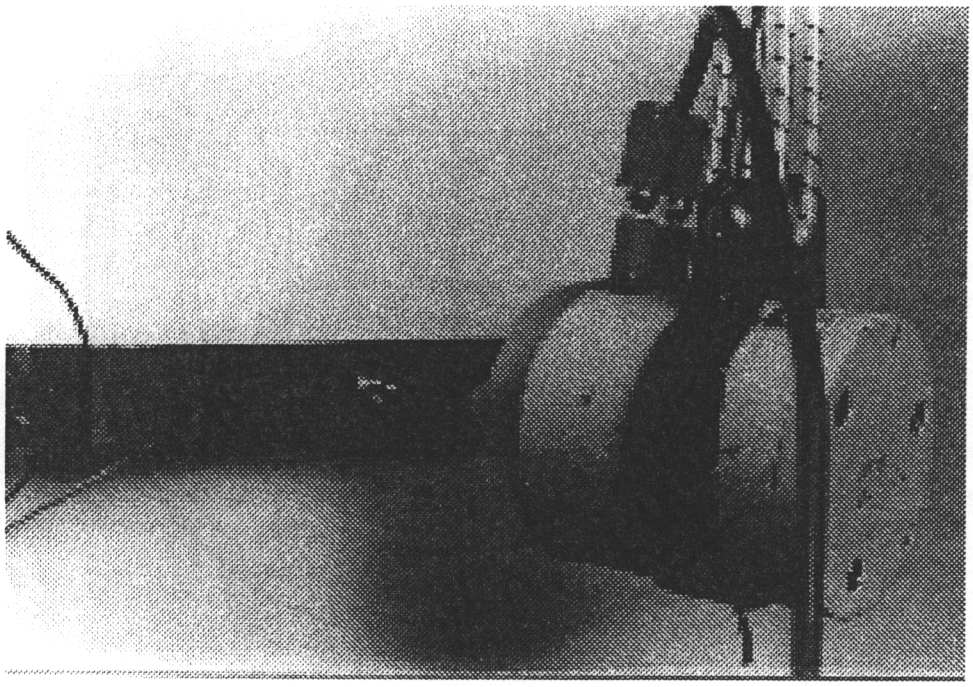

Figure 3.2: Shaker, beam and PZT actuator in the experimental set-up.

experiment. Under this dynamic load level, the adhesive joint failed after 500,000 cycles. The results of the above two experiments show a clear picture that the control of the beam's dynamic response can greatly increase the fatigue life of the adhesive joint.

In the failure process it was observed that the crack in the adhesive layer first initiated from point B, as shown in Fig. 3.1, and then propagated along the interface toward point A. According to the theory of fracture mechanics, cracks always initiate at highest stress and strain areas. Because of the discontinuity of the beam at the edge of the adhesive joint, stress and strain concentrations exist at the front and back edges, respectively. The finite element method is first used to calculate the stress and strain distributions in the adhesive joint.

3.2 Finite Element Analysis for the Stress Distribution in the Adhesive Joint

Finite element analysis was conducted to analyze the stress distribution in the adhesive joint. According to the theory of structural mechanics, it is known that the loading sources of the joint are the moment and the shear force generated by dynamic responses. Since the structure is a linear system, a unit moment and a unit shear force were used as the scaled-down external loads. The finite element mesh for the adhesive joint is shown in Fig. 3.3. To simplify the calculation, a 2-D, 8-node isoparameter element was used in the model. In Fig. 3.3, the top section represents the graphite/epoxy beam, and

the bottom section represents the steel frame. The clamped boundary condition is applied to the right side of the bottom section. Since the adhesive layer is much thinner than the beam and the frame, there is no element representing the adhesive layer in the model.

The stresses in the adhesive layer are given by the stresses on the interface nodes. For a unit moment loading (1 N-mm), the contour of σ_y is shown in Fig. 3.4, and the contour of σ_{xy} is given in Fig. 3.5. The normal stress distribution (σ_y) in the adhesive interface is depicted in Fig. 3.6. Figure 3.7 shows the shear stress distribution in the adhesive interface.

For a unit shear force loading (1 N), the contour of σ_y is shown in Fig. 3.8. The contour of σ_{xy} is shown in Fig. 3.9. The normal stress distribution (σ_y) in the adhesive interface is illustrated in Fig. 3.10. Figure 3.11 shows the shear stress distribution in the adhesive interface.

From Fig. 3.6 and Fig. 3.7, it can be seen that the stress level at the front edge is twice as much as the stress level at the back edge. From Fig. 3.10 and Fig. 3.11, it can be found that the normal stress at the back edge is three times as high as that at the front edge, and the shear stress is five time more than that at front edge. The total stress level is the summation of each stress level generated by moment and shear force. The actual

stress levels at the front edge and the back edge can only be determined after the analysis of the dynamics of the beam, from which the dynamic moment and shear force can be calculated.

Since the PZT actuators were mounted very close to the adhesive joint, the stress calculated by the activation of the PZT actuators might also affect the stress distribution in the adhesive joint. To examine this effect, another finite element analysis was conducted, and the finite element mesh is shown in Fig. 3.12. The distance between the actuators and the steel frame is 1 mm. The activation of the top actuator causes contraction, while the activation of the bottom actuator creates expansion. The schematic deformation of the beam after the activation of PZT actuators is shown in Fig. 3.13. Figure 3.14 shows the contour of the Von-Mises stress distribution after the PZT activation. The conclusion drawn from Fig. 3.14 is that the stress field resulting from the activation of the actuators has no direct effect on the stress distribution in the adhesive joint.

3.3 Mechanism of Active Fatigue Damage Control

The active fatigue damage control of a specific area is accomplished through the fatigue stress level control in that area, since the fatigue damage initiation and propagation are closely related to the fatigue stress level. In this thesis, the fatigue stress level control

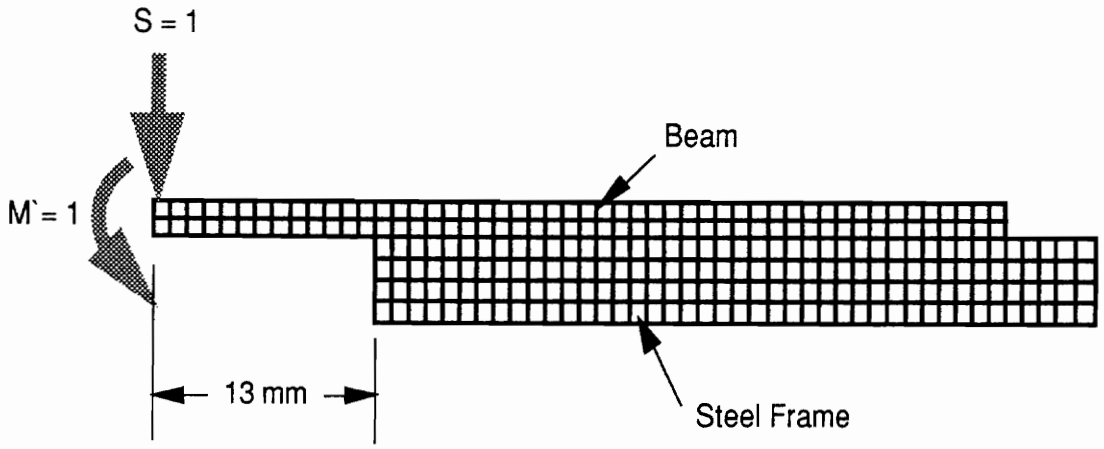

Figure 3.3: Finite element mesh for the adhesive joint.

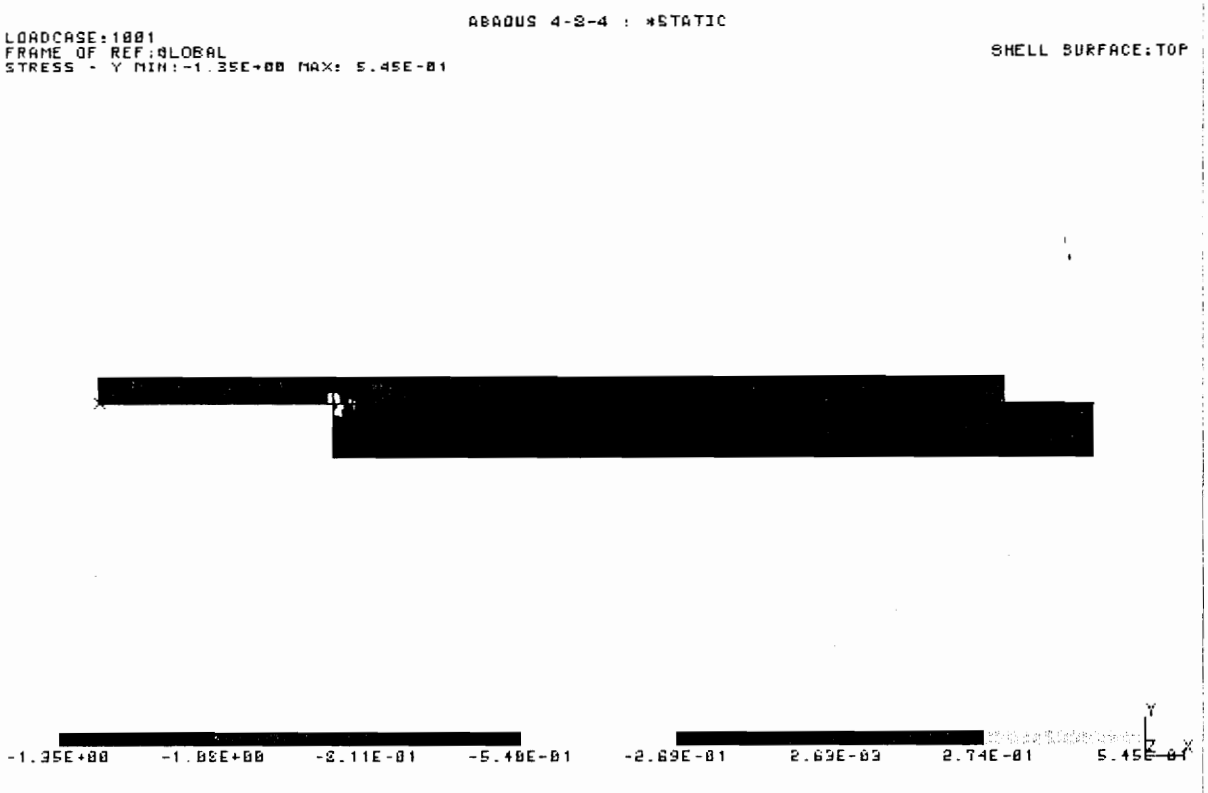

Figure 3.4: Contour of σ_y for unit moment loading.

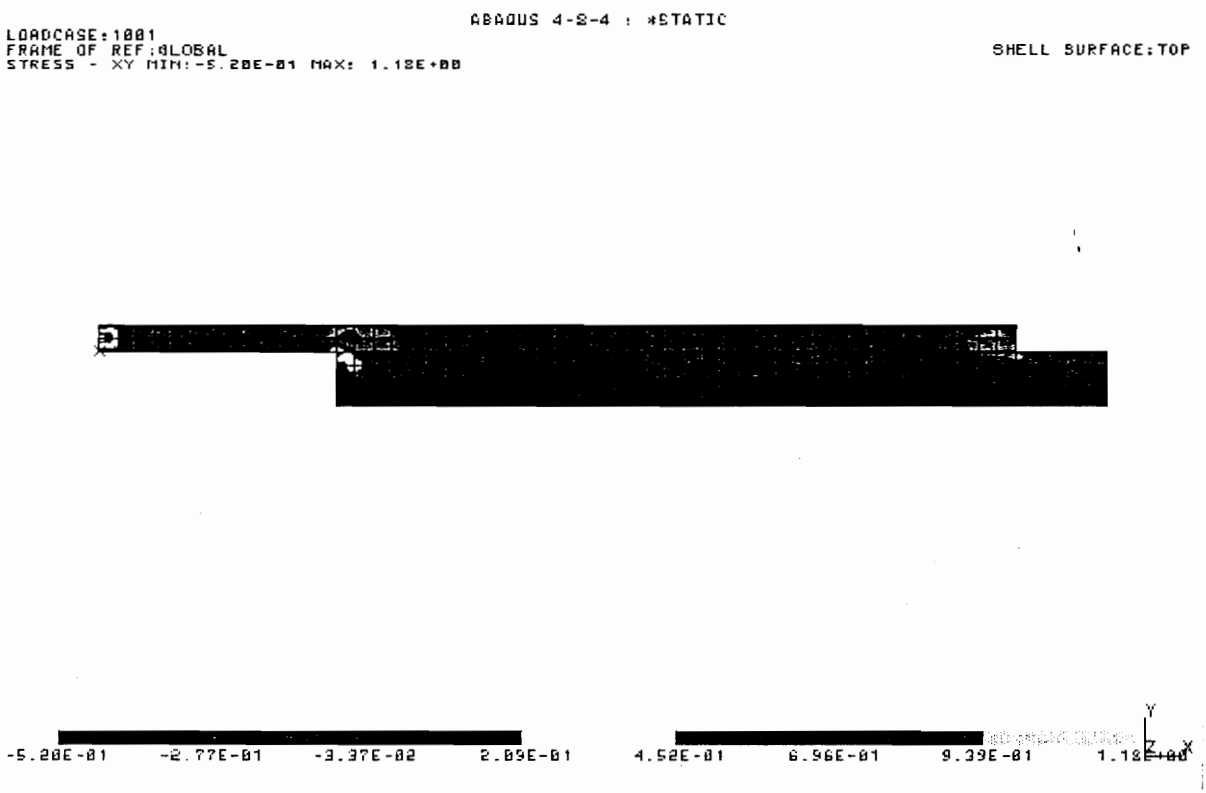

Figure 3.5: Contour of σ_{xy} for unit moment loading.

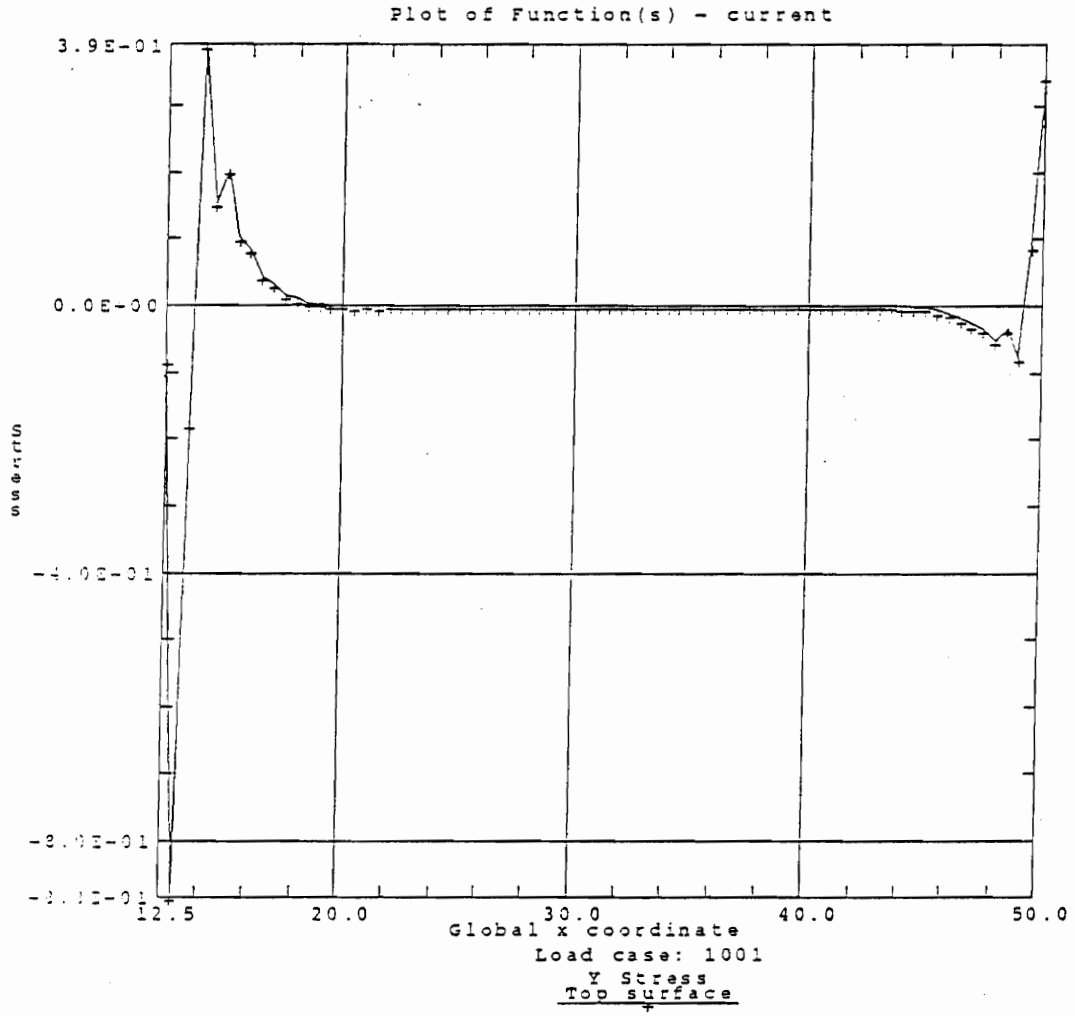

Figure 3.6: Normal stress distribution (σ_y) in the adhesive interface for unit moment loading.

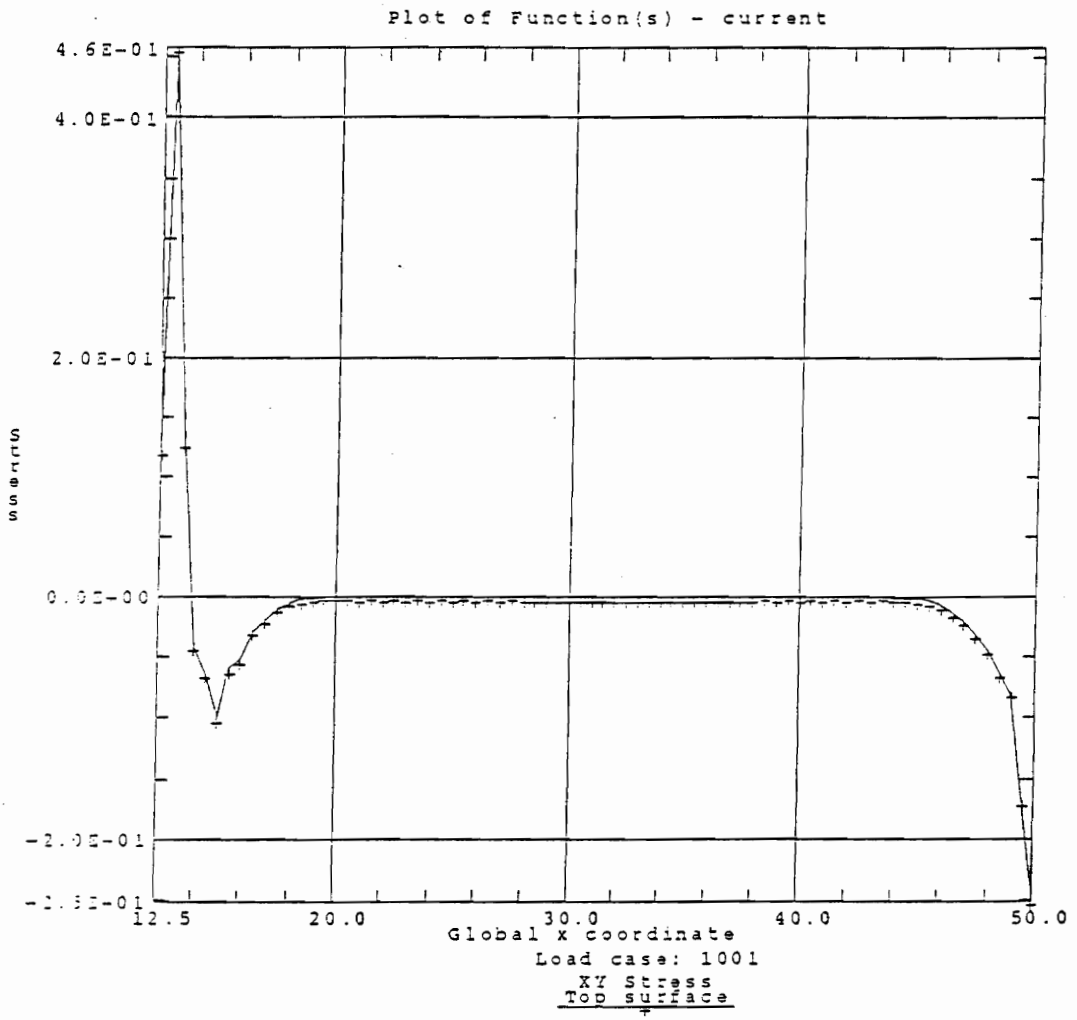

Figure 3.7: Shear stress distribution in the adhesive interface for unit moment loading.

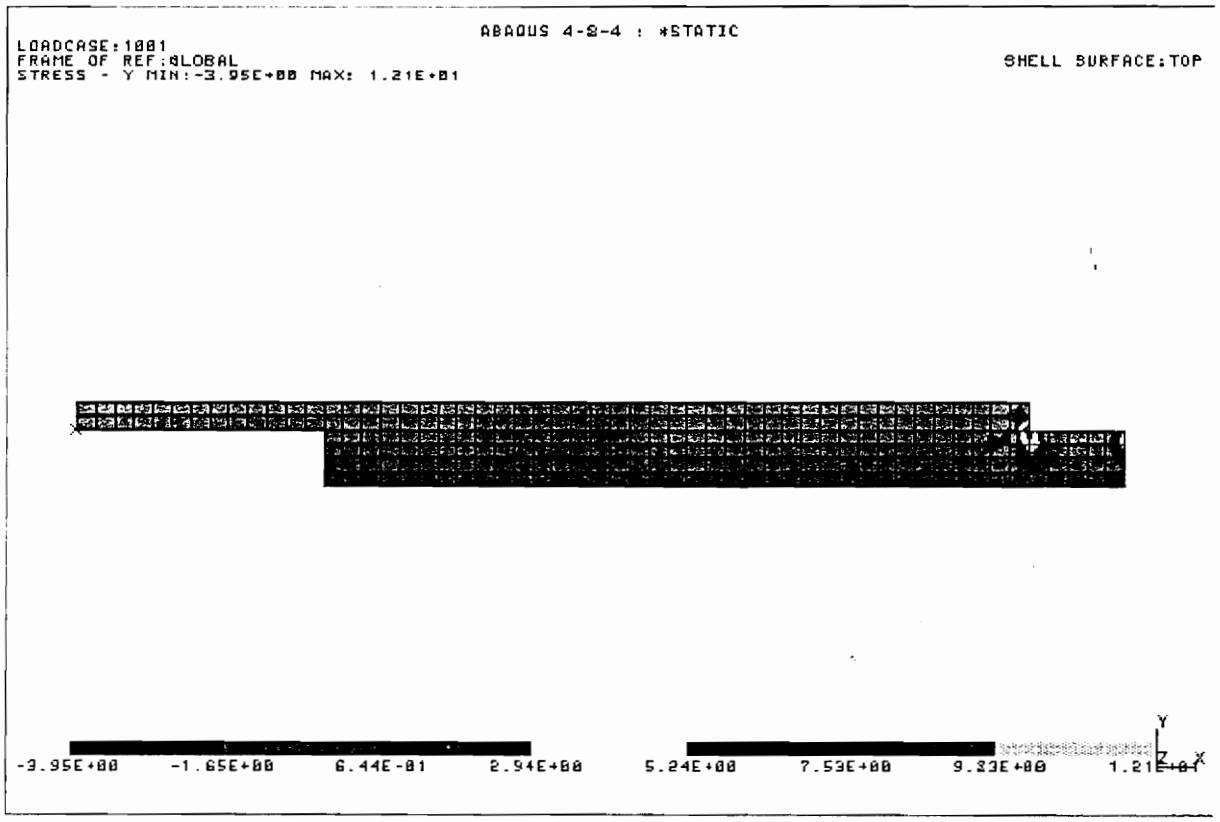

Figure 3.8: Contour of σ_y for unit shear force loading.

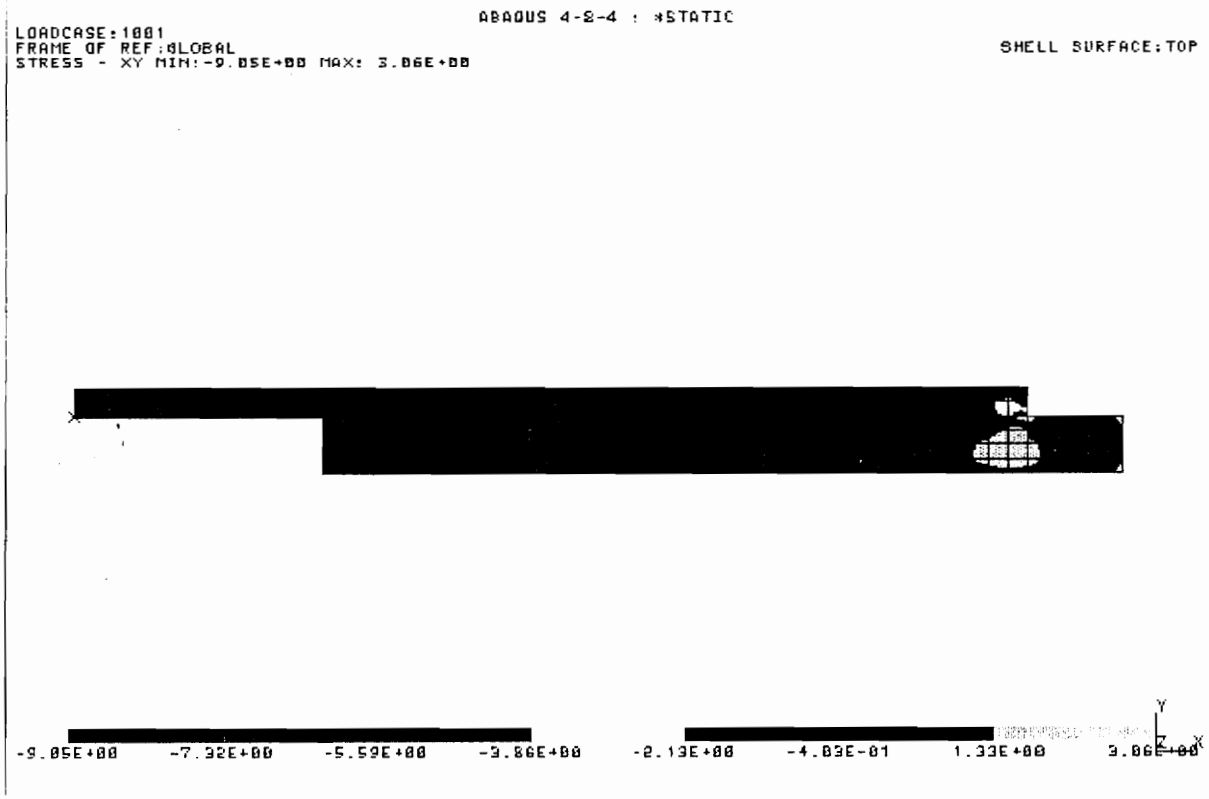

Figure 3.9: Contour of σ_{xy} for unit shear force loading.

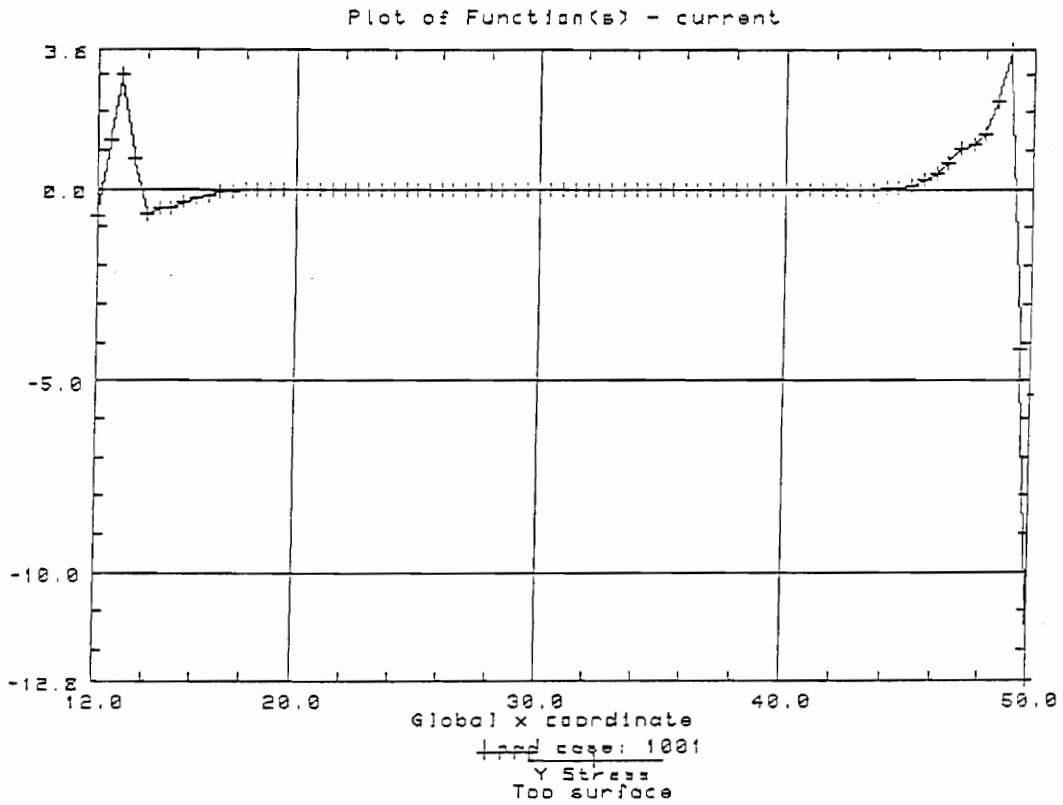

Figure 3.10: Normal stress distribution (σ_y) in the adhesive interface for unit shear force loading.

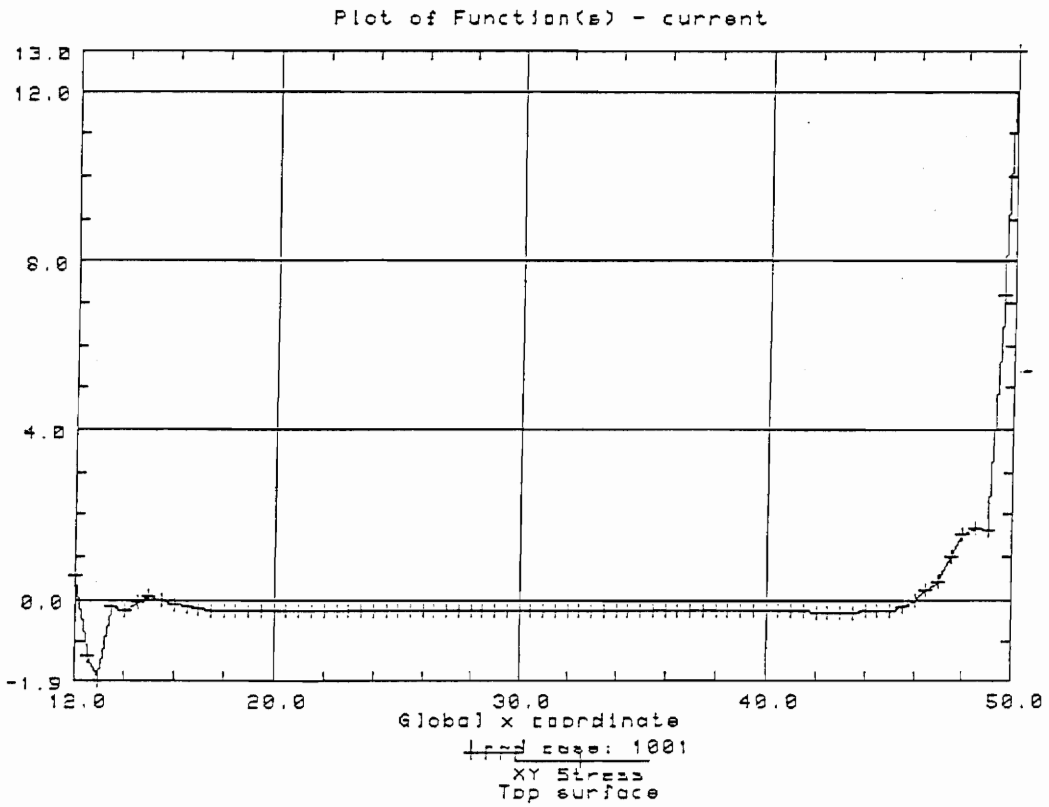

Figure 3.11: Shear stress distribution in the adhesive interface for unit shear force loading.

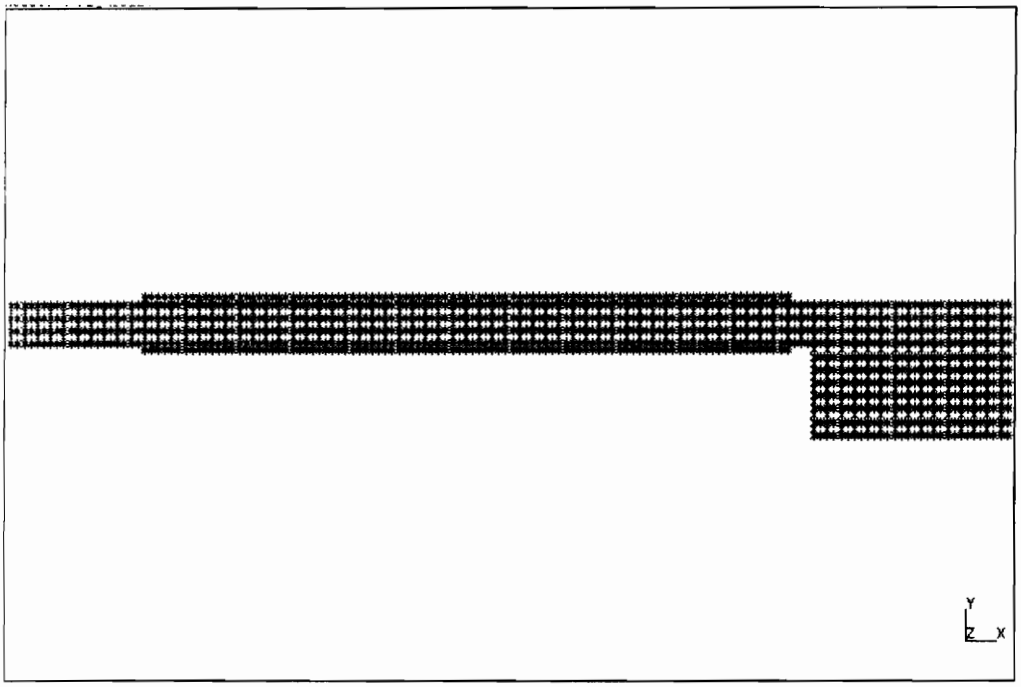

Figure 3.12: Finite element mesh for the static activation of PZT actuators.

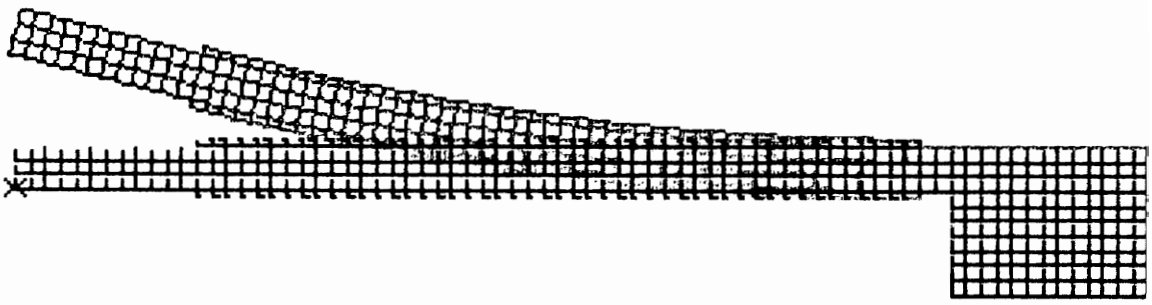

Figure 3.13: Schematic deformation of the structure after the activation of PZT actuators.

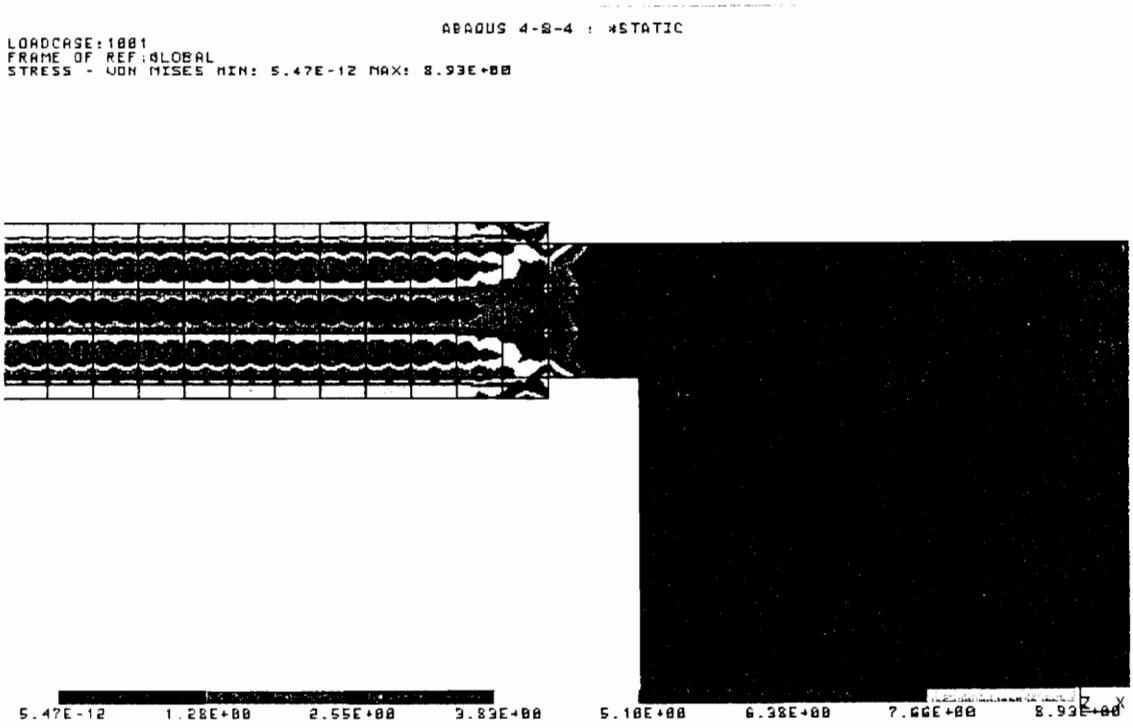

Figure 3.14: Contour of the Von Mises stress distribution after the static activation of PZT actuators.

is realized by means of fatigue stress cancellation. The active fatigue stress cancellation can be classified into two categories - direct stress cancellation and indirect stress cancellation. These two techniques will be explained in next two subsections.

3.3.1 Direct Stress Cancellation (DSC)

The technique of direct stress cancellation uses the direct superposition of two out-of-phase stress spectrums to decrease the local stress level at a specific area. A schematic diagram of direct stress cancellation is shown in Fig. 3.15 (Rogers et al., 1991). An induced strain actuator is placed at the high stress and strain area (a hole in Fig. 3.15). The activation of the induced strain actuator will generate induced strain and stress in the structure underneath the actuator. This induced strain and stress can be directly used to change the original stress and strain distribution in the structure by superposition. Proper activation of the actuator will locally reduce the stress and strain concentration level in that area, resulting in a reduction of the level of damage.

In the technique of direct stress cancellation, the control effect depends on the level of the activation stress generated in the structure. The activation stress is related to the relative stiffness of the structure and the actuator and the maximum activation strain of the actuator. Sometimes, these conditions limit the application of this configuration.

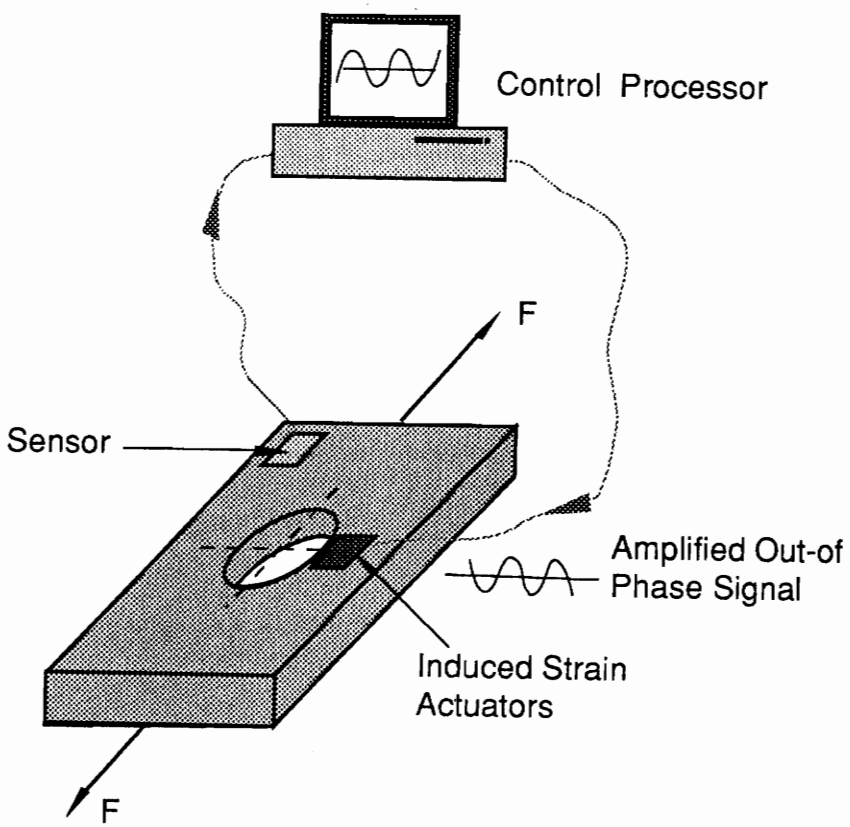

Figure 3.15: Schematic diagram of local fatigue damage control.

In addition, the location of the actuator is also important. The closer to the damage area the actuator is placed, the better the reduction effect is. Sometimes, space is critical for an induced strain actuator, although the induced strain actuators can be fabricated in small sizes.

The technique of direct stress cancellation will not be investigated for active fatigue control in this thesis. Instead, attention will be given to the indirect stress cancellation technique.

3.3.2 Indirect Stress Cancellation (ISC)

The technique of indirect stress cancellation uses the superposition of two out-of-phase dynamic responses to decrease the local stress level at a specific area. A schematic diagram of active fatigue damage control of adhesive joint with ISC is shown in Fig. 3.16. A cantilever beam is subjected to an excitation force and vibrates. The inertial force of the vibrating beam will generate a moment and a shear force at the root of the beam. From the Newton's law, $F=ma$, the inertial force is proportional to the mass and the acceleration of the mass. For a harmonic vibration, the acceleration can be expressed as $\ddot{Y}=Y\omega^2$, where Y is the amplitude of vibration, and ω is the vibration frequency. The inertial force can result in much higher debonding moment and shear force than that resulting from the excitation force at the free end of the beam, which can be seen in later

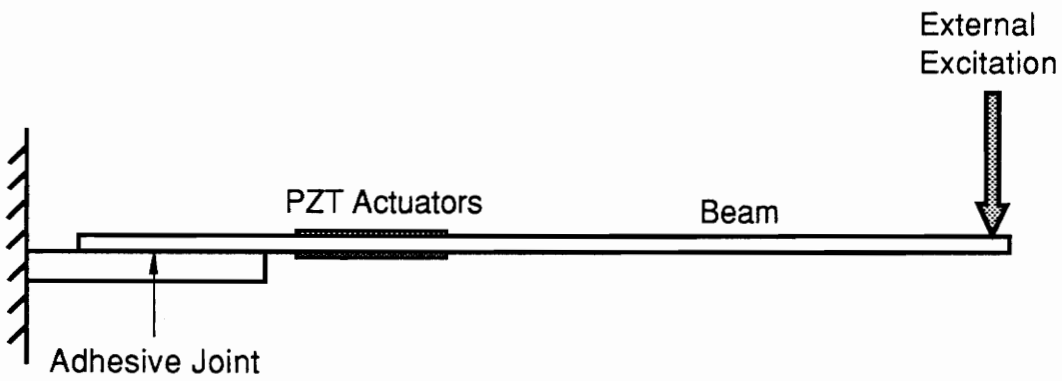

Figure 3.16: Schematic diagram of active fatigue damage control of adhesive bonding joint with ISC.

numerical result, shown in Fig. 3.21. The solid line is the dynamic moment due to the inertia force, while the dashed line is the moment created by the force at the free end of the beam. In Fig. 3.16, two PZT actuators are mounted on the top and bottom surfaces. The activation of these two actuators with out-of-phase signals can generate a pure bending moment.

Activation of these two actuators will not directly alter the stress in the bonding joint, but the reduction of vibration of the beam will reduce the dynamic moment due to the external excitation. This indirect approach of reducing the fatigue loading using the induced strain actuators is referred to as indirect stress cancellation.

3.4 Determination of the Dynamic Moment and Shear Force

The dynamic moment and shear force can be analyzed by the theory of vibration system. Since the beam system is assumed to be a linear system, the superposition is valid in this system. The control effects can be determined by the superposition of two dynamic responses - the response of external excitation and the response of actuators. Both dynamic responses can be analyzed with the Bernoulli-Euler beam theory:

$$\frac{\partial v}{\partial x} = -\theta \tag{3.1a}$$

$$(1+c^* \frac{\partial}{\partial t})\frac{\partial \theta}{\partial x} = \frac{M}{EI} \tag{3.1b}$$

$$\frac{\partial M}{\partial x} = V - c(x,t) \tag{3.1c}$$

$$\frac{\partial V}{\partial x} = -w(x,t) + c'\frac{\partial v}{\partial t} \ , \tag{3.1d}$$

where v is the lateral deflection, θ is the rotary angle of the deflection curve, M is the bending moment at any section, V is the shear force at any section, E is the modulus of elasticity of the material, I is the moment of inertia taken about the neutral axis, c is the moment intensity, c′ is the viscus damping coefficient, and c^* is the structural damping parameter.

Under forced harmonic motion, the state variables v, θ, M and V vary as $\sin\omega t$ or $\cos\omega t$. The time-dependent state variables resulting from arbitrary dynamic loading are given by (Pilkey and Chang, 1978):

$$v(x,t) = \sum_n A_n(t) v_n(x) \tag{3.2a}$$

$$\theta(x,t) = \sum_n A_n(t) \theta_n(x) \tag{3.2b}$$

$$M(x,t) = \sum_n A_n(t) M_n(x) \tag{3.2c}$$

$$V(x,t) = \sum_n A_n(t) V_n(x) \ , \tag{3.2d}$$

where v_n, θ_n, M_n and V_n are normal modes of the structure. A_n is the generalized coordinates and is expressed by:

$$A_n(t) = \frac{\eta_n(t)}{N_n} \quad . \tag{3.3}$$

By assuming that the damping is proportional, the quantities in the equation are defined as:

$$N_n = \int_0^L \rho v_n^2 dx \tag{3.4}$$

$$\eta_n(t) = e^{-\zeta_n\omega_n t}\left[\cos\alpha_n t + \frac{\zeta_n\omega_n}{\alpha_n}\sin\alpha_n t\right]\eta_n(0) + e^{-\zeta_n\omega_n t}\frac{\sin\alpha_n t}{\alpha_n}\frac{\partial\eta_n(0)}{\partial t} + \int_0^t f_n(\tau)e^{-\zeta_n\omega_n(t-\tau)}\frac{\sin\alpha_n(t-\tau)}{\alpha_n}d\tau \quad , \tag{3.5}$$

where $\alpha_n = \omega_n(1-\zeta_n^2)^{1/2}$, $\zeta_n = (c_\rho/\omega_n + \omega_n c^*)/2$. If $\zeta > 1$, sin should be replaced by sinh, cos by cosh, and $(1-\zeta_n^2)^{1/2}$ by $(\zeta_n^2-1)^{1/2}$. L is the length of the beam. For zero viscus and structural damping, $\zeta_n = 0$.

$$\eta_n(0) = \int_0^L \rho v(x,0) v_n \, dx \tag{3.6}$$

$$f_n(t) = \int_0^L [w(x,t)v_n + c(x,t)\theta_n] \, dx \quad , \tag{3.7}$$

where w(x,t) is the distributed load, and c(x,t) is the distributed moment. For the cantilever beam, the mode shape is given by:

$$v_n(x) = \cosh\frac{\lambda_n x}{L} + \cos\frac{\lambda_n x}{L} - \sigma_n\left(\sinh\frac{\lambda_n x}{L} - \sin\frac{\lambda_n x}{L}\right) \quad , \tag{3.8}$$

where λ_n and σ_n are parameters which are listed in the reference (Young and Felgar,

1949).

With the relations of Eq. 3.2, the response of external excitation and the actuator response can be calculated separately. The complete control response can be obtained by the superposition of the responses of the external excitation and the activation of the actuators.

3.4.1 Results of External Excitation

For the dynamic response analysis, the system is simplified as a cantilever beam, shown in Fig. 3.17. BEAM VI (Mitchell, 1992), which follows the approach outlined in Eqs. (3.1a) to (3.8), is used to calculate the moment and shear force acting on the bonding joint. The displacement distribution at the first resonance frequency (36.3 Hz) along the beam is calculated and shown in Fig. 3.18. Figure 3.19 shows the moment distribution along the beam. The shear force distribution is plotted in Fig. 3.20. The magnitude of the excitation force is 0.5 N.

Since the beam is a linear system, the above results can be used as reference values. The real dynamic responses can be determined by multiplying these reference values by a magnifying parameter. From Fig. 3.18, the maximum displacement at the free end at the first resonant frequency is about 20 mm, which is twice as many as the value of the

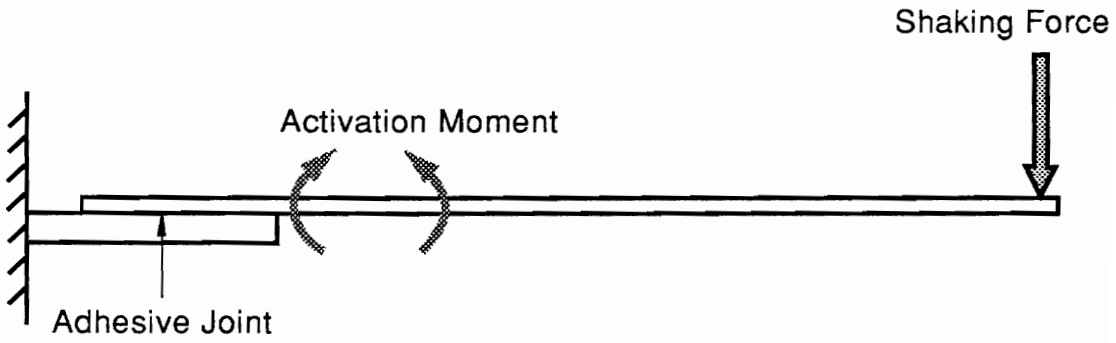

Figure 3.17: Simplified system of the cantilever beam.

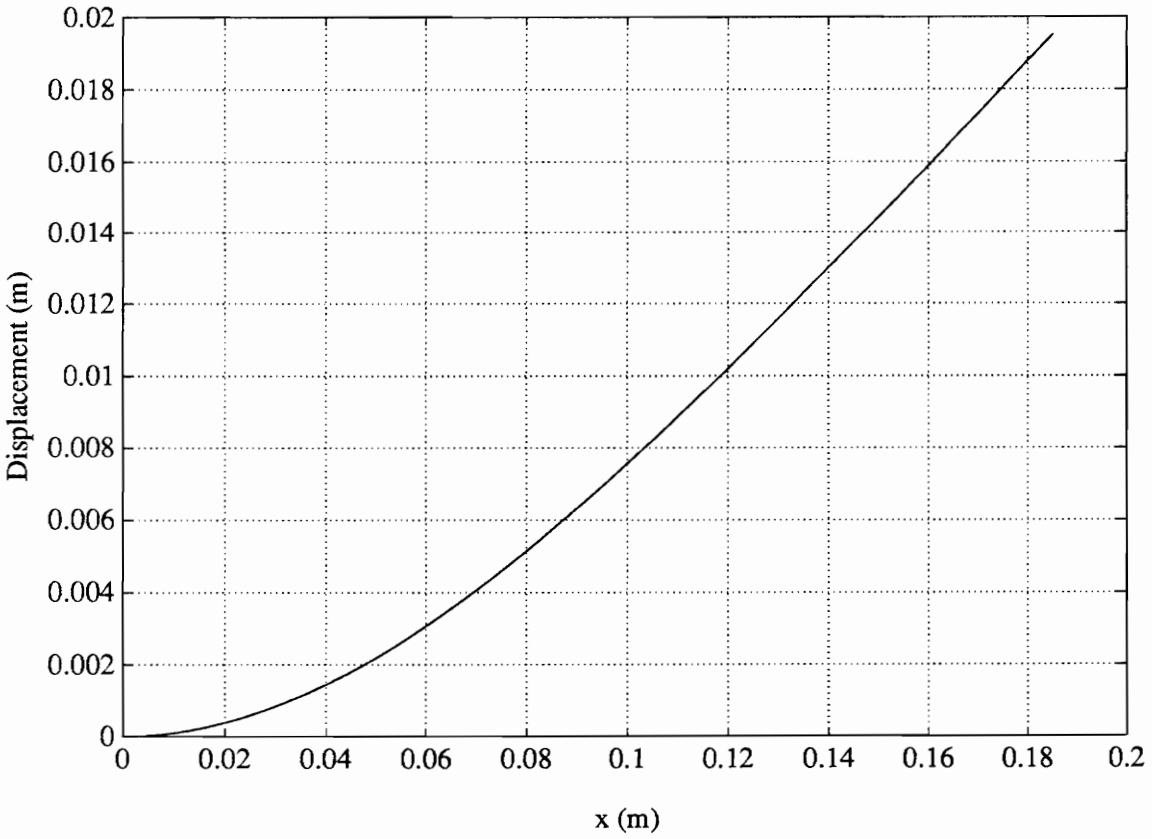

Figure 3.18: Displacement distribution along the beam due to a constant force excitation.

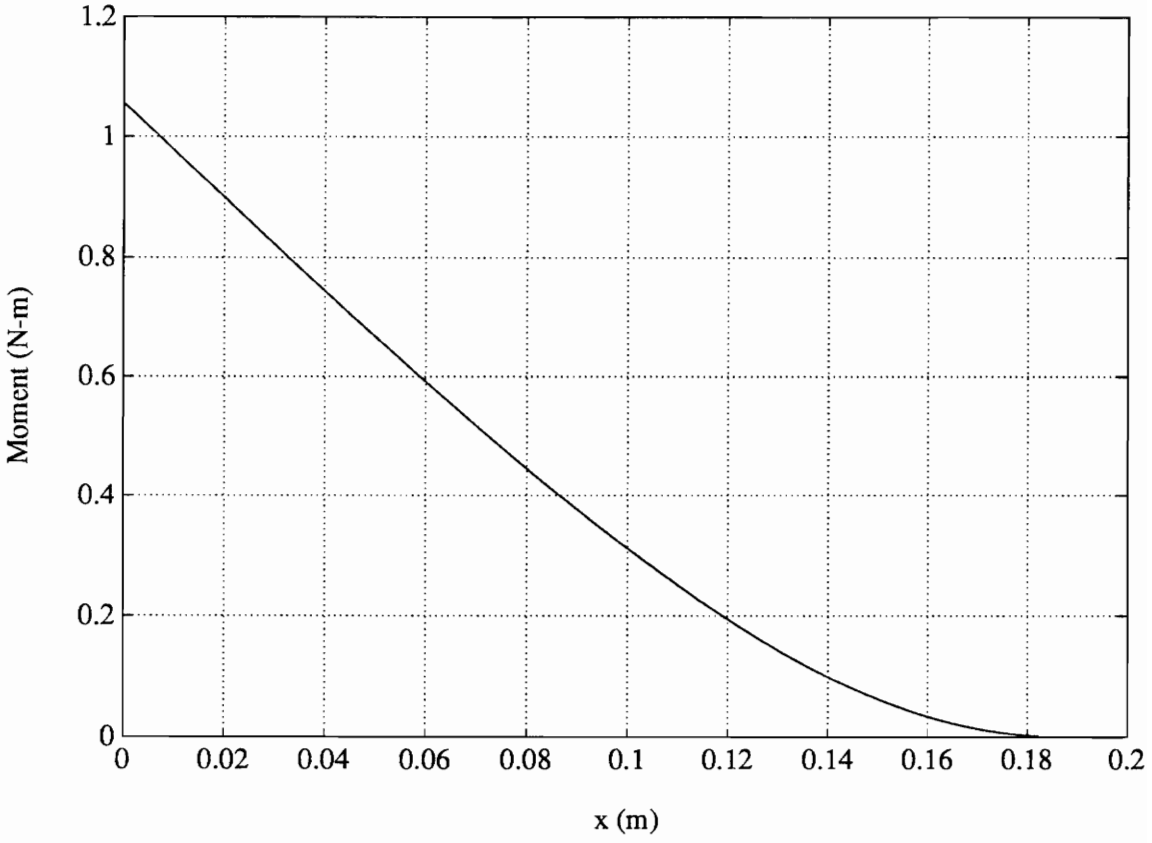

Figure 3.19: Moment distribution along the beam with the constant force excitation.

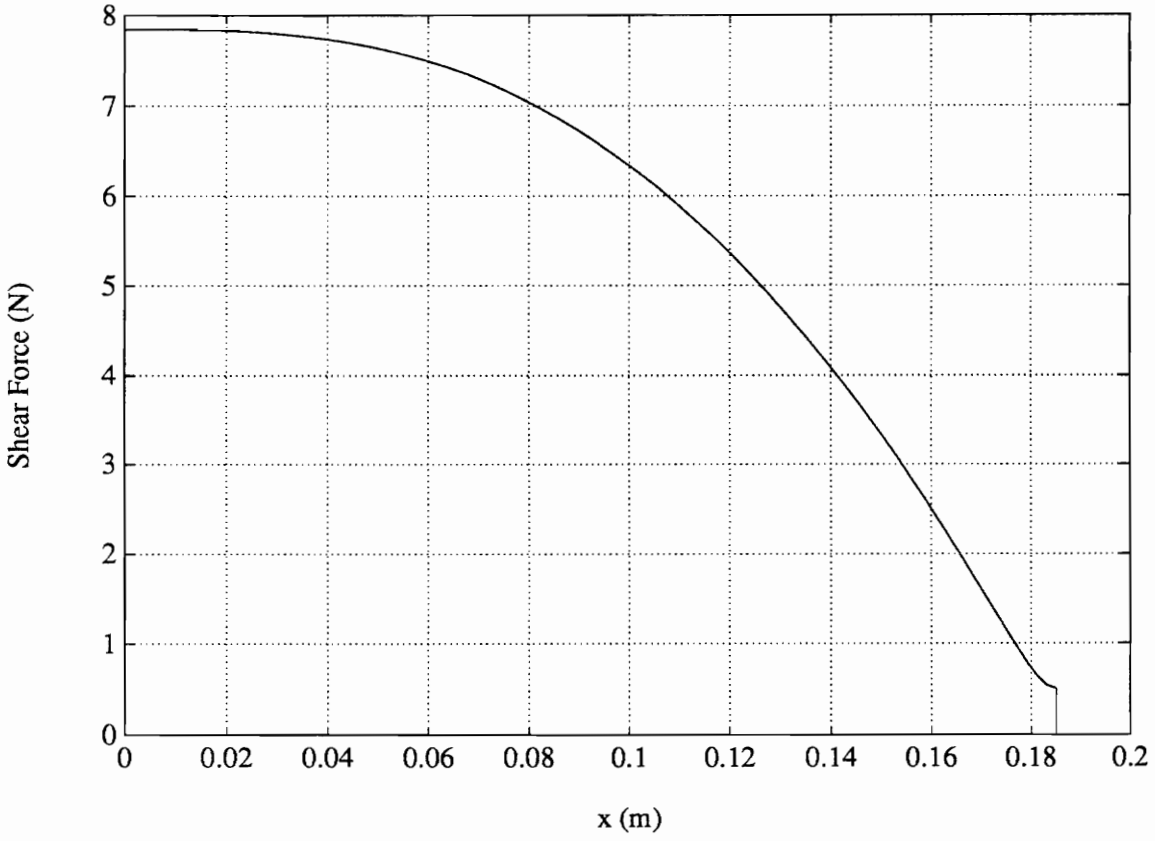

Figure 3.20: Shear force distribution along the beam due to constant force excitation.

experimental results introduced in Section 3.1. A magnifying parameter of 0.5 is needed to calculate the actual moment and shear force.

The dynamic moment and the shear force vs. frequencies at the clamped end of the beam have also been calculated, and the results are shown in Fig. 3.21 and Fig. 3.22, respectively. The moment and the shear force reach extreme values at the resonance frequencies, and the maximum value occurs at the first resonance frequency. The peak values for the second and the third modes become smaller because of the following reasons. One is that the amplitude of the beam displacement decreases as frequency increases, if the excitation source has a constant force input. The other is that the beam vibrating in the second mode, for example, has two sections vibrating out-of-phase so that the dynamic moments from the two sections cancel with each other. However, if the excitation is a pre-described motion. The results of the dynamic moment can be completely different. The maximum of the dynamic moment may occur at higher vibration modes. Since the actual excitation of a mechanical system is between a constant force excitation and pre-described motion excitation, the reduction of vibration amplitude does not necessarily provides a lower dynamic moment.

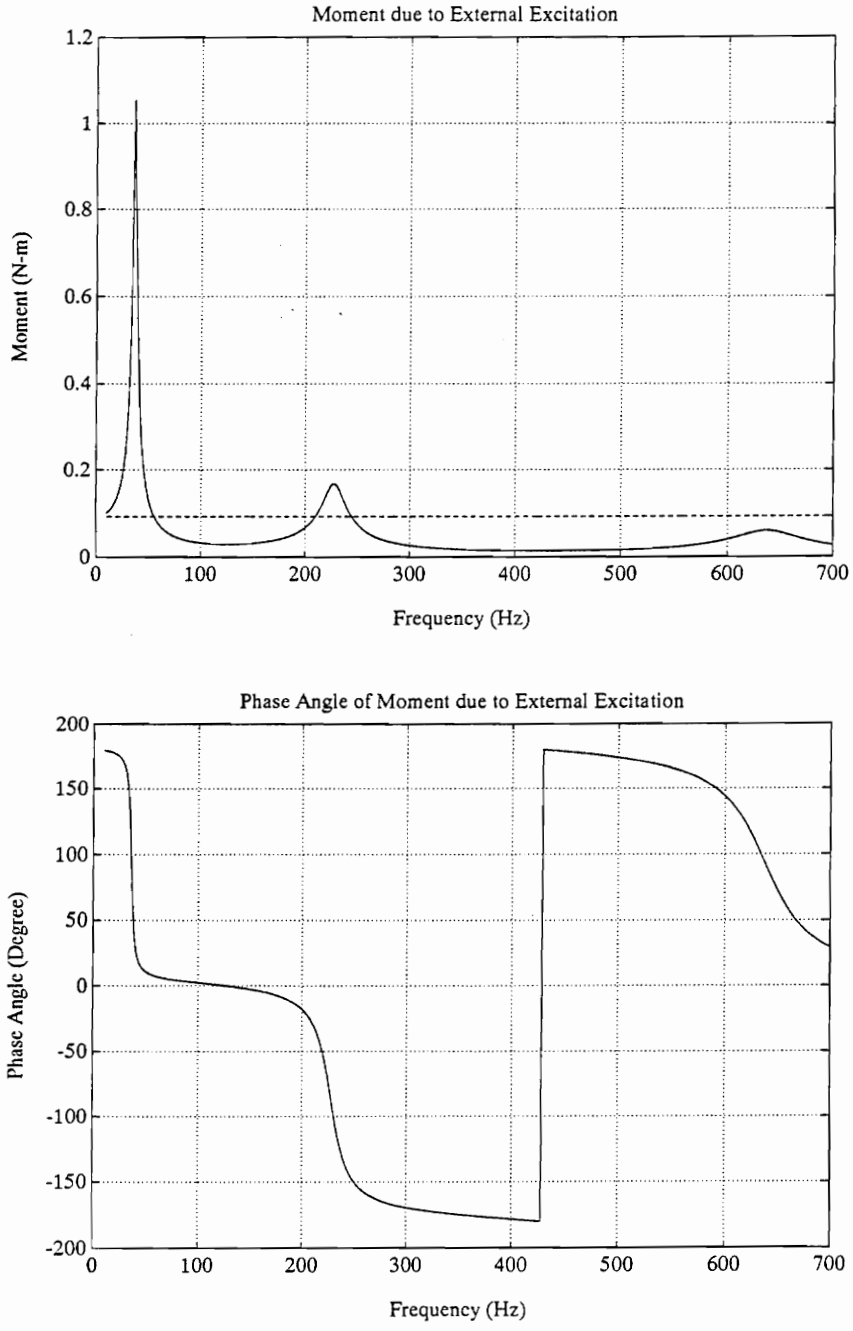

Figure 3.21: Dynamic moment at the end of the beam due to external excitation.

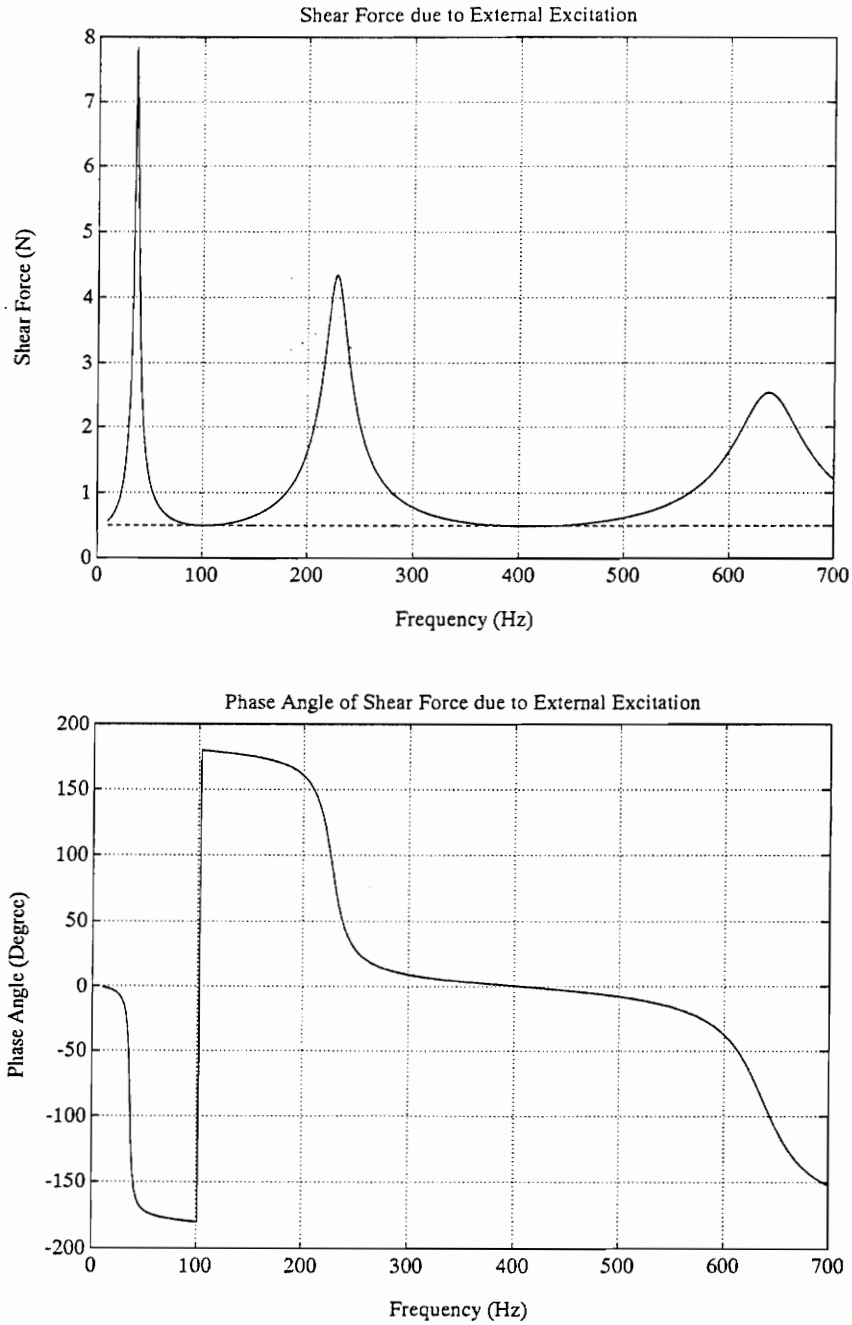

Figure 3.22: Dynamic shear force at the end of the beam due to external excitation.

3.4.2 Result of Actuator Excitation

For a pure bending beam with two piezoelectric actuators mounted on the top and bottom surfaces, the Bernoulli-Euler model gives a good prediction of activation moment (Crawley and Anderson, 1990). The moment-curvature equation is given by:

$$M = [2(EI)_a + (EI)_b]\kappa \ , \tag{3.9}$$

where the curvature, κ is expressed by:

$$\kappa = \frac{6(1+\frac{1}{T})(\frac{2}{t_b})\Lambda}{(6+\psi)+\frac{12}{T}+\frac{8}{T^2}} \ , \tag{3.10}$$

where

$$\psi = \frac{t_b E_b}{t_a E_a} \ , \tag{3.11}$$

and

$$T = \frac{t_b}{t_a} \ . \tag{3.12}$$

The induced strain, Λ, is assumed to be 300 $\mu\epsilon$ in Eq. (3.10), yielding an activation moment of about 0.1 N-m from Eq. (3.9). The displacement distribution of the beam resulting from the activation of PZT actuators at the first resonance (36.3 Hz) is shown

in Fig. 3.23. Fig. 3.24 shows the moment distribution along the beam. The shear force distribution is plotted in Fig. 3.25. The PZT activating excitation system is also a linear system, and the above results also can be considered as reference values. From Fig. 3.23, the maximum displacement at the free end is about 13 mm, which is two times the value of the experiment results presented in Section 3.1. Therefore, a magnifying parameter of 0.5 is needed in the calculation of the actual dynamic response due to the actuator excitation. This also implies that the actual induced strain from the PZT actuators in the experiment was only a half of what is assumed here.

The dynamic moment with respect to activation frequencies is shown in Fig. 3.26. Figure 3.27 shows the curve of the shear force vs. input frequencies. The dynamic moment shown in Fig. 3.26 has a similar characteristic to that excited by a constant forcing function. However, in Fig. 3.27, the maximum shear force appears at the second resonance frequency instead of at the first resonance frequency.

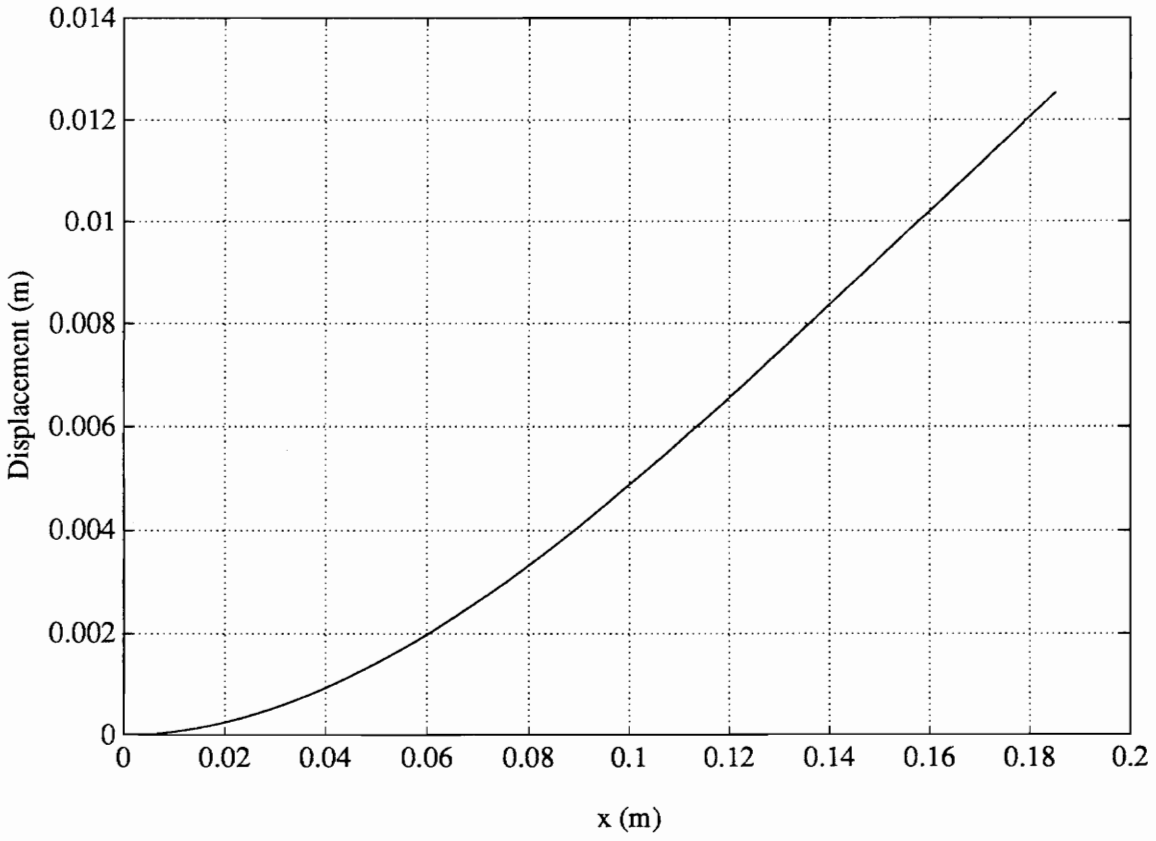

Figure 3.23: Displacement distribution along the beam due to the excitation of PZT actuators.

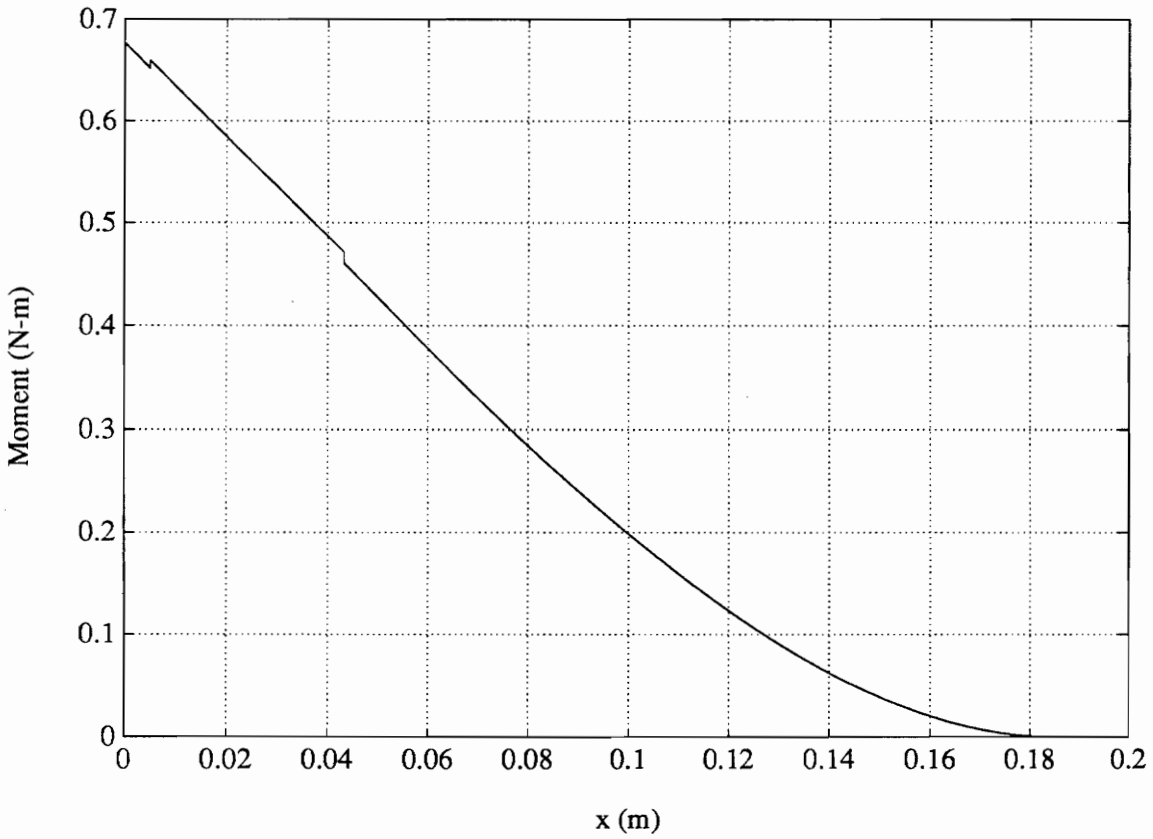

Figure 3.24: Moment distribution along the beam due to the excitation of PZT actuators.

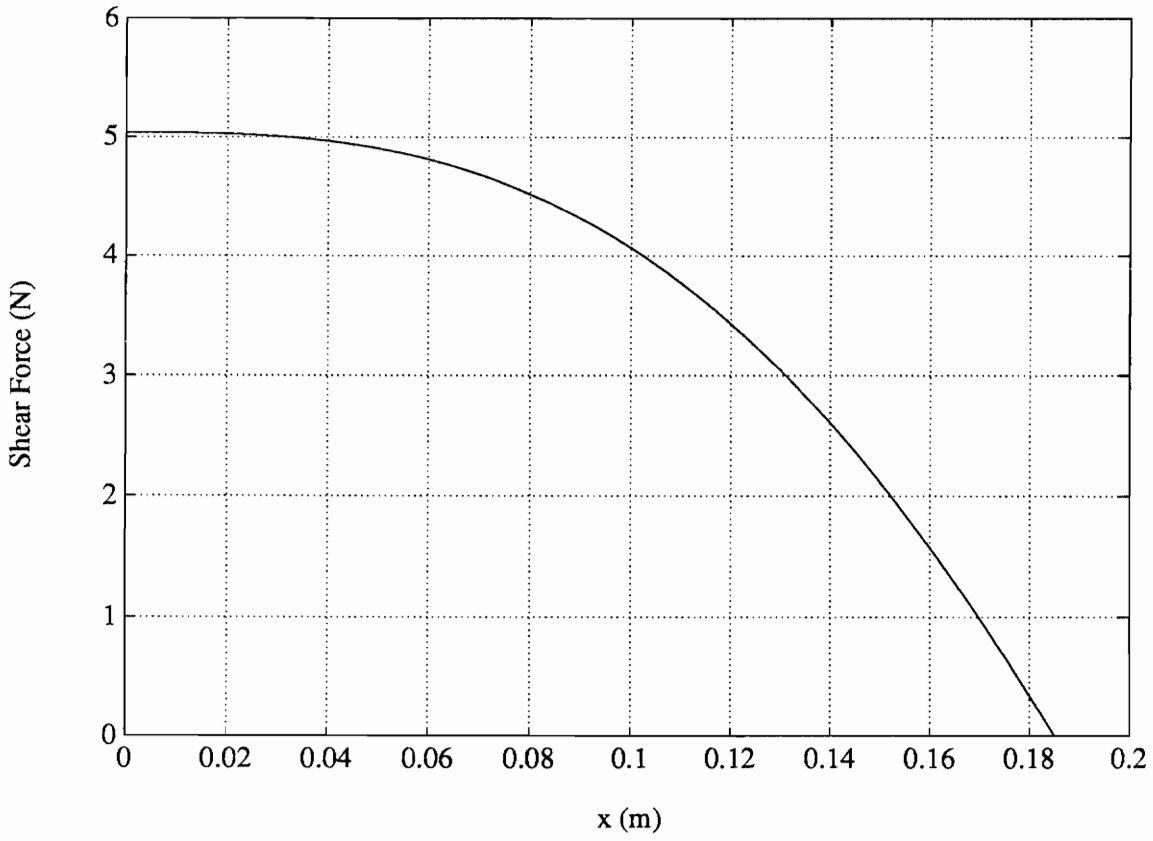

Figure 3.25: Shear force distribution along the beam due to the excitation of PZT actuators.

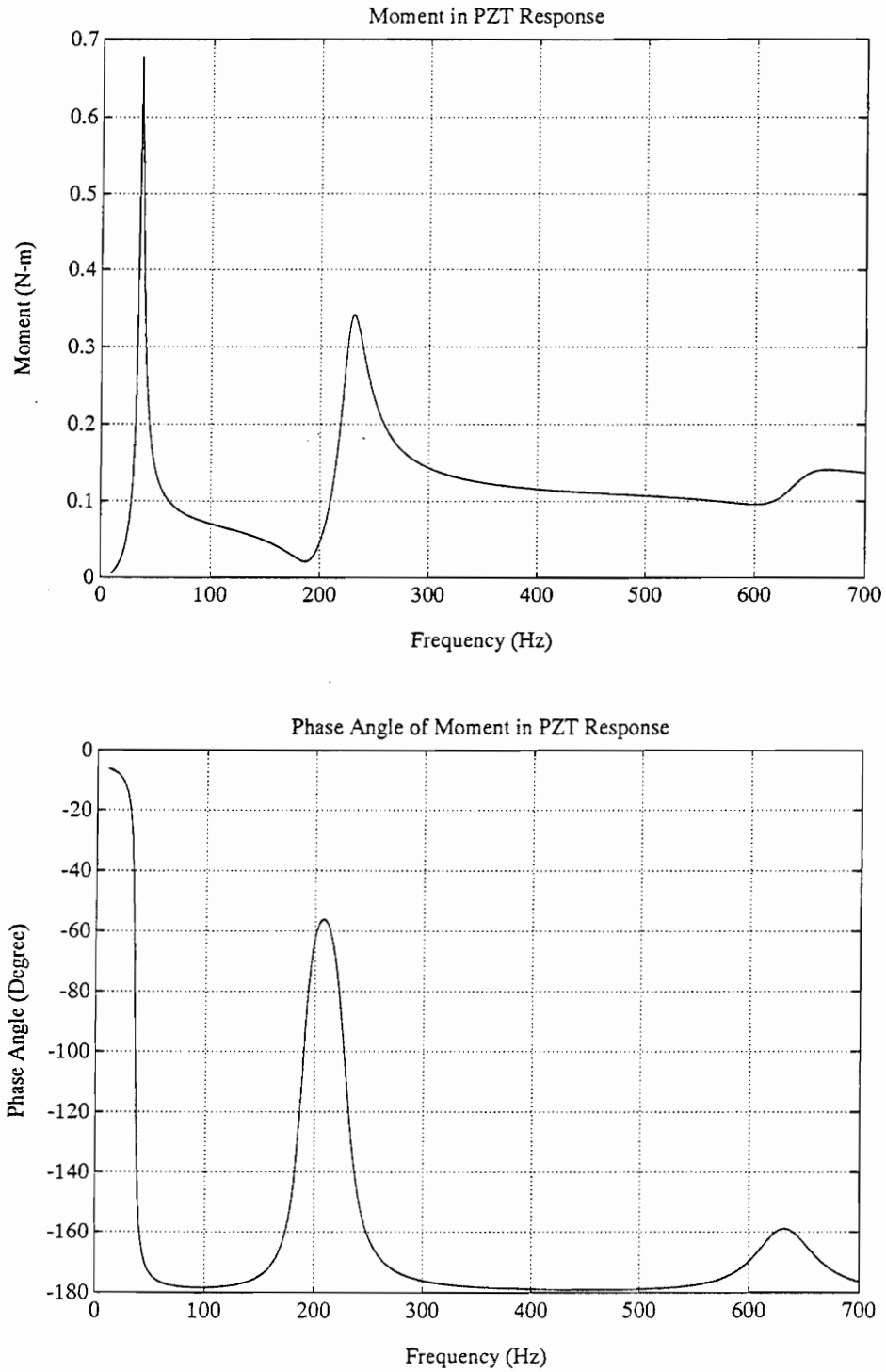

Figure 3.26: Dynamic moment at the end of the beam as a function of the frequencies of PZT excitation.

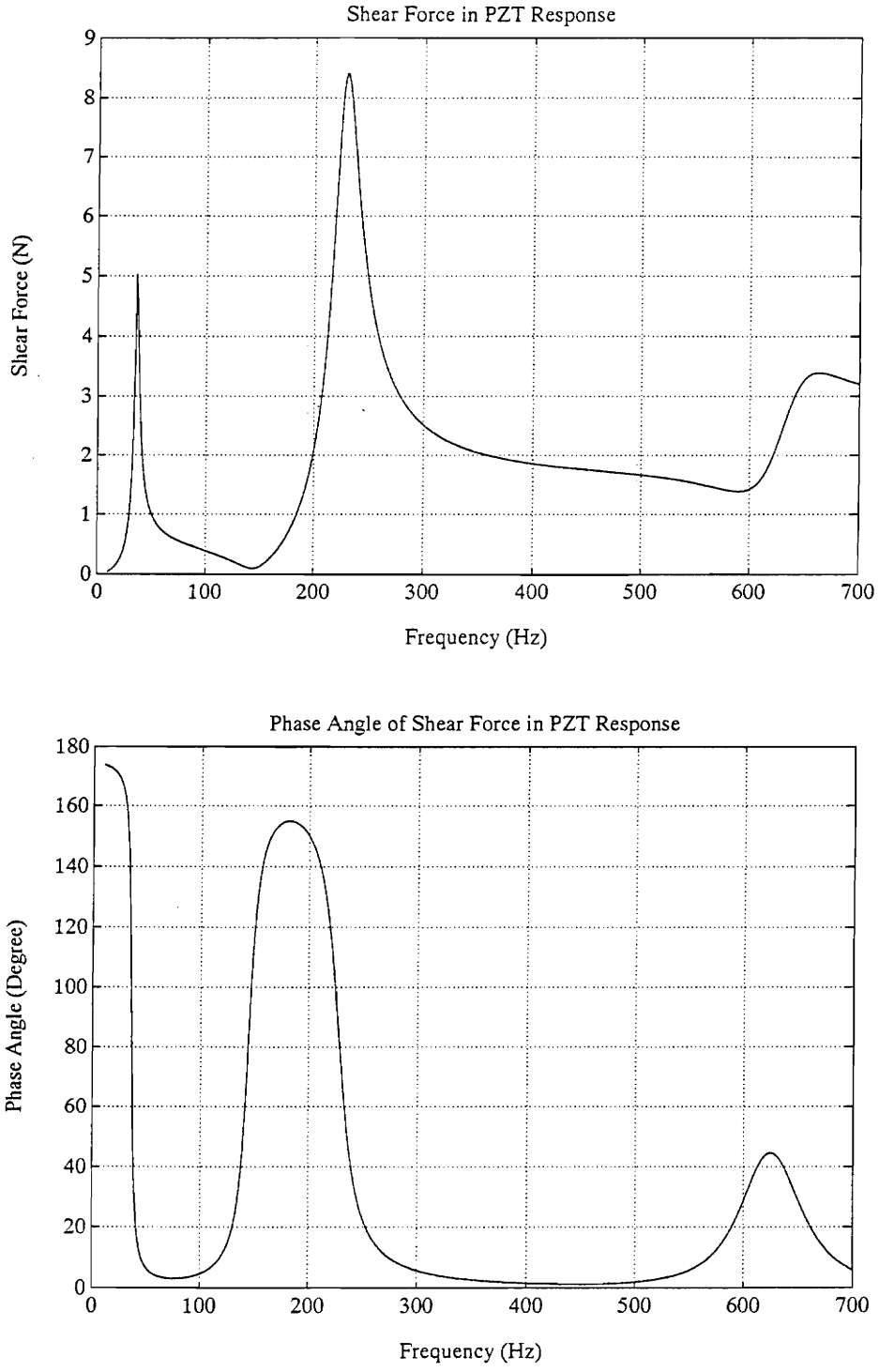

Figure 3.27: Dynamic shear force at the end of the beam as a function of the frequencies of PZT excitation.

3.5 Analysis of Active Fatigue Damage Control (A.F.D.C.) Experiments

In the A.F.D.C. experiments discussed in Section 3.1, the activation of PZT actuators reduced the maximum displacement at the free end of the beam from 10 mm to 3 mm. The displacement, dynamic moment and shear force along the beam can be calculated by superposition of the response of external excitation and the response of PZT actuators. A scale-down factor of 0.5 needs to be used according to the discussions in Sections 3.4.1 and 3.4.2. The superimposed displacement, dynamic moment and shear force distribution at the first mode are illustrated in Fig. 3.28, 3.29, and 3.30, respectively. In the figures, the dashed lines are the responses of the external excitation, the dash-doted lines are the results due to PZT excitation, and the solid lines are the superimposed results. The superimposed results are the differences between the external excitation and the PZT excitation.

The dynamic moment and its phase at the fixed end with respect to the frequency are shown in Fig. 3.31. Figure 3.32 shows the dynamic shear force and its phase vs. frequency. The dashed and dash-dotted lines represent the responses of external and PZT excitation. In Figs. 3.31 and 3.32, PZT excitation signal is out-of-phase with the external excitation signal, i.e., if the phase angle for the external excitation is zero, the phase angle for the activation voltage of PZT then is 180°. At the first resonant frequency, the dynamic moment due to PZT excitation has a -90° phase angle, while the

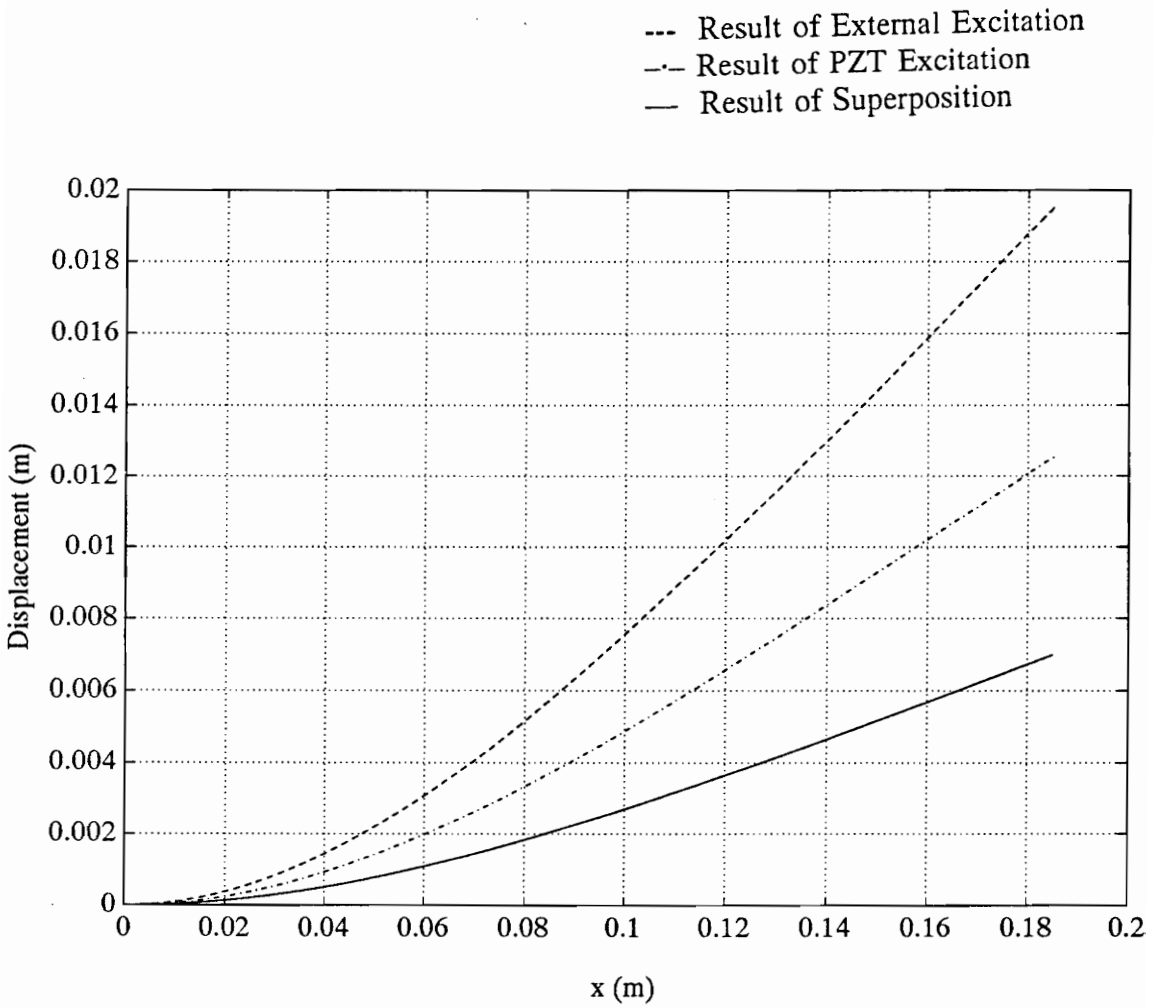

Figure 3.28: Displacement distribution along the beam.

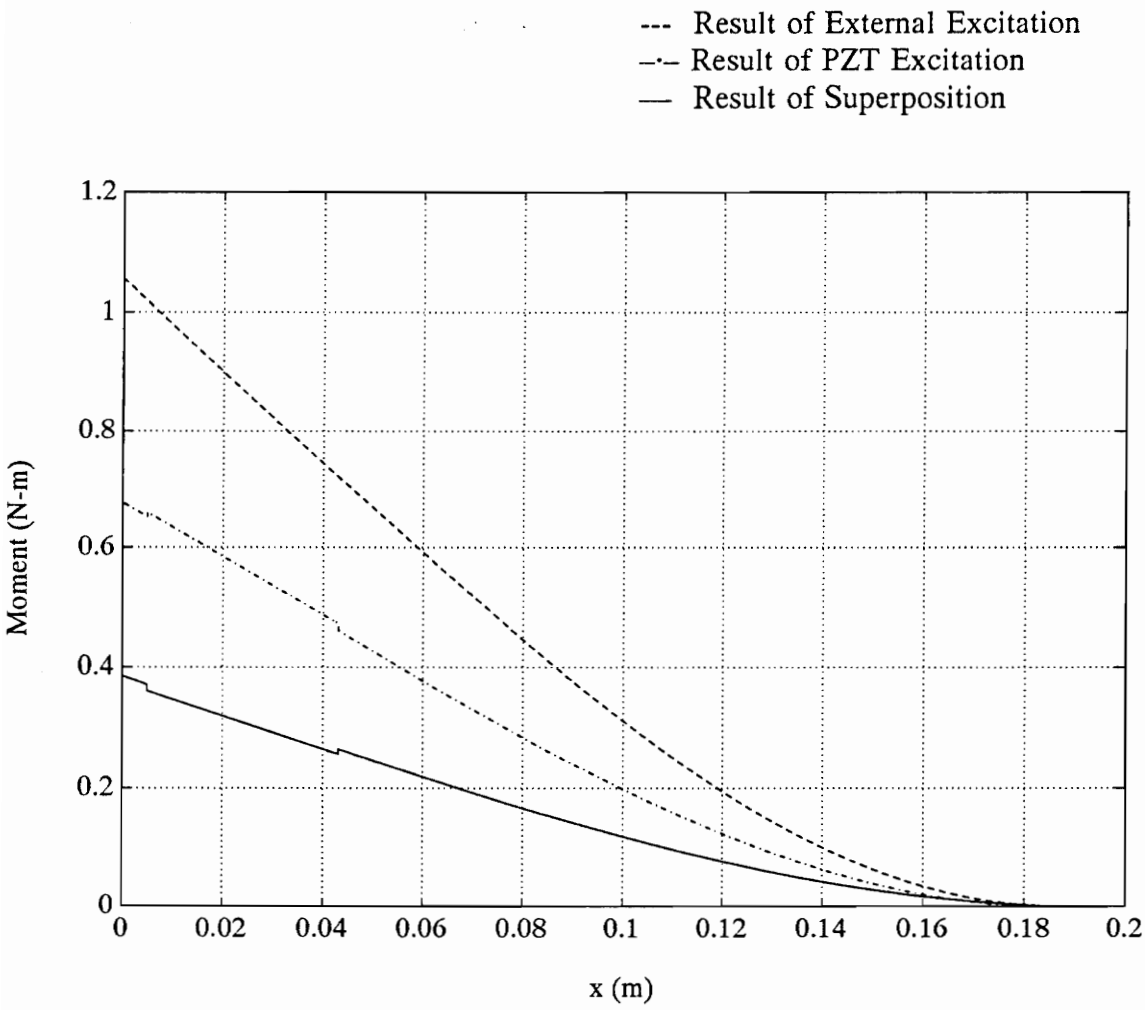

Figure 3.29: Moment distribution along the beam.

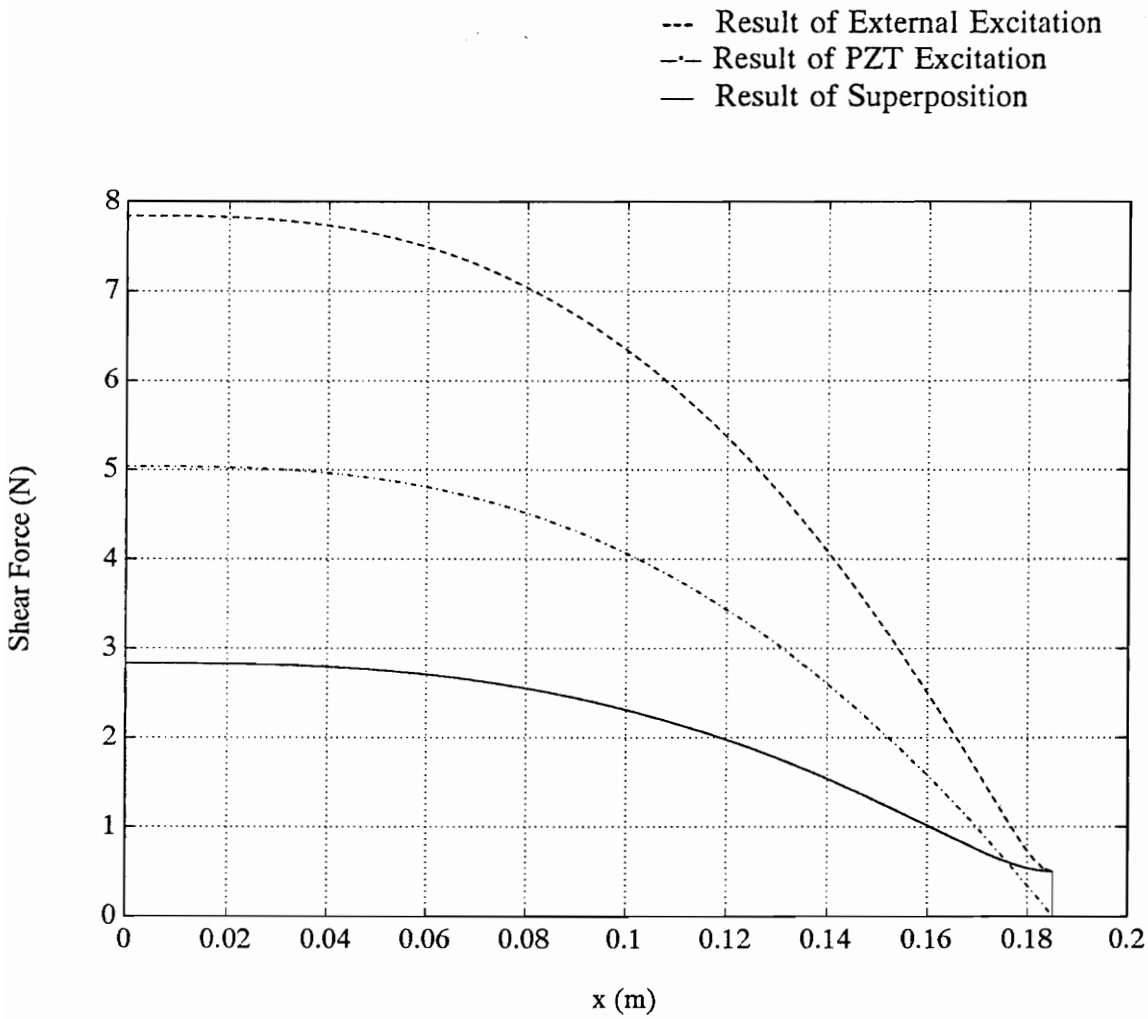

Figure 3.30: Shear force distribution along the beam.

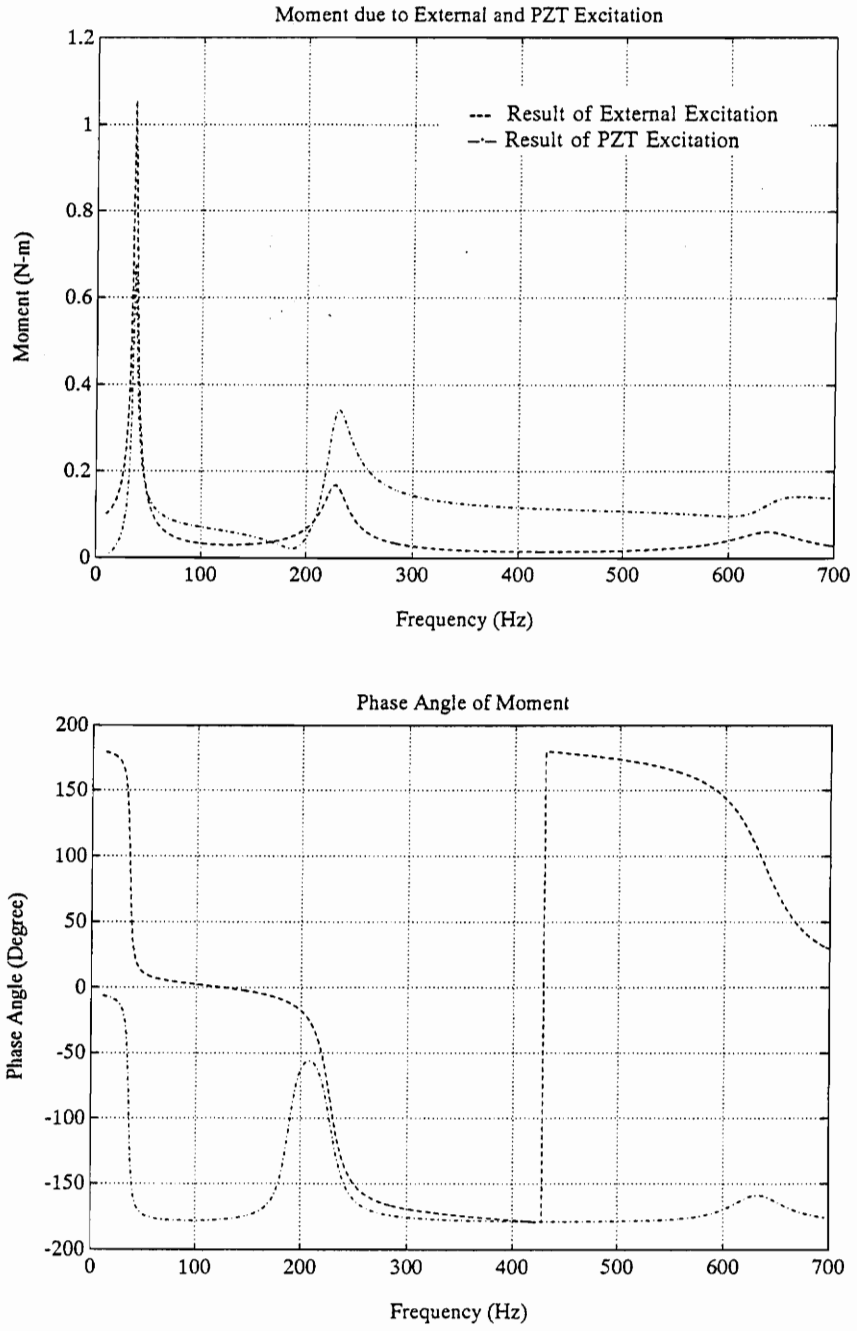

Figure 3.31: Dynamic moment and its phase at the end of the beam as a function of frequency.

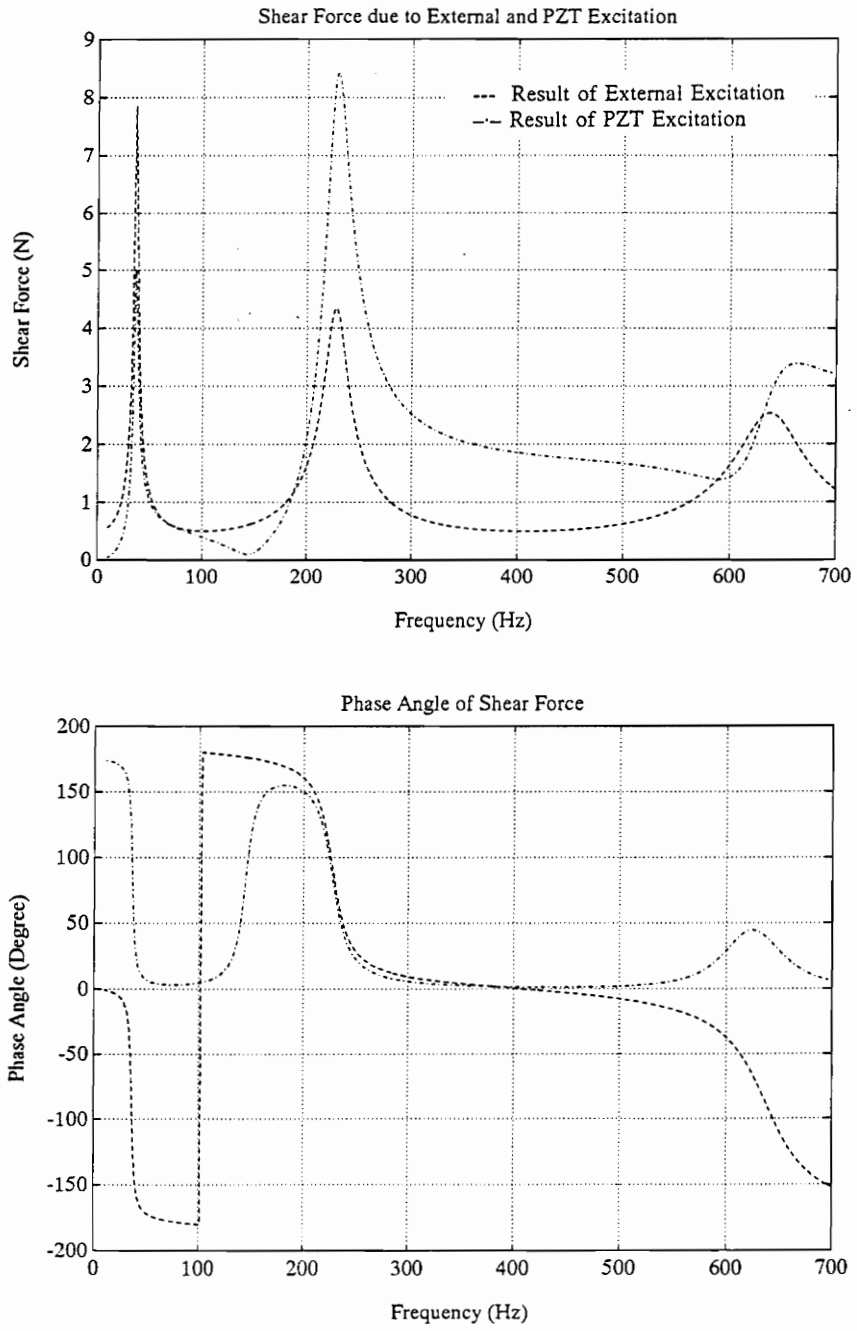

Figure 3.32: Dynamic shear force and its phase at the end of the beam as a function of frequency.

dynamic moment due to external excitation has a +90° phase angle. The two dynamic moments can be used to directly cancel each other. At the second resonant frequency, the dynamic moment due to PZT excitation has a -90° phase angle, while the dynamic moment due to external excitation also has a -90° phase angle. This indicates that in order to use the PZT actuator to reduce the damage at the second resonance, the voltage applied to the actuator must have a phase angle of +90°. The same principal can also be applied to the analysis of dynamic shear force.

The stress level in the adhesive layer before and after the PZT activation can be determined based on the finite element analysis (Section 3.2) and the dynamic moment and shear force. Before the activation of PZT, the moment applied to the adhesive joint by the dynamic response is 0.52 N-m, or 520 N-mm. The dynamic shear force applied to the adhesive joint is about 4 N. Considering the results of the finite element analysis conducted in Section 3.2, 1 N-mm of moment can generate 0.88 MPa of normal stress at the front edge (B) and 0.35 MPa of normal stress at the back edge (A) (shown in Fig. 3.6), the 520 N-mm of moment will generate 475.6 MPa of normal stress at the front edge and 182 MPa of normal stress at the back edge. Since 1 N shear force can generate 3 MPa of normal stress at the front edge (B) and 12 MPa of normal stress at the back edge (A) (shown in Fig. 3.10), 4 N of shear force will generate 12 MPa of normal stress at the front edge and 48 MPa of normal stress at the back edge. The total normal stress at the front edge is 469.6 MPa, in which 97.4% is generated by the dynamic moment.

The total normal stress at the back edge is 230 MPa, in which 79.1% is resulting from the dynamic moment. For the shear stress, since 1 N-mm of moment can generate 0.45 MPa of shear stress at the front edge and 0.25 MPa of shear stress at the back edge (shown in Fig. 3.7), 520 N-mm of moment will generate 234 MPa of shear stress at the front edge and 130 MPa of shear stress at the back edge. On the other hand, since 1 N of shear force can generate 1.9 MPa of shear stress at the front edge and 12 MPa of shear stress at the back edge (shown in Fig. 3.11), the 4 N of shear force will generate 7.6 MPa of shear stress and front edge and 48 MPa of shear stress at the back edge. The total shear stress at the front edge is 241.6 MPa, in which 97% is resulting from the dynamic moment. The total shear stress at the back edge is 178 MPa, in which 73% is due to the dynamic moment. The results clearly exhibit that the moment dominates the fatigue loading. The adhesive layer at the front edge subjects to the highest fatigue loading. For this reason, the following discussion will focus on the front edge of the adhesive joint.

After the activation of PZT actuators, from Fig. 3.29, the moment drops to 185 N-mm, and the shear force reduces to 1.5 N. Similar to the above analysis, 185 N-mm of moment will generate 162.8 MPa of normal stress and 83.25 MPa of shear stress at the front edge; 1.5 N of shear force will generate 4.5 MPa of normal stress and 2.85 MPa of shear stress at the front edge of the adhesive joint. The total stress state consists of 167.3 MPa of normal stress, and 86.1 MPa of shear stress.

After the stress level in the adhesive joint is obtained, the fatigue cycles for crack initiation and propagation can be determined according to the S-N (stress-fatigue cycle) and da/dN (crack propagation per cycle) curves of the adhesive layer. The increase of the fatigue life resulting from the activation of PZT actuators can also be determined. Because the S-N and da/dN curves for the adhesive material are not available, it is difficult to accurately calculate the original fatigue life and the increase of the fatigue cycles after the PZT activation. However, according to a typical S-N curve for epoxy (Adams and Wake, 1984), the fatigue cycles of crack initiation will generally increase more than 10 times if the load level decreases by 50%, which agrees with the experimental results.

Finally, the mechanism of indirect stress cancellation is illustrated in Fig. 3.33. The external excitation generates both static and dynamic moment and shear force. The dynamic moment and shear force at the first resonant frequency are much higher than the static moment and shear force. The PZT excitation can only generate dynamic moment and shear force at the fixed end. The magnitude of the response due to PZT excitation can be of the same order of magnitude as that resulting from external excitation. If the response of PZT excitation is out-of-phase with respect to the response of external excitation, the superposition of two dynamic responses will result in a great decrease in the dynamic moment and shear force at the fixed end of the beam.

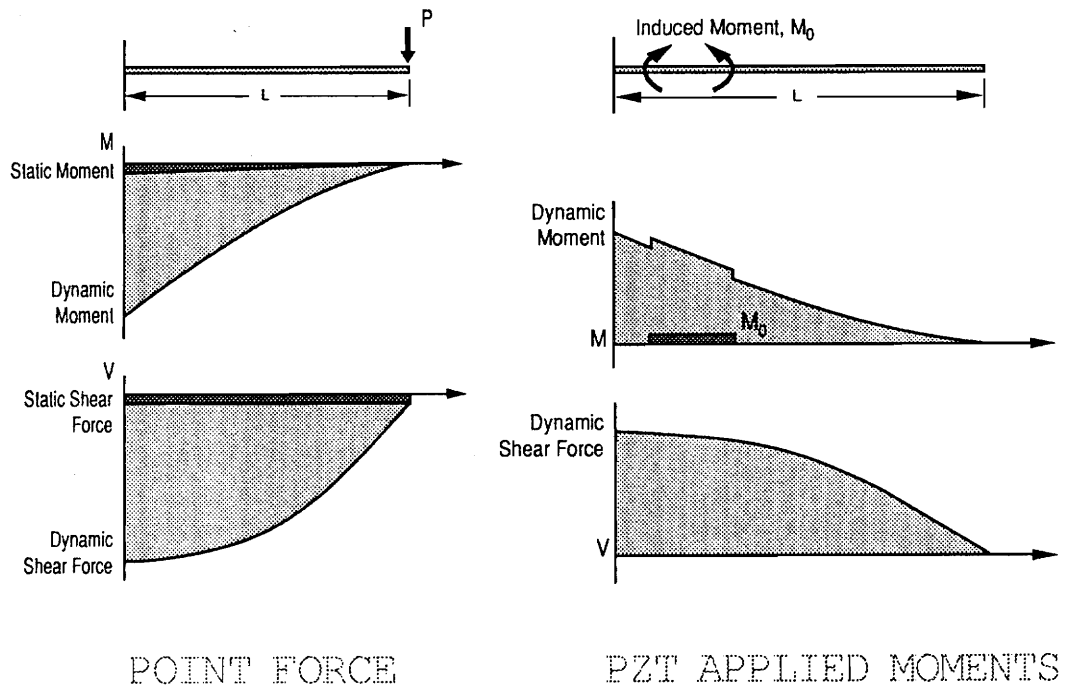

Figure 3.33: Schematic illustration for indirect stress cancellation.

3.6 Summary

The numerical analysis of fatigue damage control experiment shows the mechanism of fatigue damage control with indirect stress cancellation techniques. It also results that the dynamic moment due to the inertia force is the primary cause of fatigue damage. The PZT actuators cannot change the stress distribution in the adhesive joint directly. However, by controlling the dynamic response of structure, PZT actuators may significantly reduce the dynamic moment and shear force.

Generally, active fatigue damage control and active vibration control have different control objective functions which may have different placement of induced strain actuators. The objective function of active vibration control is the displacements or velocity, while the objective function of active fatigue damage control is the dynamic stress level at a specific area. A decrease in the stress level at the specific area does not require the decrease in displacements, while a decrease in the displacements of the whole system will result in a decrease in the inertial force, and hence a decrease in the dynamic stress level in the structure. However, since active vibration control is to control the displacements at some specific areas, it does not necessarily provide lower dynamic stresses. Therefore, the two control schemes can be very different, which depend on the structures, actuator configurations and locations, etc.

In summary, the following items have been discussed in this chapter:

1. Active fatigue damage control experiments have showed that the fatigue life of an adhesive joint can be increased by almost ten times by reducing the vibration amplitude by 70%. The reduction has been realized by the superposition of two out-of-phase dynamic responses.

2. Finite element analysis has been performed to calculate the stress distribution in the adhesive joint. Because of the discontinuity of the single-lap connection, stress concentrations occur at the front edge and the back edge of the adhesive joint for the moment loading and shear force loading. The normal stress and shear stress distributions in the adhesive joint for unit moment and unit shear load have been calculated. The high stress level at the front edge caused by stress concentration is the reason of crack initiation and propagation. Finite element analysis has also showed that the activation of PZT actuators has no direct contribution to the stress distribution in the adhesive joint.

3. Two techniques, i.e., direct stress cancellation and indirect stress cancellation, for active fatigue damage control have be discussed. The direct stress cancellation uses the induced stress to directly cancel the original structural stresses, while the indirect stress cancellation uses the dynamic moment and shear force excited by the induced stress and strain to cancel the original dynamic structural loading.

4. The expressions for the dynamic moment and shear force have been given. The displacement, moment and shear force distributions have been calculated for the external excitation and PZT activation. The dynamic moment and shear force with respect to frequencies have also been calculated. The results show that the dynamic moment and shear force, which depend on both frequencies and mode shape, reach their extremes at the resonant frequencies.

5. Numerical analysis has proved that the dynamic loading is the dominant source for fatigue damage of the adhesive joint. In the dynamic loading, the dynamic moment plays a much more important role than dynamic shear force.

Chapter 4 Conclusions and Recommendations

This thesis deals with the theoretical modeling and, experimental investigation of active crack damage control (Chapter 2), and active fatigue damage control (Chapter 3). A summary of the research along with the major conclusions relating to active crack damage control is as follows:

(1) Two scenarios have been analyzed for active crack damage control. In the first scenario, inelastically elongated SMA fibers are embedded into composites. Because of the free edge effect, the activation is not effective on the center part of the composites. For the SMA fibers with short inelastically deformed sections, the activation is effective, but in reality, the position of the section of the SMA fiber which is to be elongated is difficult to determine. In the second scenario, virgin SMA fibers are embedded into composites. When the crack propagates and touches the fibers, the crack will pass through the fibers leaving the fibers intact, and the crack opening will transform the bridging parts of the fibers into the martensite phase. The activation of the bridging section by heating will cause a recovery stress to be applied to the crack surfaces, resulting in a decrease of the stress intensity at the crack tip.

(2) Photoelactic experiments have been used to study the activation effects of SMA actuators on the crack tip. By using a partly prestrained SMA fiber, and activating it in front of the crack tip, the stress intensity at the crack can be decreased by as much as 24%. The results experimentally demonstrate the activation effects of SMA fibers on active crack damage control.

(3) Finite element analysis has been carried for comparison with the experimental photoelastic results. Good agreement is obtained. In addition, the finite element analysis also shows that the stress level at the crack tip is decreased by 36% after the activation. The results numerically show that the activation of a short martensite phase section can greatly change the stress distribution in the surrounding area.

(4) A new theoretical model for the debonding length of SMA fibers has been developed, and the SMA pull-out tests are conducted to verify the theoretical model. Good agreement with the experiment results are obtained.

(5) A new theoretical model for SMA fibers bridging a crack has been developed. The expressions for crack opening displacement, martensite phase fraction, fiber strain, fiber stress and stress intensity factor are obtained for pull-out tension and activation tension. For a given case, the numerical calculations show that after

the activation of the bridging fibers, the stress intensity can be decreased by as much as 50%.

The summary of research and major conclusions relating to active fatigue damage control is as follows:

(1) Experiments have been performed to investigate the effect of damage and the effect of activation. A shaker is used to input damage signal where the frequency is close to the first resonance frequency. The displacement at the free end was observed to be about 10 mm. After 52,000 cycles of loading, the adhesive joint failed. In contrast, in another experiment PZT actuators activate out-of-phase with the shaker, and the displacement at the free end was reduced to 3 mm, and the adhesive joint failed after 500,000 cycles of loading.

(2) Finite element analysis has been conducted to calculate the stress distribution in the adhesive joint. Because of the discontinuity of the single-lap connection, high stress peaks are generated at the front and rear edge of the adhesive joint for the moment loading and shear force loading. The normal stress and shear stress distributions in the adhesive joint for unit moment and unit shear load are calculated. In addition, finite element analysis confirms that even when the actuators locate in the vicinity of the adhesive joint, the stress distribution in the

adhesive joint is not affected by the activation of PZT actuators.

(3) Active fatigue damage control can be realized through two techniques - direct stress cancellation and indirect stress cancellation. The direct stress cancellation uses the induced stress to directly cancel the original structural stresses, while the indirect stress cancellation uses the dynamic moment and shear force excited by the induced strain and stress to cancel the original dynamic structural loading.

(4) The expression for the dynamic moment and shear force has been derived. The displacement, moment and shear force distributions were calculated for the external excitation force and the PZT activation moments. The variation in the moment and shear force with frequency was also calculated. The results showed that the resonance frequencies are the primary band of high dynamic loading level.

(5) Numerical analysis proves that the dynamic loading is the dominant source for the damage of the adhesive joint. The active load canceling is also realized by using dynamic response. For active vibration control, the displacement is chosen as objective control function, and the canceling effect can be estimated by a static analysis method. However, for active fatigue damage control, the moment and shear force are chosen as objective control functions, and the canceling effect

cannot be estimated by a static analysis method.

Recommendations

Active damage control is a new emerging technique, and this thesis presents only the beginning of this important research area. More in-depth theoretical and experimental investigations are needed. Some recommendations for future work are as follows:

(1) The theoretical model is only a preliminary model or simplified model for the active crack damage control in SMA hybrid composite system. For this model, further experimental measurements are needed to verify the accuracy of this prediction.

(2) In the configuration of active fatigue damage control, the external excitation and activation are assumed to be harmonic signals with single frequency. However, in practice, the disturbance can be random or broadband, and the activation signal may also be broadband, and may not necessarily have the same frequency as the disturbance signal. It would be of a great interest to extend the current analysis to modeling of active CONTROL of the fatigue damage of the adhesive bonding joint in a broad frequency range to determine the applied field and phase angle, the optimal actuator placement, and actuator configurations, etc.

References

Adams, R. D. and W. C. Wake, 1984, Structural Adhesive Joints in Engineering, Elsevier Applied Science Publishers, London.

Anderson, E. H. and E. F. Crawley, 1989, "Piezoceramic Actuation of One and Two Dimensional Structures," Paper No. 5-89, Space Systems Laboratory, Dept. of Aero./Astro., MIT.

Barker, D., 1989, Active Dynamic Response Tuning of Adaptive Composites Utilizing Embedded Nitinol Actuators, Master Thesis, Department of Mechanical Engineering, Virginia Polytechnic Institute and State University, Blacksburg, Virginia.

Buehler, W. J., and R. C. Wiley, 1965, "Nickel-Base Alloys," U.S. Pat. 3,174,851, 23 March, 1965.

Chaudhry, Z. and C. A. Rogers, 1991, "Bending and Shape Control of Beams Using SMA Actuators," Journal of Intelligent Material Systems and Structures, Vol. 2, No. 4, pp. 581-602.

Clark, A. E., 1980, "Magnetostrictive Rare Earth -Fe2 Compounds," Chapter 7 in Ferromagnetic Materials, Vol., 1, North Holland Publishing Company.

Crawley, E. F. and Anderson, E. H., 1990, "Detailed Models of Piezoceramic Actuation of Beams," J. of Intelligent Material Systems and Structures, Vol. 1, pp. 4-25.

Cross, W. B., A. H. Kariotis and F. J. Stimler, 1969, "Nitinol Characterization Study," Goodyear Aerospace Corporation Report No. Ger 14188, (NASA CR-1433), Akron, Ohio.

Cross, L. E. et al., 1987, "Piezoelectric and Electrostrictive Materials for Transducer Applications," Pennsylvania State University, University Park, Materials Laboratory, 1985-1987.

Dally, J. W. and W. F. Riley, 1985, Experimental Stress Analysis, McGraw-Hill Book Company, New York.

DATA, Inc., 1987, Composites and Laminates, Desk-Top Data Bank.

Dimitriadis, E. K., C. R. Fuller and C. A. Rogers, 1989, "Piezoelectric Actuators for Distributed Noise and Vibration Excitation of Thin Plates," Failure Prevention and

Reliability - 1989, DE-Vol. 16 (Proceedings of the 8th Biennial Conference on Failure Prevention and Reliability, Montreal, Canada, 18-20 September, 1989), pp. 223-234.

Dye, T., 1990, "An Experimental Verification of a One-dimensional Constitutive Model of Shape Memory Alloys," Master Thesis, Department of Mechanical Engineering, Virginia Polytechnic Institute and State University, Blacksburg, Virginia.

Evans, A.G. and A. H. Heuer, 1980, "Review - Transformation Toughening in Ceramics: Martensitic Transformations in Crack-Tip Stress Fields," Journal of the American Ceramic Society, Vol. 63, No. 5-6, pp. 241-248.

Hanagud, S., G. L. NageshBabu, R. L. Roglin and S. G. Savanur, 1992, AIAA/ASME/ASCE/AHS/ASC 33rd Structures, Structural Dynamics and Materials Conf., Dallas, Texas.

Hertzberg, R. W., 1989, Deformation and Fracture Mechanics of Engineering Materials, Wiley, New York.

Jackson, C. M., H. J. Wagner and R. J. Wasilewski, 1972, "55-Nitinol---The Alloy with a Memory: Its Physical Metallurgy, Properties and Applications," NASA-SP-5110, pp. 91.

Kanninen, M. F. and C. H. Popelar, 1985, Advanced Fracture Mechanics, Oxford University Press, New York.

Lawn, B. R. and T. R. Wilshaw, 1975, "Fracture of Brittle Solids," Cambridge Univ. Press.

Lazarus, K. B. and E. F. Crawley, 1989, "Induced Strain Actuation of Composite Plates," GLT Report #197, March, MIT.

Liang, C. and C. A. Rogers, 1989, "Behavior of Shape Memory Actuators Embedded in Composites," Proceedings of the 1989 International Composite Conference, Beijing, PRC.

Lin, M. W. and C. A. Rogers, 1989, "Investigation of Fundamental Design Issues Related to SMA Reinforced Composites," VPI-E-89-3, SMSL-FR-89-1, Dept. of Mechanical Engineering, Virginia Polytechnic Institute and State University, Blacksburg, Virginia.

Lin, M. W. and C. A. Rogers, 1991, "Analysis of Stress Distribution in a Shape Memory Alloy Composite Beam." AIAA 32nd SDM, Baltimore, Maryland.

Marshall, D. B. and B. N. Cox, 1985, "The Mechanics of Matrix Cracking in Brittle-Matrix Fiber Composites," Acta Metall., Vol. 33, No. 11, pp. 2013-2021.

Meguid, S. A., 1986, Impact Surface Treatment, Elsevier Applied Science Publishers, London.

Meguid, S. A., 1989, Engineering Fracture Mechanics, Elsevier Applied Science Publishers, London.

Mitchell, L. D., 1992, User's Guide -- BEAM VI, Mechanical Engineering Department, Virginia Polytechnic Institute and State University, Blacksburg, Virginia.

Nawy, E. G., 1989, Prestressed Concrete - A Fundamental Approach, Prentice-Hall.

Nemat-Nasser, S. and M. Hori, 1987, "toughening by Partial or full Bridging of Cracks in Ceramics and Fiber Reinforced Composites," Mech. Mat., Vol. 6.

Parker, A. P., 1981, The Mechanics of Fracture and Fatigues, E. & F. N. Spon, New York.

Piggott, M. R., 1991, "Failure Precesses in The Fiber-Polymer Interface," Comp. Sci.

Tech. 42 (1991) 57-76.

Pilkey, W. D., and P. Y. Chang, 1978, Modern Formulas for Statics and Dynamics, McGraw-Hill Book Company.

Rogers, C. A., 1989, "Dynamic and Structural Control Utilizing Smart Materials and Structures," Proceedings of the International Workshop on Intelligent Materials (The Society of Non-Traditional Technology, Tsukuba, Japan), pp. 109-121.

Rogers, C. A., C. Liang and J. Jia, 1989, "Behavior of SMA Reinforced Composite Plates - Part I: Theory," Proc. of the 30th Structure, Structural Dynamics and Materials Conf., Paper No. AIAA 89-1389, Mobile, AL,

Rogers, C.A., C. Liang and S. Li, 1991, AIAA/ASME/ASCE/AHS/ASC 32nd Structures, Structural Dynamics and Materials Conf., Baltimore, MD.

Rogers, C. A. et al., 1991, "Smart Materials, Structures and Mathematical Issues for Active Damage Control," Research Proposal, CIMSS, Virginia Polytechnic Institute and State University, Blacksburg, Virginia.

Rolfe, S. T., 1972, "Fracture Mechanics in Bridge Design," Civil Engineering, ASCE,

August.

Rolfe, S. T. and J. M. Barsom, 1977, Fracture and Fatigue Control in Structures, Prentice-Hall, Inc.

Schetky, L., 1979, "Shape Memory Alloys," Sci. Am. 241, 74.

Sewell, J. M., "Principles of Applicable to Terfenol Devices," Proceeding of the First International Terfenol Conference on Giant Magnetostrictive Alloys, Marbell, Spain.

Sih, G.C., 1973, Handbook of stress Intensity Factors, Lehigh University, Bethlehem.

Sneddon, I.N. and M. Lowengrub, 1969, Crack Problems in the Classical theory of Elasticity, Wiley, New York.

Sun, C. T. and T. L. Norman, 1990, "Design of a Laminated Composite with Controlled-Damage Concept," Composites Science and Technology, Vol. 39, pp 327-340.

Uchino, K., 1986, "Electrostrictive Actuators: Materials and Applications," Ceramic Bulletin, Vol. 65, No. 4.

Uchino, K. 1986, "Electrostrictive Actuators: Material and Applications," American Ceramic Society Bulletin, Vol. 65, pp 647-652.

Uchino, K. and L. E. Cross, 1980, "Electrostriction and Its Interrelation with Other Anharmonic Properties of Materials," Japanese Journal of Physics, Vol. 19, No. 4.

Wang, B. T., E. K. Dimitriadis and C. R. Fuller, 1990, "Active Control of Structurally Radiated Noise Using Multiple Piezoelectric Actuators," Proceedings of the AIAA/ASME/ASCE/AHS 31st Structures, Structural Dynamics and Materials Conference, Long Beach, CA, April 2-4, Paper No. AIAA-90-1172.

Wang, B. T. and C. A. Rogers, 1990, "Laminate Plate Theory for Spatially Distributed Induced Strain Actuators,'' Proceeding of the Fifth Japan-U.S. Conference on Composite Material, Tama City, Japan, June.

Wells, J. K. and W. R. Beaumont, 1985, "Debonding and Pull-out Processes in Fiber Composites," J. Mater. Sci. 20, 1275.

Young, D. and R. P. Felgar, Jr., 1949, Tables of Characteristics, Functions Representing Normal Modes of Vibration of a Beam, The University of Texas Publication 4913.

Vita

Shi Li was born in Shenyang, Liaoning Province, People's Republic of China (PRC) on December 5, 1955. He grew up in Beijing, PRC, and graduated from the High School attached to People's University of China in 1974. After high school, he worked in Computer Center of Science Academy of China for three years. Then, he attended Beijing University of Aeronautics and Astronautics (BUAA), majoring in applied mechanics. He received a bachelor's degree from Applied Mechanics Department in 1982, and a master's degree from Power Engineering Department in 1984. After working for five years at BUAA as a assistant professor, he came to Virginia Polytechnic Institute and State University to continue his graduate study in 1989. He worked in the area of intelligent material systems and structures, and graduated with his another M.S. degree in the Mechanical Engineering Department in September of 1992.

Shi Li